Development of Novel Materials for Solid-State Lithium-Sulfur Batteries

Lefevr, Jessica

Publication date:
2018

Document Version
Publisher's PDF, also known as Version of record

Development of Novel Materials for Solid-State Lithium-Sulfur Batteries

PhD THESIS

Submitted in candidacy for the degree Doctor of Philosophy

Jessica Lefevr

December 2018

Technical University of Denmark

Department of Energy Conversion and Storage

Preface

This thesis is submitted in candidacy for the PhD degree from the Technical University of Denmark (DTU) based on the work carried out at the Electrochemical Materials and Interfaces (EMI) section at the Department of Energy Conversion and Storage, during the period from December 2015 to December 2018. The project was supervised by Senior Scientist Didier Blanchard, co-supervised by Professor Poul Norby and Professor Harry Hoster from the department of chemistry, Lancaster University. The work has been funded by the Danish Council for Strategic Research and by a grant received from Otto Mønsteds Fond. The Synchrotron measurements performed during the project have been funded by DANSCATT, instrument supported by the Danish Agency for Science and Higher Education. A 4-month external stay was carried out at Lancaster University in the group of John Griffin and Nuria Tapia Ruiz, Department of Energy Lancaster.

Acknowlegement

First of all I would like to thank my supervisor, Didier Blanchard, and co-supervisor, Poul Norby, for guidance and discussions. Secondly, I would like to thank John Griffin who supervised my work at Lancaster University.

I would also like to thank researcher Søren Bredmose Simosen and senior development engineer Janet Jonna Bentzen for help with microscopic analysis of samples and fellow PhD-student Tiago Cunha Ramos and senior researcher Peter Stanley Jørgensen for help with analyzing tomography data. A big thank you goes to fellow PhD student Mathias Kjærgård Christensen for help along the way and good working environment.

Finally, I would like to thank beamline scientists: Chiara Cavallari (ESRF; ID 20), Fabian Wilde (DESY, P05 Petra) and Guiliana Aquilanti (Elettra Sincrotrone Trieste) for help with synchrotron measurements.

Abstract

To meet the growing energy demands of the future, safer batteries, with higher energy density are required. Li-ion batteries have been on the market for nearly 30 years and although there has been improvements of the original technology of the 90's, the theoretical capacities have been reached and little increment are expected, therefore new materials and chemistry are needed.

Among alternatives to Li-ion batteries are Li-S batteries with higher energy densities, demonstrated 500 $Whkg^{-1}$ vs 250 $Whkg^{-1}$for the best Li-ion batteries. Conventional Li-S batteries use salts dissolve in liquid solvents as electrolyte. However the solvents are flammable, which causes safety concerns and cause the shuttling of dissolve polysulfide resulting in rapid self-discharge of the batteries. Furthermore, lithium metal cannot be used as anode material and lithium dendrite formation shortens the lifetime of the batteries. A solution to these problems is to replace the liquid electrolyte by solid-state electrolytes based on ionic solids. In this work, two novel solid-state electrolytes, $LiBH_4$-SiO_2 and $LiBF_4$-$LiBH_4$, have been investigated as potential candidates for solid-state lithium sulfur batteries. These electrolytes have been synthesized and characterized using state of the art technics such as electrochemical impedance spectroscopy, Raman spectroscopy and nuclear magnetic resonance (NMR). High ionic conductivities were measured (0.1 mS/cm^{-1} at room temperature).

The electrolyte made from a composite of $LiBH_4$-SiO_2 has a higher Li^+ conductivity than that of pure $LiBH_4$ (1000 times higher at room temperature, 0.1 mS/cm^{-1} vs 0.1 10^{-3} mS/cm^{-1}). Our investigation showed no evidence for the formation of new bulk phases but the existence of a highly conductive interface between the insulating silica and the borohydride, most probably resulting from the reaction of $LiBH_4$ with the surface silica silanol groups. The Raman and NMR measurements clearly sow the different behavior of the composites compared to pure $LiBH_4$.

For $LiBH_4$-$LiBF_4$, with low content of $LiBF_4$ we found that the increased Li^+ conductivity is occurring in modified $LiBH_4$, possibly via a solid solution with $LiBF_4$, while for higher $LiBF_4$ contents decomposition of $LiBH_4$ occurs and result in lower conductivities.

Li-S batteries build around $LiBH_4$-SiO_2 solid electrolyte have been successfully assembled and tested. Capacityies of 794 $mAhg^{-1}$ sulfur have been obtained after 10 cycles at charge-discharge rate of 0.03 C and 50 ^{o} C. Because larger capacities than the theoretical one were observed during the first discharge – charge cycle, protection of the sulfur cathode has been investigated. We deposited LiPON thin films on the cathode surface to protect it from direct contact with the electrolyte. These batteries showed, smaller capacities, but better capacity retention over cycling than the batteries with non-coated cathodes. The first discharge overcapacities disappeared. This result underlines the importance of the interface treatment and engineering within Li-S solid state batteries.

Dansk Resumé

For at imødekomme det stigende energi behov for i fremtiden er der behov for sikre batterier med højt energi behov. Li-ion batterier har været på markedet i 30 år og selvom der har været forbedringer af den oprindelige teknologi er den teoretiske grænse ved at være nået og der kan derfor kun forventes små forbedringer fremadrettet, derfor er der behov for nye materialer og nye batteri teknologier.

Iblandt alternativerne til Li-ion batterierne har Li-S batterierne højere energi tæthed. Normale Li-S batterier benytter salte opløst i ioniske væsker som elektrolyt. Disse væsker er dog brandbare hvilket danner grundlag for bekymringer for sikkerheden af disse batterier og kan være årsag til udveksling af polysulfide der kortslutter batterierne. Ydermere, Li-metal er uegnet som anode materiale på grund af dendrit formation der begrænser levetiden af batterierne. En løsning på disse problemer er at erstatte den flydende elektrolyt med en faststof elektrolyt basseret på ikoniske faste stoffer. I dette projekt er to nye faste elektrolytter, $LiBH_4$-SiO_2 og $LiBH_4$-$LiBF_4$, blevet undersøgt som potentielle kandidater til fastestof Li-S batterier. Disse elektrolytter er blevet fremstillet og karakteriseret ved brug af teknikker som elektrokemisk impedans spektroskopi, Raman spektroskopi og nuclear magnetisk resonans. Høje joniske ledningsevner blev målt (0.1 mS/cm^{-1} at ved stuetemperatur).

Elektrolytten fremstillet af en $LiBH_4$-SiO_2 blanding har højere Li^+ ion ledningsevne sammenlignet med ren $LiBH_4$, helt op til en 1000 gange højere ved stuetemperatur, 10^{-7} S/cm^{-1}) . Disse undersøgelser fandt ikke nogen beviser for formationen af nye bulk phaser men bekræftede eksistensen af en interface mellem silicium og borohydrid med høj ledningsevne. Højst sandsynligt stammer denne fase fra en reaktion mellem $LiBH_4$ med overflade silicium silanol grupper. Raman og NMR målingerne viser tydeligt at blandingerne opfører sig anderledes for ren $LiBH_4$.

For $LiBH_4$- $LiBF_4$ blandinger med lavt $LiBF_4$ blev det forslået at Li^+ ledningsevnen opstår i $LiBH_4$ fordi den indeholder $LiBF_4$. For blandinger med højt $LiBF_4$, dekomponerer $LiBH_4$ hvilket

resulterer i laver ledningsevne. Li-S batteri baseret på $LiBH_4$-SiO_2 faststofelektrolytten blev bygget og testet. Disse batterier havde en kapacitet på 794 $mAhg^{-1}$ S efter 10 op- og afladninger ved 0.03 C ved 50 ^{o} C.

På baggrund af målte kapaciteter der under første op- og afladning er højere end teoretisk muligt, blev det undersøgt om det var muligt at beskytte S-katoden. Dette blev gjort via deponering af LiPON tyndfilm på katodes overfalde for undgå direkte kontakt med elektrolytten. Disse batteri havde mindre kapacitet men mistede mindre kapacitet over tid sammenlignet med batterier uden beskyttelsen. Samtidig forsvandt den højere end muligt målte kapacitet under første op- og afladning. Dette understreger vigtigheden af at beskytte katodens interface med elektrolytten i Li-S batterier.

Table of Content

List of figures

List of tables

Abbreviations

BTU	British Thermal Unit
CB	Carbon Black
CE	Counter Electrode
CPE	Constant Phase Element
CSA	Chemical shift anisotropy
CV	Cyclic Voltammetry
DFT	Density Functional theory
EDS	Energy-dispersive X-ray spectroscopy
EES	Electrical Energy Storage
EIS	Electrochemical Impedance Spectroscopy
EXFAS	Extended X-Ray Fine Absorption Structure
EXSY	Exchange Spectroscopy
FID	Free Induction Decay
FWHM	Full Width at Half Maximum
IR	Infra-Red
Li-S	Lithium Sulfur
MAS	Magic Angle Spinning
MCM-41	Mobile Composition of Matter No.41
NMR	Nuclear Magnetic Resonance
OCV	Open circuit voltage
PTFE	Polytetrafluoroethylene
PVDF	Polyvinylidene fluoride
RF	Reactive radio frequency
SEI	Solid electrolyte interphase
SEM	Scanning Electron Microscopy
SS-NMR	Solid-state Nuclear magnetic resonance
TEM	Transmission electron microscopy
TGA	Thermal Gravimetric Analysis
UV	Ultraviolet
WE	Working Electrode
XAS	X-ray Absorption Spectroscopy
XANES	X-ray absorption near edge structure
XRD	X-ray diffraction

Chapter 1

Introduction

1.1 Role of sustainable energy in modern world

Among different types of energy vectors, electricity is the most commonly used one worldwide, both in the residential and commercial sector.[1] The major sources of electric power are coal, natural gas, nuclear power, renewable sources and petroleum. Figure 1 shows distribution of global consumption of electric power by major sources in trillion ton BTU.

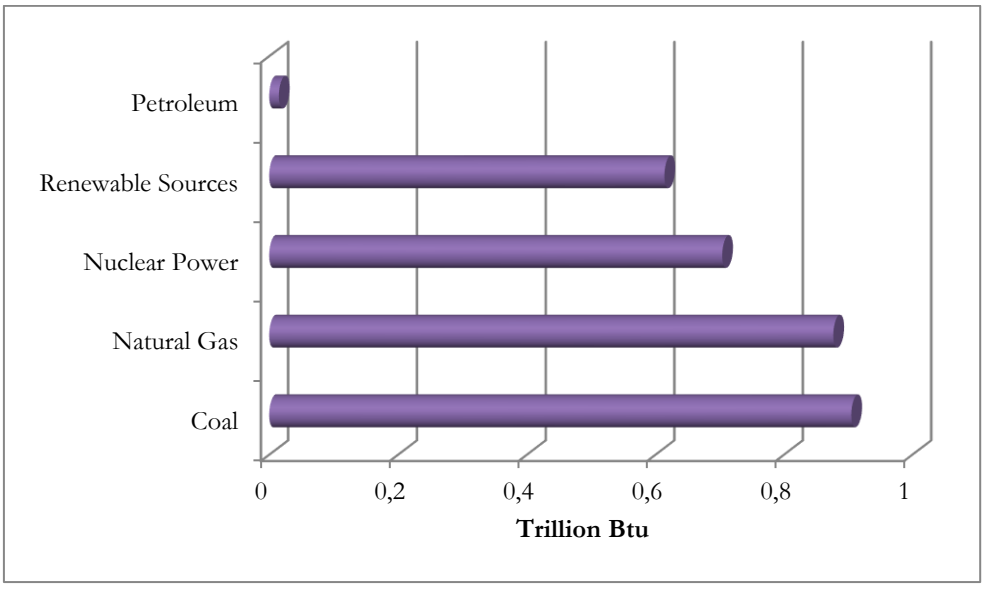

Figure 1 Electric power consumption in trillion ton btu by major source globally, May 2018 (reproduced from data [1])

For example, in May 2018, 80 % of the generated electricity in the world was produced from non-renewable sources, within a share of 23% from nuclear power and only 20% was produced from renewable sources. [1]

Emissions from burning fossil fuels cause various environmental and health problems on a global scale, such as acidification of oceans and pollutions in big cities, carbon dioxide is undoubtedly contributing to global warming while being dependent on gas or oil on a national level causes political and social instability. [2]

Data on greenhouse gas emissions from the Environmental Protection Agency (EPA) shows that since 1900 the levels of CO_2 and non-CO_2 greenhouse gases has increased as a consequence of industrial processes and burning fossil fuels. Figure 2 shows total carbon emissions since 1950 to 2015 and as it can be seen, it has increased by more than 90% since 1970. [3]

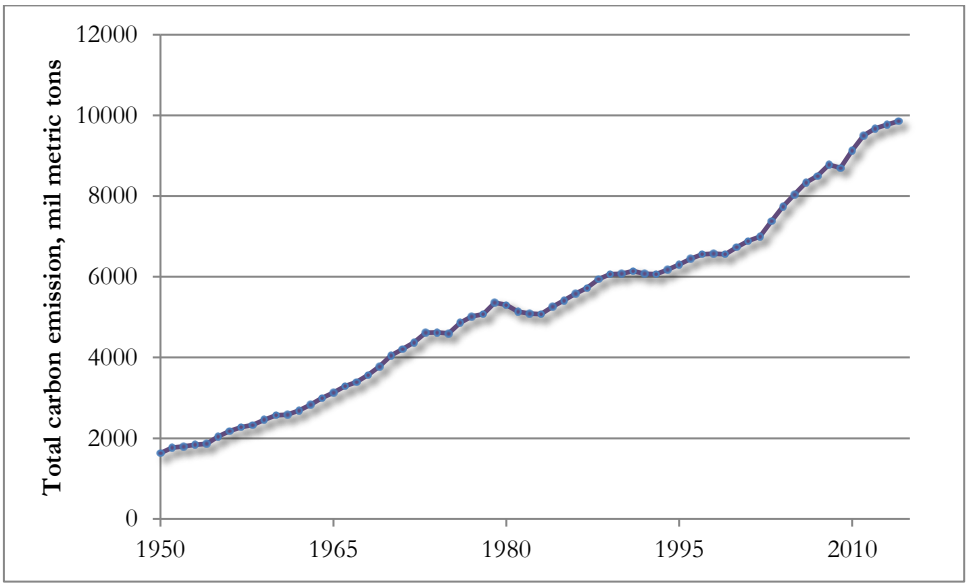

Figure 2. Global carbon emissions in millions of metric tons (data from Boden, et al [4])

In the recent decades, the energy sector has been in transition. Governments have realized the severity of the problem and concentrate on national and global initiatives to promote production of energy from renewable source and increase its utilization by using electric motors.[2] Figure 3 shows the difference in energy generation by source in 2013 and 2018 globally.

Figure 3 Distribution of generated electric power by source in 2013 and 2018. Blue represents non-renewable souces, red nuclear and green renewable sources
(Reproduced data from U.S. Energy Information Administration, 2018 [1])

While in 2013, 13% of generated electric power originated from renewable sources, in 2018 the share increased to 20% at cost of nuclear power and non-renewable sources. This shift towards "green" power had a positive effect on the level of carbon emissions. During a period from 2014 to 2016, little or no growth was observed in carbon emissions due to the increased share of renewable power on the energy market. However in 2017, the levels of CO_2 emissions increased by 1.7% as primary energy consumption increased by 2.2%[5]. This increase in carbon dioxide emissions is among other reasons, due to the insufficient growth of the renewable energy production to keep up with the ever increasing energy demand in the world. [2]

The production of energy from renewable resources such as wind or solar energy varies with time and therefore efficient electrical energy storage systems (EES) are required.[6] EES are especially important for future grid balancing services to make best use of available resources. This is an important issue for countries where the share of power generated from renewable sources is high. For example, in Denmark in 2017, 40% of generated electric power came from wind power[7]. Figure 4 shows the production of power from wind sources and a typical load curve for a winter day in Denmark[8].

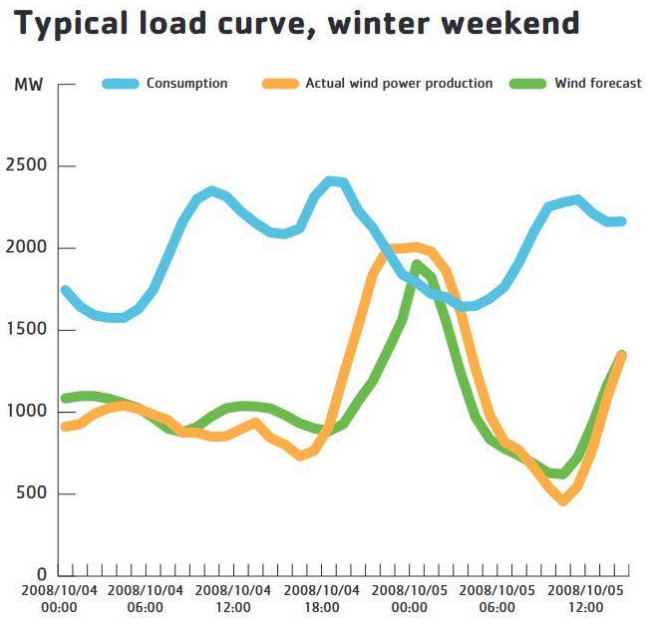

Figure 4 Wind production during a single day in Denmark (Reprinted from EnergiNet, 2017 [8])

As it can be seen from Figure 4, a mismatch power consumption (blue line) -and production (orange line) have caused overproduction and peak consumption. At hours during the night when the production exceeds the energy demand, the overproduced energy has to be sold at a low price on the market or balanced by frequency regulation. On the contrary, consumption peaks at early morning (8 am) and in the afternoon (6-7 pm) where the energy demand is twice as high as the production level, energy has to be bought on the market at high price. Although forecasts are made on the daily and hourly basis, it is not possible to make accurate predictions on energy production which is causing economic losses due to sales at low cost and frequency regulation where generated electricity cannot be used efficiently.

As the share of electric power generated from renewable source should increase, the mismatch between production and consumption will be even more important. In a prognosis by the Danish Ministry of Climate, it is predicted that by 2025, 50% of electricity in Denmark will be generated by wind power, while by 2050, the goal is set to 100% of electricity from renewable sources[8]. As shown in the example above, it is difficult to match energy demand and production and therefore integration of electricity storage (EES) devices on the grid, on a much larger scale is required. On possibility for EES is of cause to use batteries. In the next section, the most commonly used battery technologies will be discussed in detail.

1.2 Energy storage: Lithium-ion and lithium sulfur batteries

Before discussing batteries for energy storage applications, it should be noted that when it comes to electrical energy storage, the most common and cost-efficient way is the pumped-storage electricity whith prices as low as 10-20 USD/kWh associate with and high efficiency.[9] Globally, around 184 GWh are stored in pumped-storage hydroelectricity which is also the most common load balancing system due to its reactivity.[9] Pumped-storage hydroelectricity can be used with renewable energy sources, such as solar or wind, however the main disadvantage of hydroelectricity is that is requires a special nature of the site – typically mountainous regions are suited for hydropower as both reservoirs are needed together with a height difference. In the areas where water availability is low and the landscape is flat or where nature has a protected status, there is a need for storing energy in alternative ways, such as electric energy storage (EES). For example, batteries are commonly used for frequency regulation, peak shaving and wind ramp management.

When it comes to electric energy storage, primary concern is the energy and power density and price per unit of the above. Figure 5 shows specific energy and power density of common battery technologies based on data from 2013. [10]

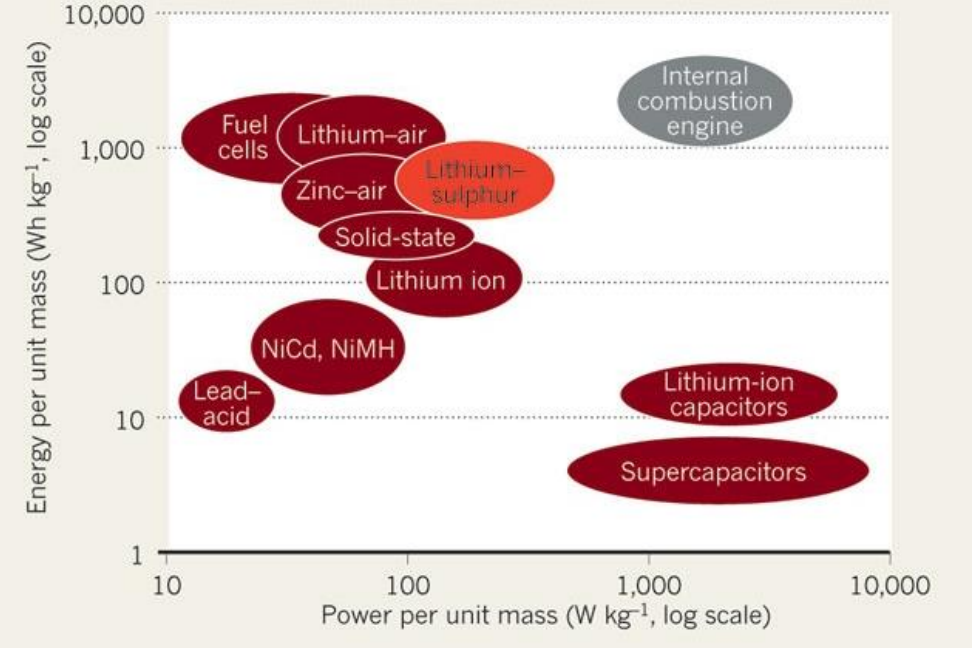

Figure 5. Specific energy and power density of common battery technologies on the market. Reprinted from van Noorden, 2013 [10]

While lead-based batteries are the oldest battery technology on the market, this type of battery is still the most commonly used.[9] They are well-suited for grid applications due to following major advantages:[9]

- Low installation and capital costs in range 50-200 $ per kWh[11]
- Life-time up to 15 years (if operated under optimal conditions)[12] [13]
- Low self-discharge rates per day and per month (around 2%)[13]
- Easy connection in large arrangement with no management systems required for operation

Because the world market for energy storage is expected to increase rapidly, due to the increase in renewable energies production, lead-based batteries are becoming less and less adapted compared to other technologies. The low cost of lead-based batteries does not win over its disadvantages on a large scale which includes following issues:

- specific densities that are much lower than that of competing technologies
- lead-based batteries have a significant limitation due to temperature dependence: a variation from optimal operating temperature (~25°C) can result in shortening of a life-time by a factor of 2.[9]
- Batteries should be charged at slow rates limiting their application in load leveling and peak shaving.

Li-ion batteries are an alternative to lead-based batteries and are among the most common battery types used today[14]. About 100 MWh are stored worldwide in Li-ion batteries connected to the grid for frequency regulation, peak shaving and load levelling[9]. Li-ion batteries have higher specific energy (150 to 200 $Whkg^{-1}$)[6] compared to other technologies, have efficiencies claimed to be up to 100% and long life time, high number of charge-discharge cycles.

There is a competition for leading technology on the MW-scale. While Li-ion technology has undergone significant improvement since its introduction in the 1990's, the limits of theoretical capacity of lithium-ion technology has been reached.[14] While improvements have been made, only marginal increment is expected and therefore there is a need for new technologies to respond to the growing energy demands in the world.

New battery technology offering higher energy densities are being explored; among them are lithium-sulfur batteries (Li-S). Compared to other emerging battery types, Li-S is one of the most

promising technology [6] as LiS batteries offer higher theoretical energy density (2700 $Whkg^{-1}$)[15] and theoretical capacity of 1672 mAh g^{-1} of sulfur [6] which is more than 10 times the specific energy of commonly used lithium-ion technologies that are currently on the market; 180 mAh/g for Lithium Nickel Cobalt Aluminum Oxide (NCA), 160 mAh/g for Lithium Nickel Manganese Cobalt Oxide (NMC), 160 mAh/g for Lithium Iron Phosphate (LFP)[16]. Lithium-sulfur batteries with specific energy of 400 Wh/kg have been achieved at cell level by Oxis Energy Ltd. [15], Sony is planning to introduce a lithium-sulfur battery in its mobile devices by 2020. [17] There is a variety of materials that are used on cathode and anode side in lithium-sulfur batteries and it exists solution based on liquid or solid electrolytes. This is discussed in detail in following chapters.

1.3 Batteries based on Solid state electrolytes

At present time, commonly used electrolytes in commercial li-ion batteries are organic liquid electrolytes, typically carbonates (dimethyl carbonate, ethylene carbonate or diethyl carbonate) [6] and gel-polymer electrolytes. These are good solvents for lithium salts. However they are flammable with flash point below 30 °C. [2] These are typically used with lithium salt $LiPF_6$, which is moisture and temperature sensitive[18] and undergoes autocatalytic decomposition into LiF and PF_5 at temperatures above 60 °C with PF_5 reacting with water and forming PF_3O and HF which leads to degradation of the batteries and raises safety concerns.[2]

Apart from being temperature and moisture sensitive, batteries with liquid electrolytes have another disadvantage, namely the formation of solid electrolyte interphase (SEI) on the anode side that is ionically conductive but electronically insulating and consumes both electrolyte and Li metal. Furthermore the SEI causes low coulombic efficiencies and poor reversibility of the electrochemical reactions. [19] Thick SEI will eventually cause Li dendrites to fall off the layer. Li diffuse through separator and cause internal short circuit. [19]

The solution to these safety issues would be using batteries built around solid electrolyte that have major advantages compared to liquid electrolytes:

- **Safety:** Solid electrolytes eliminate the risk of vaporization or electrolyte leakage. The need to monitor the temperature to avoid battery degradation is not so critical compared to batteries with liquid electrolyte;
- **Higher energy density:** by using solid electrolyte it is possible to make thinner batteries as solid state batteries do not require separators and can be made with minimum volume

of electrolyte. Furthermore solid electrolytes allow bipolar stacking which reduces the need of space.

- **Higher current:** as solid electrolytes will not ignite unlike liquid electrolytes at temperatures above flash point, it is possible to draw higher currents from solid-state batteries.
- **Lower costs of operation:** as temperature is not an issue for certain types of solid-state batteries cooling systems are not necessary. [20]

While lithium-ion cells are commonly used in electric vehicles on the market, car manufacturers are actively investigating the possibility to use solid-state batteries as an alternative in new vehicles. In 2017, the following driving ranges were achieved by some car manufacturers using conventional electrolyte: Tesla S (208-315 miles), BMW i3 (114 miles), Nissan Leaf (107 miles), Volkswagen e-Golf (124 miles).[16] While these ranges are longer than for the previous generations of electric cars, leading car brands are investing in solid-state battery research, for example:

- **Fisker:** have stated that its next-generation cars with solid-state batteries will have a driving range of 460 miles and a fast charging option to recharging the batteries in minutes. [21]
- **Hyundai:** Hyundai's subsidiary, Hyundai Cradle, is investing in Ionic Materials, a company using solid polymer materials in battery innovation. [22]
- **BMW:** has invested in Solid Power, a Colorado-based company producing batteries using inorganic solid state electrolyte. [20,23] Solid Power is planning to produce solid-state batteries with specific energy of 320-700 Wh/kg and specific power of more than 1000 W/kg. [20]
- **Toyota:** Toyota motors are planning to commercialize battery technology based on solid-state batteries and introduce a vehicle by early 2020s. [23]

Due to the growing interest in solid state batteries in industry, much research in the battery field is now focusing on solid state electrolytes. There are various families of compounds that have been tested as solid state electrolyte, among others sulfide compounds, e.g. GeS_2, P_2S_5[24], oxide/ oxinitrite glasses, such as LiPON[24], LISICON.[25] Sulfide solid-state electrolytes are difficult to prepare, furthermore they are easily oxidized after preparation.[24] LiPON and LISICON compounds have shown to be good Li^+ ion conductors with conductivities in the range from 0.1 to 1 $mScm^{-1}$, however the technology has significant drawbacks that limit their practical

application. These compounds are not stable against Li metal and it is difficulti to control their stoichiometry during synthesis. [26]

Complex metal hydrides, such as $LiBH_4$, $Mg(BH_4)_2$ and $NaBH_4$, have been considered as good candidates as solid-state electrolytes due to their high ionic conductivities.[27] $LiBH_4$ is a complex metal hydride that has been widely studied in hydrogen storage research due to its high hydrogen content (18.6 wt%).[28–30] In this work, $LiBH_4$ was chosen as solid-state electrolyte in combination with SiO_2 or $LiBF_4$, due to simple preparation procedures and higher conductivity values when compared to that of pure $LiBH_4$. We have successfully assembled and cycled lithium-sulfur batteries built around $LiBH_4$ as solid-state electrolyte, furthermore he mobility of lithium ions was studied in the electrolyte by a number of different techniques, including Nuclear magnetic resonance (NMR) and Raman spectroscopy.

1.4 Outline of the thesis

The thesis is divided into 6 chapters:

Chapter 1 Introduction describes the scope and purpose of the thesis.

Chapter 2 Theory gives an introduction on the working principle of Li-S batteries and explains the principles of ionic conduction in solids. The chapter also describes the theory behind the methods used in the experimental part.

Chapter 3 Experimental Techniques describes the details of the cell design, material preparation and setup for the experimental techniques that were used for data collection in paper I-III.

Chapter 4 Materials Preparation and Battery Setup describe the details of cell design, material preparation and setup of primary experimental techniques that were used for data collection in paper I-III.

Chapter 5 Results presents the results of the different experimental studies performed on $LiBH_4$-SiO_2 and LiBh4-LiBF4 electrolytes and all-solid-state lithium-sulfur cells built around $LiBH_4$-SiO_2 electrolyte.

Chapter 6 Conclusion presents the conclusions of the PhD project and gives an outlook of the results.

1.5 Articles

Paper I

Lithium Conductivity and Ions Dynamics in $LiBH_4/SiO_2$ Solid Electrolytes Studied by Solid-State NMR and Quasi-Elastic Neutron Scattering and Applied in Lithium-Sulfur Batteries

Jessica Lefevr, Luca Cervini, John M. Griffin, and Didier Blanchard

Contribution: experimental work on NMR, battery cycling and impedance measurements.

Paper II

Ions Dynamics in $LiBH_4/SiO_2$ Solid Electrolytes Studied by Solid-State NMR

Jessica Lefevr, Luca Cervini, John M. Griffin, and Didier Blanchard

Contribution: experimental work on NMR.

Paper III

Ions Dynamics in $LiBH_4/LiBF_4$ Solid Electrolytes Studied by Solid-State NMR

Jessica Lefevr, Luca Cervini, Peter N'Gene, John M. Griffin, and Didier Blanchard

Contribution: experimental work on NMR.

Chapter 2

Theory

2.1 Principle of operation of Li-S batteries

A conventional Li-S battery consist of the following components[14]:

- **Negative electrode:** Lithium (either metal or composite materials made of C-Li, Si-Li, Si-C-Li or other compounds). Lithium is the lightest metal in the periodic table and lightest solid element and for that reason is well suited for battery applications. [31] While ideally pure lithium metal can be used as anode, battery manufacturers use C-Li to prevent lithium reaction with liquid electrolytes.
- **Electrolyte:** typically made of non-aqueous organic solvent based on single solvents or binary/ mixtures of ethers[18] and lithium salts such as $LiPF_6$. [31]
- **Separator:** a conductive polymer, such as polyaniline or filter paper;
- **Positive electrode**: Due to insulating nature of sulfur, it is typically used in a matrix of carbon material that is lightweight and is highly electronically conductive. A binder, typically polyvinylidene fluoride (PVDF), or polytetrafluoroethylene (PTFE) are used to ensure adhesion between the electrode materials and the current collector.

Typical U-I curve for Li-S battery with liquid electrolyte is shown in Figure 6. As it can be seen, solid S_8 undergoes transition from solid to polysulfides dissolved in electrolyte and precipitates back as Li_2S or Li_2S_2.

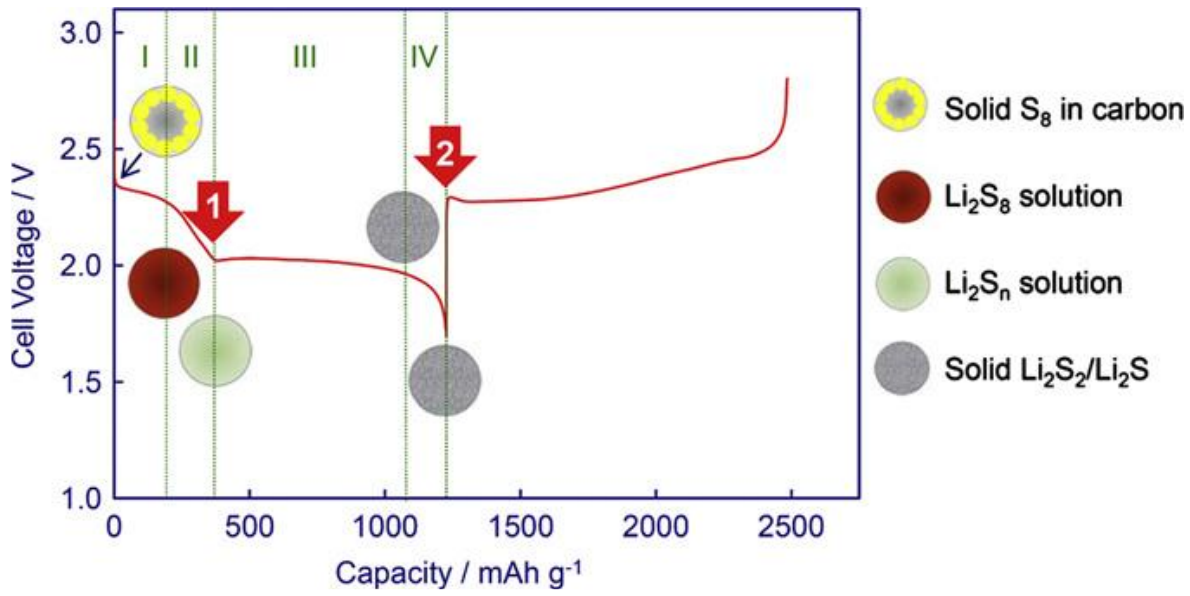

Figure 6 Principle of operation of a Li–S battery

(reprinted from Zhang, 2013[32])

The overall reaction that is taking place can be written as:

$$S_8 + 16Li = 8Li_2S \qquad \text{Eq. 1}$$

As it can be seen in Figure 6, the discharge occurs in the following steps[33]:

- 2.4 - 2.3 V vs. Li/Li^+: sulfur is reduced to high order polysulfides, Li_2S_n where n >4, in following order:

  $$S_8 \rightarrow Li_2S_8 \rightarrow Li_2S_6 \rightarrow Li_2S_4 \qquad \text{Eq. 2}$$

  Dissolved sulfur forms polysulfides and diffuse in the battery, ready to react in the next step;

- 2.3 - 2.1 V vs. Li/Li^+: high order polysulfides are reduced to Li_2S_2
- < 2.1 V vs. Li/Li^+: high order polysulfides are further reduced to Li_2S_2 and Li_2S. Short chain polysulfides and the final discharge product, Li_2S, is insoluble and precipitates on anode until the surface is fully covered [34].

During charge, the formation of S_8 occurs from Li_2S in flat voltage plateau region and various intermediate species have been reported in the literature.[19] Overall, during discharge, polysulfides starting from Li_2S_4 undergo transformation from in the dissolved state and then precipitate at lower voltages.[35]

2.2 Strategies for improvement of lithium-sulfur batteries

Li-S batteries have some major issue related to polysulfide shuttle and formation of SEI layer. [19] Following strategies are commonly applied in research to overcome limitations of li-s technology:

Modification of the cathode side:

- Encapsulation of S: encapsulation in carbon scaffolds ensures that the reactions between lithium and sulfur is occurring in the scaffold; [19] thus preventing the shuttling of the polysulfides.
- Functionalizing sulfur: various groups are used (oxygen, nitrogen and boron functional groups) to avoid shuttle effect. [14] Figure 7 shows an example of functionalizing sulfur with nitrogen groups thus creating strong bonding between N and Li cations and preventing polysulfides dissolution in the electrolyte and the resulting polysulfide shuttlinge;

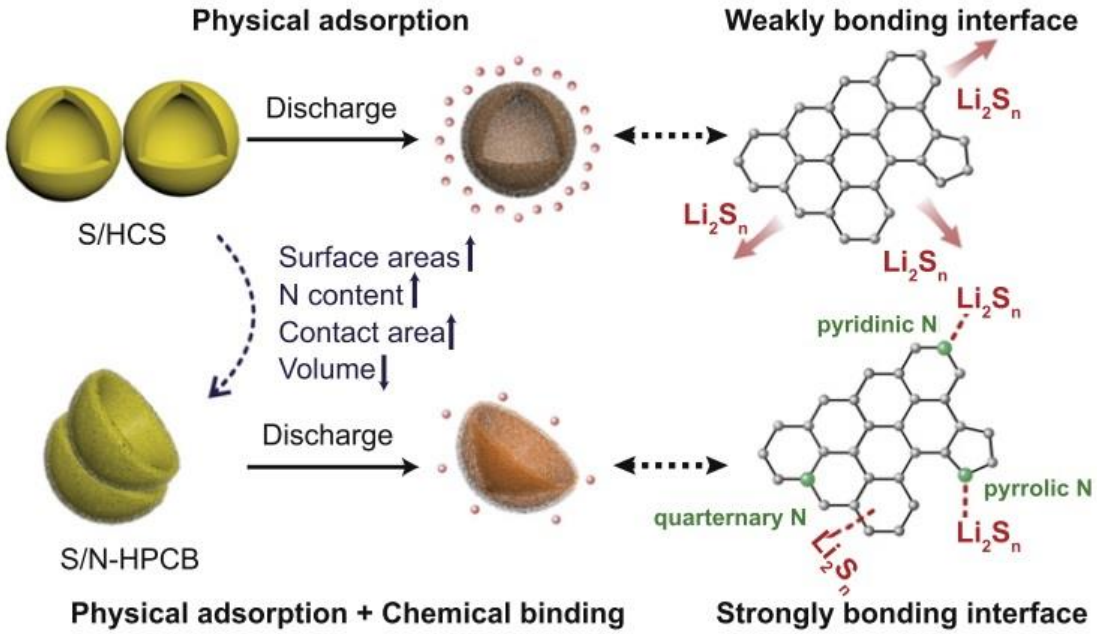

Figure 7 Functionalizing sulfur using nitrogen functionalized groups (Reprinted from Fan, et al 2017[14])

Modification of electrolyte:

- Ionic liquids are considered by some researchers as the ideal alternative to commonly used organic solvents, thanks to their high conductivities and non-volatility. However at present time they are expensive, even for large-scale production and pose a health threat due to their high toxicity;[36]
- Polymeric electrolytes: short-chain polymeric electrolytes such as Tetraethylene glycol dimethyl ether (TEGDME) [6]
- Solid-state electrolytes: include among others members of LISICON family, $Li_2S - P_2S_5$ glasses, and $Li_{10}GeP_2S_{12}$.[6] Solid-state electrolytes have many advantages compared to liquid electrolytes in terms of blocking shuttle effect and reducing solubility of polysulfides, furthermore, they are protecting the cathode and reducing the formation of dendrites. As for the disadvantages, solid-state electrolytes normally have low ionic conductivities due to high energy barriers for Li ion transport in solids

2.3 Ionic conduction in 'point defect type' solids

The process of ion transport in ionic solids has been well studied.[37] For a crystalline solid with perfectly arranged atoms in its crystal lattice, one does not observe any ion transport since a direct exchange of places between neighboring cations and anions is highly unlikely. For example, for NaCl- the energy required for a direct exchange between two neighboring cation and anion, as shown in Figure 8, is around 15 eV and the possibility of this event to occur in one gram of salt is as low as every 10^{30} years. [38]

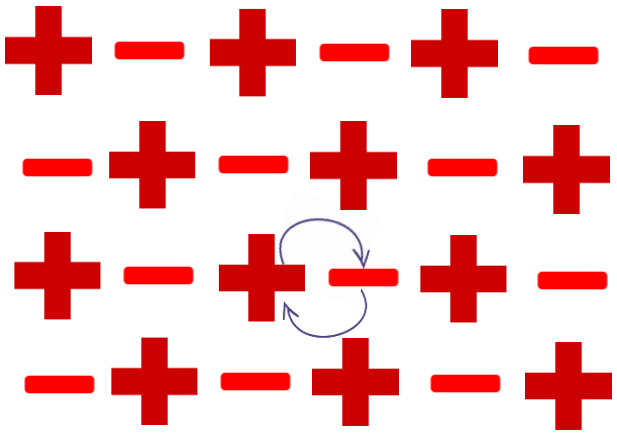

Figure 8 Exchange between neighboring cations and anions in a perfect crystal (reproduced from Chandra [37])

Ionic conductivity in regular crystal lattices by direct substitution is unlikely to occur and therefore must be mediated by defects present in the lattices. The two most likely types of defects in lattices are:

- **Schottky Defects:**

In lattices with Schottky defects, cations and anions move to existing vacancies as illustrated in Figure 9. This mechanism is commonly referred to as "vacancy mechanism".

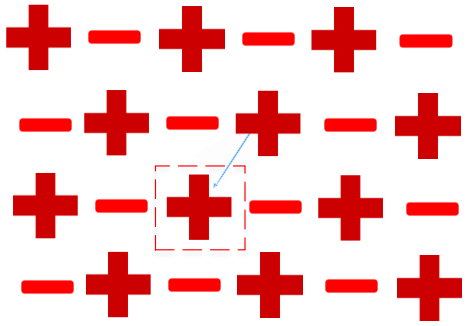

Figure 9 Vacancy mechanism (reproduced from Chandra [37])

- **Frenkel defects:**

For lattices with Frenkel defects, ionic transport is mediated by interstitial jumps, either from interstitial sites to interstitial sites, as shown in Figure 10(left) or by jumping into normal sites and pushing atoms into interstitial sites Figure 10 (right). The former is referred to as "interstitial" mechanism while the latter as "interstitialcy" mechanism.

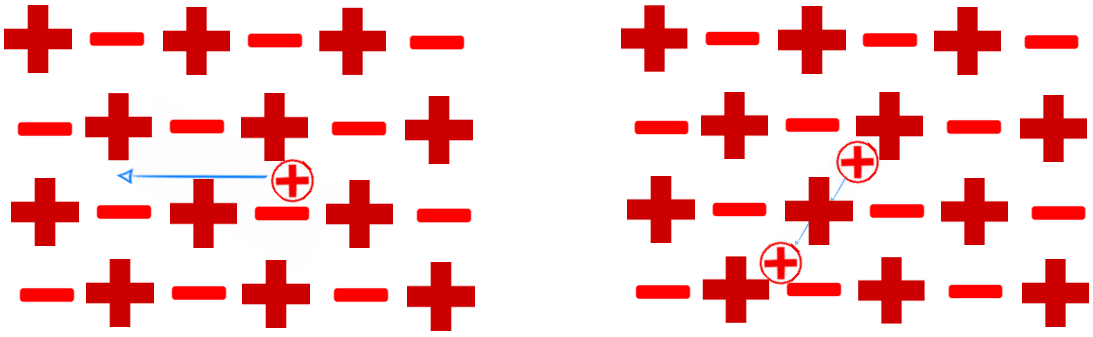

Figure 10 Interstitial (left) and interstitialcy mechanisms (right) (reproduced from Chandra [37])

Ion transport in solids is determined by a jump probability of an ion in a lattice defect. This probability depends on two factors:

- Jump frequency, ω, which is a probability of ion to jump in a lattice defect in a given time unit. Jump frequency depends on the energy barrier seen by the ions.
- Probability of a site having a defect in a closest neighbor site. This probability can be found as a product of mole fraction of defects and number of closest neighboring sites.

Jump frequency, ω, can be calculated using different approaches but its final form can be written as[37]:

$$\omega = \nu_0 \exp\left(-\frac{Ea}{kT}\right) \quad \text{Eq. 3}$$

where Ea is the free energy barrier between positions of saddle-point of ions and lattice site position and υ_0 is the vibrational frequency of equilibrium positions.

Equation (3) is valid for cases where ions can jump freely, i.e. this are no correlated jumps in the crystal lattices.

Diffusion coefficient can be calculated as:[39]

$$D = \frac{1}{6}\Gamma r^2 \quad \text{Eq. 4}$$

Where Γ is the random jump of a particle in a unit of time, r is the length of a jump.

2.4 Conductivity in Heterogeneous Solid Electrolytes

In this section, the ionic properties of heterogeneous solid electrolytes including ionic conductors and insulating oxides are discussed. The ionic conductivity of pure $LiBH_4$ is detailed and some of the strategies to increase it at room temperature, by making binary systems with halides, oxides and carbon matrices are discussed.

2.4.1 Space-charge Model

While defect chemistry and bulk conductivities of ionic conductors are well-studied, ion transport properties of heterogeneous systems are not fully understood.[40] It is often considered that properties of non-uniform systems are the superposition of the properties its constituents, however new effects are often found in multiple phases heterogeneous conductive solids, showing that the properties of a system are not a simple addition of the properties its components. In the literature, there are different models to explain the increased conductivity obtained when mixing for example lithium salts and insulating oxides. Therefore, there is a need to explain unambiguously the phenomenon and create a robust model to use for the analysis of experimental data. [41]

The effects of mixing ionic conductors with oxides, such as SiO_2, ZrO_2, Al_2O_3, Fe_2O_3, have been known for nearly 50 years. Such effects have also been observed for systems with two ionic conductors, e.g. metal halides such as a mixture of silver iodide and silver bromide; however X-Ray studies have not shown evidence of new phases being formed in such mixtures.[40] Difference in conductivities of mixtures may occur by two mechanisms:

- **Core region mechanism**: Novel conductive path in the core region characterized by novel migration enthalpy
- **Space charge layer mechanism**: Conductive path due to a change in defect concentrations formed as a result of interface interactions

While the core region mechanism is a very specific problem, the space charge mechanism is a general mechanism that can be applied to various heterogeneous systems. This mechanism will occur due to thermo- and electro-static reasons and two cases can be considered:

- **Single interface or Bicystal:** in cases where the contact surface between two phases is considered to be a rectangular plane, i.e. the two phases are forming a bicrystal, extra conductance that is parallel to the interface between the phases. There is also a perpendicular contribution for the conductivity that needs to be considered, however for modelling of impedance spectra, fitting effective parallel capacitor gives good agreement with obtained results.[40]

- **Two phase mixtures:** for two-phase systems, the transport properties will differ in the bulk, boundary layer and grain boundaries of the conductive phase. A realistic model of the two-phase system with a lot of interfaces can be given as a three dimensional network with conductivity pathways formed in grains of an ionic conductor made by clusters of particles of a second phase that is an insulator. Impedance plots of two phases mixtures show two separate contributions: the high frequency branch that is originating from the bulk and parallel conduction pathways and lower frequency branch from the contribution of the core region and series boundary layers. In some studies, it has been shown that space charge regions are formed under free surfaces as a result of charge accumulation at the surface, however there is controversy in the literature regarding the sign of space charge layer even for well-understood materials, furthermore the systems are not well-defined from point of view of thermodynamics.[40]

The space charge layer model will be used in this work to model $LiBH_4$-SiO_2 composites that will be discussed in details in Section 3.4.2.

2.5 Lithium Borohydride ($LiBH_4$) as Li ion conductor

$LiBH_4$ has been widely studied a possible material for solid state hydrogen storage because of its high hydrogen content (18.6 wt% H_2). It is widely use as reductant in industrial chemistry. Recently it has drawn attention as a material well suited for solid-state batteries because it is lightweight and has high ionic conductivity (~ 1 $mScm^{-1}$) in its high temperature (T > 381 K) polymorph..[27]

At room temperature, $LiBH_4$ has an orthorhombic symmetry (space group P*nma*) and low ionic conductivity in the range of 10^{-6} - 10^{-8} $mScm^{-1}$. [42]At temperatures above 381 K, it undergoes a phase transition and crystallizes in a hexagonal structure (space group $P6_3mc$).[43] Figure 11 displays the crystal structure of $LiBH_4$ before the phase transition (left) and after the phase transition (right).

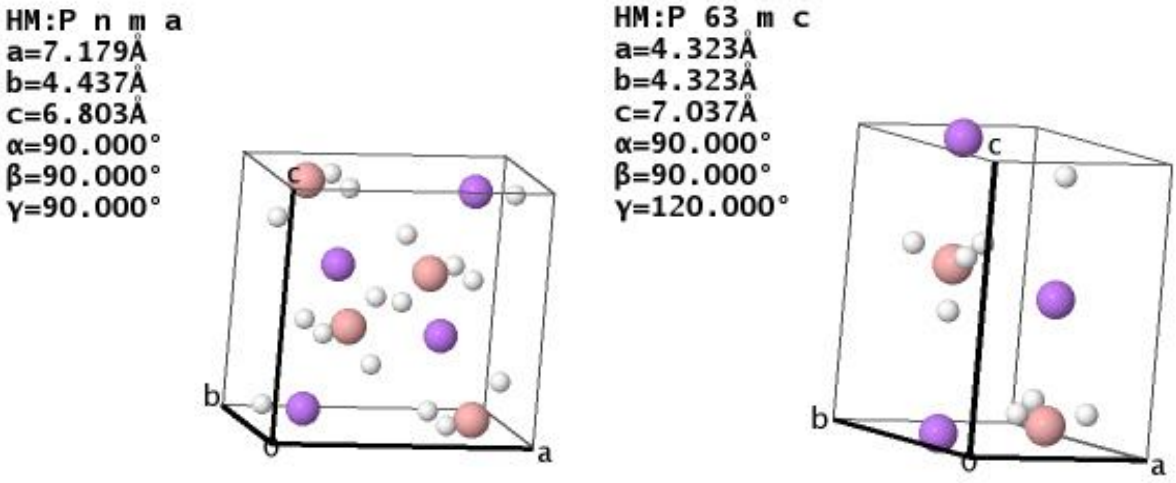

Figure 11 $LiBH_4$ crystal structure before (-Pnma, left) and after the phase transition ($P6_3mc$, right)

While pure $LiBH_4$ is a poor Li ion conductor at room temperature, an increase of two orders of magnitude is observed above the phase transition temperature.[44] The effect of heating is reversible and once $LiBH_4$ is cooled below the phase transition temperature, the conductivity drops with more than 3 orders of magnitude. Various attempts have been made to increase Li ion conductivity of pure $LiBH_4$ at room temperature. The common ways to achieve high ionic conductivity of $LiBH_4$, by making binary mixtures or reducing particle size of $LiBH_4$ via nanocofinement, will be discussed in detail in the following section.

2.5.1 Modifications of LiBH4 for high ionic conductivity

Several strategies are commonly used to increase conductivities of pure $LiBH_4$. These include creation of solid solutions with halide, confinement of $LiBH_4$ in nanostructures (carbons or mesoporous silica structures) or mixing $LiBH_4$ with insulating oxides.[45]

Solid solution with lithium halides, such as chloride, iodide and bromide, has shown to decrease phase transition temperature for $LiBH_4$. It was shown by Maekawa, et al[46] that addition of lithium halides stabilizes the hexagonal phase at room temperature leading to a significant increase in Li ionic conductivity. As predicted by Maekawa, et al[46], $LiBH_4$-LiI has the highest conductivity values at room temperature among other $LiBH_4$- halide systems and Matsuo, et al[45] and Sveinsbjörnsson, et al[47] investigated the performance of $LiBH_4$-LiI solid-state electrolyte. Matsuo, et al[45] assumed that the higher ionic conductivity of iodide solid solution is due to replacement of the borohydride anion by iodide anions which stabilized is the system. Myrdal et al [48] have performed DFT calculations on vacancies and interstitials in $LiBH_4$ – LiI solid solutions showing that the formation energy for defect pairs, Frenkel defects, starting from a defect-free system is as low as $E_{Frenkel} = 0.44$ eV and that the concentration of Frenkel pairs is $\sim 5 \cdot 10^{18}$ cm^{-3}. As the formation energy of vacancies and interstitials is very low, the conduction mechanism by which ion transport is mediated is vacancy diffusion. The most favorable jump mechanisms and rates calculated by Myrdal et al [48] are shown in Table 1:

Table 1 Calculated favorable jump rates for Li^+ ions in $LiBH_4$-LiI solid solutions

Jump mechanism	Jump rates, s^{-1}
Li^+_{int} 1/3 to 1/3	$8{,}3 \cdot 10^9$
I^- to BH_4^-	$9{,}8 \cdot 10^8$

The calculations performed by Myrdal et al [48] show that most favorable jumps are taking place in the hexagonal plane and therefore the diffusion can be considered as two dimensional.

Apart from mixing $LiBH_4$ with halides, another approach has been used namely confinement of $LiBH_4$ in scaffolds with nanosized pores, for example in carbon scaffolds or in mesostructured silica MCM-41. For example, in a study conducted by Liu, et al, $LiBH_4$ has been confined in nanoporous carbons (NPCs) with pores in nanometer range.[49] NMR and Raman spectroscopy studies of nanoconfined $LiBH_4$ have shown that the confined Li has different mobility than

that of pure $LiBH_4$. As neither NMR or QENS results have proven that a clear solid-solid phase transition has occurred, it was concluded by Liu, et al[49] that the effect is due to particle size reduction in the pores of the carbon scaffolds. Confinement of $LiBH_4$ in mesoporous silica scaffold have been used by Das, et al [50] who have successfully cycled batteries with $LiBH_4$-MCM 41 solid state electrolyte.

Finally, attempts have been made to achieve high ionic conductivity of $LiBH_4$ at room temperature by using oxides, Al_2O_3 [51], ZnO [52] and SiO_2. [53] The increase in conductivity that can be achieved by mixing an ionic conductor with insulating oxides.[54] The exact mechanism of conductivity in $LiBH_4$ – oxide systems is unknown, however many researchers are assuming that the effect is due to particle size reduction and formation of defects in crystal lattices close to insulating particles.[55]

In this work, we have studied the mechanism behind the conductivity in $LiBH_4$-SiO_2. We needed to consider the nature of the surface of the SiO_2 particles as well to understand the "cogwheel" mechanism of condu3ctivity in lithium salts. This is discussed in details in the following two chapters.

2.6 Surface Chemistry of Silica Particles

In order to understand the origin of high conductivity of $LiBH_4$-SiO_2 composites, it is important to consider surface properties of amorphous SiO_2. In this work, we will consider the Zhuravlev model[56] for surface chemistry of amorphous silica. In Zhuravlev model, [56] groups on surface of silica particles are divided into following subgroups:

- Single silanols (≡ SiOH): are isolated, free OH groups

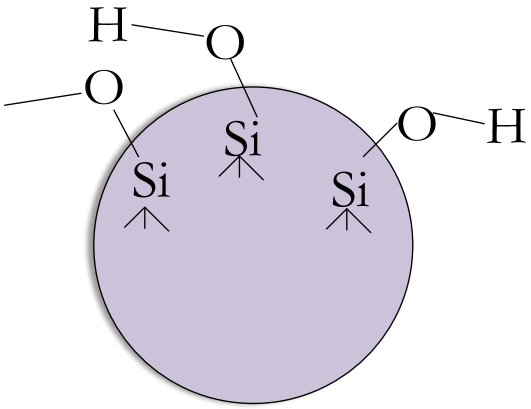

Figure 12 Silanol groups on the surface of a silica particle

- Geminal silanols, also referred to as silanediols (= $Si(OH)_2$)
- Vicinal or bridged silanols (silanols that are bonded through H bonds)
- Siloxane groups: exist on surface of silica as ≡Si-O-Si≡ (bridge with oxygens on silica surface)
- Internal silanol groups (structurally bound water in silica skeleton)

The hydroxyl groups on the surface of silica are formed during synthesis process of silica where $Si(OH)_4$ undergoes condensation polymerization reactions or rehydroxylation reactions: ≡Si-O-Si≡ interacting with H_2O and forming ≡Si-O-H groups on the surface of silica particles. Hydroxyl groups are also formed during rehydroxylation of silica, when dehydroxylated SiO_2 particles come in contact with aqueous media.

The ratio between groups changes as a result of thermal treatment and there is evidence of interaction between groups.[56] When silica is heated in vacuum ratio between the number of silanol and siloxane groups is changing. In Zhuravlev model, silanol number, i.e. number of OH groups per surface area of silica (α_{OH}), is a function of temperature during the process of thermal treatment of silica. The main stages of the surface composition are shown in
Table 2. [56]

Table 2 Main stages of surface of amorphous silica with heating

Heating temperature	Effect on silica
Initial state: 298 K, in vacuum	All groups described above are present on the surface. Maximum degree of hydroxylation of silica surface (α_{OH}=4.60 OH nm^{-2}). Physically adsorbed water covers surface of silica. Internal hydroxyl groups are present in silica skeleton.
Heating to 463K, in vacuum	In the beginning of the stage single layer of water, but towards the end of this stage, water monolayer is completely removed from the surface of silica. Surface is still in highest degree of hydroxylation (α_{OH}=4.60 OH nm^{-2}) and internal OH groups are still present in silica skeleton.
Heating to 673K, in vacuum	Decreased hydroxylation of surface is observed (4.60 ≥ α_{OH} ≥2.35 OH nm^{-2}). Internal OH groups disappear with increased temperature. With increased temperature, the concentration of vicinal OH groups decreases (2.80 to 0.0 OH nm^{-2}) until they disappear completely at the end of the stage.
Heating to 1173K, in vacuum	Decreased hydroxylation of surface, however the rate is different for isolated (5.05 ≥ α_{OH} ≥0.4 OH nm^{-2}) and genimal groups (0.3 ≥ α_{OH} ≥0.0 OH nm^{-2}) which are the only OH groups present on the surface of silica. At temperatures close to 1173, internal OH groups and geminal OH groups disappear.
Heating to 1473K	Concentration of siloxane bridges on surface of silica particles is increasing. At the end of the stage, all OH groups are removed from the surface of silica particles.
Heating above 1473K	Only siloxane bridges are present on the surface of silica

Zhuravelev model can be useful describing dehydration, dihydroxylation and rehydroxylation and can be applied to various materials containing OH groups on their surface (e.g. solid oxide substances).

2.7 Paddle-Wheel mechanism of conductivity

It has been debated that cations diffusion can occur by multiple mechanisms and are not limited to hopping between certain lattice positions as it was described above. The alternative mechanisms include that certain types of anions reorientation can promote diffusion of cations. The phenomenon was studied by Lunden who observed the so-called "paddle to wheel" or "cogwheel" effect in lithium sulfates[57]. Lunden stated that the high-conductivity of lithium sulfates could be due to the rotation of the sulfate anion "pushing" the smaller cations thus providing a new pathway for conductivity. Similar to lithium sulfates, an increase in ionic conductivity for mixtures of $LiBH_4$ and oxides could be a case where similar "pushes" are observed thus resulting in higher ionic conductivity. Figure 13 is illustrating the paddle wheel concept on the example of BH_4 anion showing rotary motion of the anion and Li^+ being pushed by the anion. Eventhough this "paddle to wheel" mechanism still remains controversial, it is clear that the high Li^+ conductivity is always accompagnied by high mobilitof their anions counterpart.

.

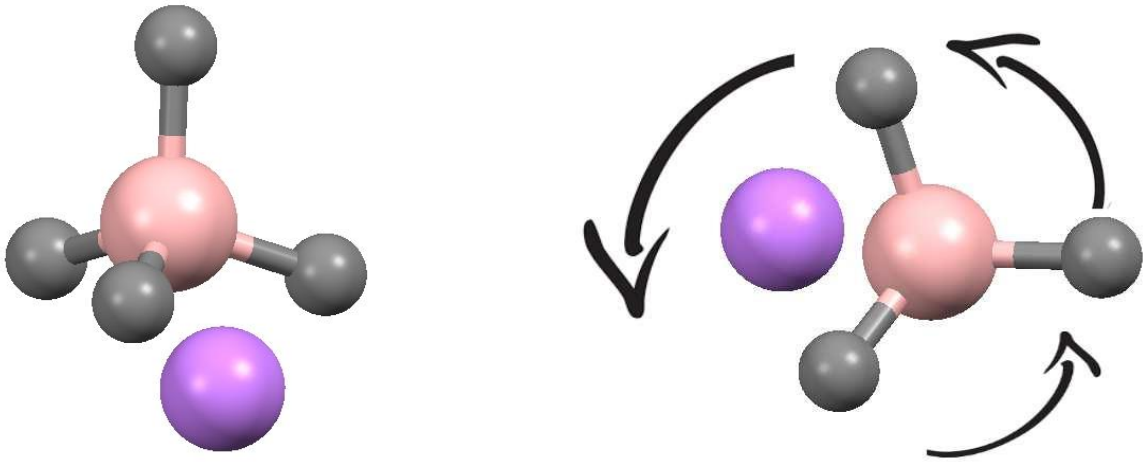

Figure 13 Side view of BH_4 anion with Li+ (left) and top view of BH_4 showing rotary motion

As shown in Figure 13, faster reorientations of BH_4 anion will increase the probability of lithium cations exchange between orthorhombic and hexagonal lattice positions. Similar effect if observed in lithium sulfides where Li ions are most likely exchanging between tetrahedral and octahedral lattice positions.[57]

Chapter 3

Experimental Techniques

This chapter presents the techniques that are commonly used in material science and battery testing, including electrochemical testing, impedance measurements, Scanning Electron Microscopy (SEM), Transmission electron microscopy (TEM) and some more specialized techniques that were used to study the ion mobilities in the solid-state electolytes, including nuclear magnetic resonance (NMR), Raman spectroscopy and others for imaging and structural characterization such as X-Ray diffraction (XRD) and synchrotron-based techniques, such as Extended X-Ray Fine Absorption Structure (EXFAS) and X-ray absorption near edge structure (XANES).

3.1 Battery operation

In a 2-electrode setup, the electrochemical cells consist typically of the following components separated by the electrolyte:

- **Working electrode (WE):** electrode where the reaction of interest takes place, e.g. sulfur in case of Li-s batteries
- **Counter electrode (CE):** is the auxiliary electrode that provides the circuit over which the current is applied. The area of the counter electrode is normally larger than the area of the working electrode to make sure that a half-cell reaction occurring at the counter electrode is not acting as a limiting step for the reaction occurring at the working electrode.

The overall reaction in a cell can be written as:

$$OX + ne^- \leftrightarrow RE \quad \text{Eq. 5}$$

Where *n* is the number of electrons transferred in the reaction.

In the cell, the voltage is measured during the reaction. The Nernst Equation can then be used to determine the voltage of an electrochemical cell at OCV:

$$E = E^{0\prime} + \frac{R_g T}{nF} ln\left(\frac{C_{ox}}{C_{re}}\right) \text{ Eq. 6}$$

Where E is the cell voltage, $E^{0'}$ is the formal potential, adjusted with activity coefficients for oxidized and reduced species, R_g is the gas constant, F is the Faraday constant and C is the bulk concentration of oxidized or reduced species.

During charging or discharging of a battery, the measured voltage, $E_{measured}$, will be different from voltage at OCV condition due to ohmic losses, electrochemical reactions in the battery and diffusion of different charge carriers. The difference between $E_{measured}$ and OCV can be founds as:

$$\boldsymbol{E_{measured}} = E_{OCV} - \text{IR} - \eta_R - \eta_D \text{ Eq. 1}$$

Where E_{OCV} is the potential measured at OCV condition, η_R is the charge-transfer resistance and η_R is the diffusion processes in the battery

The three components in the equation are explained as follow:

- IR: is the ohmic loss in the battery from all the resistances resulting from battery design, e.g. electrode surfaces, grids, interphases in a battery, ionic conductivity of electrolyte and electron conductivity of active materials.

- η_R: is the reaction overpotential that is occurring due to charge-transfer resistance which can be found from Butler-Volmer equation in its general form [58]:

$$I = A\, i_o \left(\frac{C_{Ox}}{C_{OX}^0} \cdot \exp\left(\frac{a\, n\, F\, n_{Reaction}}{RT}\right) - \frac{C_{Red}}{C_{Red}^0} \cdot \exp\left(\frac{-(1-a)\, n\, F\, n_{Reaction}}{RT}\right)\right) \text{ Eq. 8}$$

  Where I is the electrode current, A is the active surface of the electrode, i_0 is the exchange current density, a is the dimensionless symmetry factor for charging and discharging, n is the number of the electrons involved in the reaction at the electrodes, F is the Faraday constant, R_g is the gas constant, T is the absolute temperature, $n_{Reaction}$ is

overvoltage of the reaction, C_{Red} and C_{Ox} are concentrations of reducing / oxidizing ions in the electrolyte and $C^o{}_{Red}$ and $C^o{}_{OX}$ are concentrations of reducing / oxidizing ions in the electrolyte at equilibrium.

There are two liming cases of Butler-Volmer equation:

- High overpotential region: For very larger overpotentials, Butler-Volmer equation can be simplified as Tafel equation[58]:

$$Cathodic\ reaction: E - E_{eq} = a_{\ Cathodic} - b_{\ Cathodic} \log(i) \quad \text{Eq.9}$$

$$Anodic\ reaction: E - E_{eq} = a_{\ Anodic} + b_{\ Anodic} \log(i) \quad \text{Eq. 10}$$

Where *a* and *b* are reaction's Tafel equation constants (for a given temperature)

- Low overpotential:

$$i = i_0 \left(E - E_{eq}\right) \frac{nF}{RT} \quad \text{Eq. 11}$$

- η_D: is the diffusion overpotential resulting from concentration gradients of the electrolyte.

$$\eta_D = \frac{RT}{nF} ln\left(\frac{C}{C_o}\right) \quad \text{Eq. 12}$$

Where *C* and C_o are the actual and equilibrium ion concentration in the electrolyte

3.2 Galvanostatic Cycling with Potential Limitation (GCPL)

A common way to study battery performance is by doing Galvanostatic cycling with potential limitation (GCPL). During this type of cycling, a battery is charged and discharged in a given voltage range and at a given C-rate which is a measure of how fast a battery can be charged or discharged in respect to its capacity. For example C-rate of 1 C means that a battery can be charged or discharged in 1 hour while rate of 0.1 C means charge/discharge of 10 hours.

Two common indicators of the performance of a battery are the coulombic efficiency and discharge capacity retention. Coulombic efficiency is the ratio between discharge and charge capacity:

$$\eta_{Ah} = \frac{Q_D}{Q_C} \quad \text{Eq. 13}$$

Where Q_C and Q_D are the charge and following discharge capacities

Discharge capacity retention can be calculated as a ratio of discharge capacities between cycles and can be calculated as:

$$\Delta Q_{Discharge\,(J)} = \frac{Q_{Discharge\,(J)}}{Q_{Discharge\,(J-1)}} \quad \text{Eq. 14}$$

While coulombic efficiency is showing irreversible losses in a cell, the discharge capacity retention can serve as an indication of state of health of battery after cycling.

3.3 Cyclic Voltammetry (CV)

Cycling voltammetry is a sweeping technique that allows to study electrochemical processes in a battery by sweeping the electrodes potential between two given limits (E_1, E_2) and at a certain given rate, ν. [59] In potential sweep techniques, it is common that when reaching the limit E_2 the sweeping of the potential is reversed and on reaching the initial potential E_1, the sweep is reversed once more, halted or set to a new value E_3. Typically, in a CV experiment, electrode potential is being ramped with time in cycles with a set potential sweeping rate as shown in Figure 14.

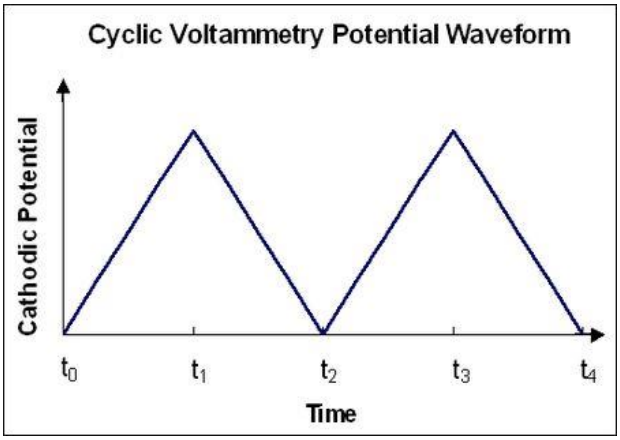

Figure 14 Cyclic voltammetry as a series of forward (t_0 to t_1) and reverse scans (graphics by Timothy M. Paschkewitz/ Wikimedia Commons /CC-BY 3.0)

While the potential is ramped on the working electrode, the current on working electrode is measured and plotted as a function of valtage. A typical Voltammogram of a Li-s battery is shown in Figure 15.

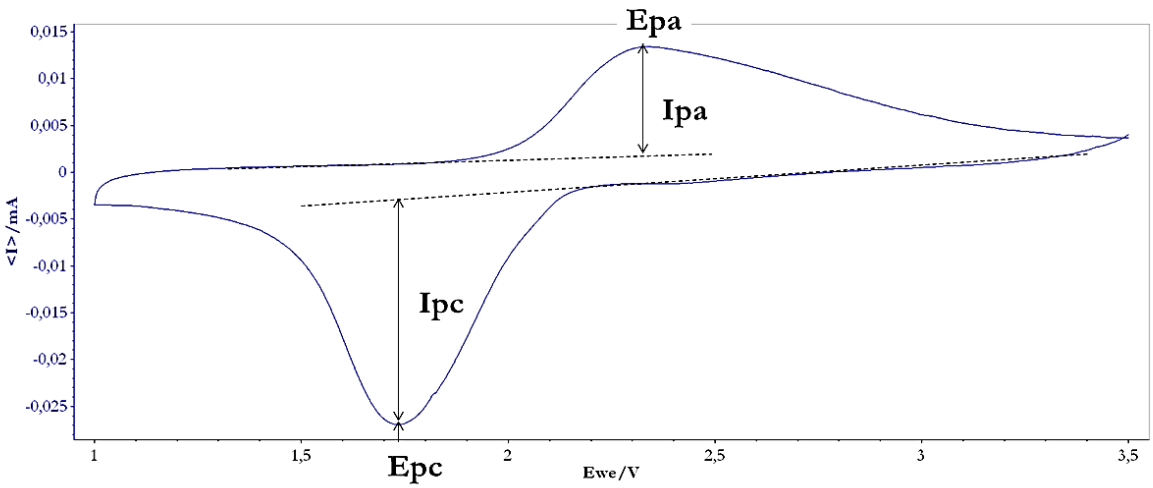

Figure 15 Cyclic Voltammogram of a Li-s battery with solid electrolyte where Ipa and Ipa are anodic and cathodic current and Epa and Epc are anodic and cathodic peak potentials

Figure 15 shows anodic and cathodic peaks with corresponding currents and potentials. It should be noted that the area under the peak for anodic processes is smaller than that of corresponding cathodic processes. This is due to the difference in concentration at the electrodes which is driving reduced species, RE (see Eq.5), further away from the electrodes into the bulk. Once RE is diffused in the bulk, they cannot be re-oxidized back fast enough in the timescale of a cyclic voltammetry experiment. [59]

3.4 Electrochemical Impendence Spectroscopy

Electrochemical impedance spectroscopy (EIS) is a technique used to study electrochemical systems by applying alternating current (AC) to a system and measuring its response. The measurement is done over a range of frequencies. The frequency responses from a variety of interfaces in a cell are revealed.

Impedance, *Z*, can be written in complex form as a sum of resistance and reactance:

$$Z = R + iX = |Z|e^{i\theta} \quad \text{Eq. 15}$$

Where *R* is the real part of impedance representing the resistance, *X* is the imaginary part representing the reactance, *i* is the imaginary unit, θ is the phase angle between the current and voltage. Graphical representation of impedance is shown in Figure 16.

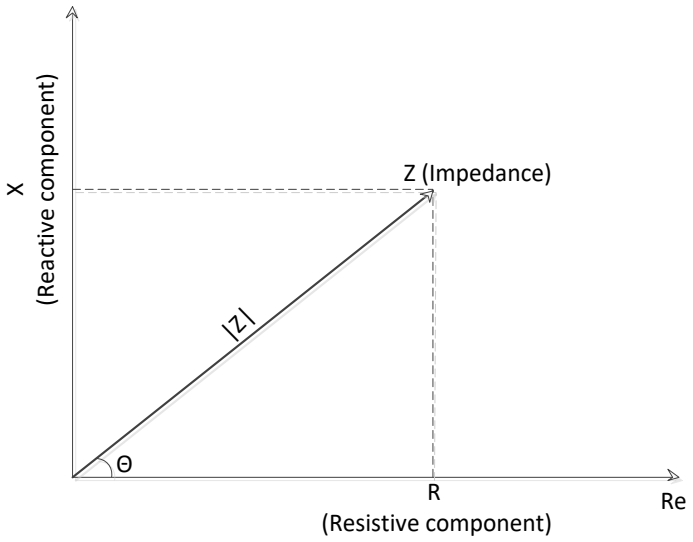

Figure 16 Reactive (X) and Resistive (R) components of impedance (Z)

$$Re(Z) = R = |Z|\cos(\theta) \quad \text{Eq. 16}$$

$$IM\ (Z) = X = |Z|\sin(\theta) \quad \text{Eq. 17}$$

It is common to plot impedance spectra as Nyquist or Bode plots. Modern potentiostats present impedance data as Nyquist diagrams and for complex processes multiple arcs are often observed which will be discussed in detail in the following sections.

3.4.1 Elements of the circuit

It is common to model and describe the results of impedance measurements in terms of electrical circuits with frequency responses similar to the measured electrochemical cell[60]. There are large numbers of possible elements but in this chapter we only focus on the ones relevant for the materials used in this work.

Table 3 Elements of the electrical circuits that were used for modelling in this work

Resistor	For resistors, phase shift (φ) is zero and impedance in this case is represented only by its real component Z'. Resistance can be found by Ohm's law: $$Z_R = \frac{U}{I}$$ For an ideal resistor the current flowing through is always proportional with the voltage across the resistor, independently of the frequency.
Capacitor	Capacitors are together with resistors passive elements of the electric circuit; however the behavior of a capacitance is very different than that of a resistance. For an ideal capacitor, DC current cannot pass through a capacitor, however in reality all capacitors have a small leak current, which we will not consider here. If we apply DC current to a capacitor, a charge will build up and the voltage across the capacitor will rise over time.[61] The relationship between charge and current can be expressed as: $$V = \frac{Q}{C}$$ If we invert the DC current, the charge will disappear over time and a charge with opposite sign will build up. This behavior gives a frequency depending impedance when alternating the current. The impedance of a capacitor can be described as: $$\boldsymbol{Z_C} = \frac{1}{j\omega C}$$ We can see that the impedance is infinite at DC current and inversely proportional to the frequency. In other words the impedance have low values at high frequencies.

Table 3 (continued) Elements of the electrical circuits that were used for modelling in this work

Inductor	Inductance is represented by a coil. Current induces electromotive force in a coil which opposes the changes in current. An ideal inductor has zero resistance (in the real world an inductor always has a small resistance). When passing a current through an inductor, a magnetic field builds up which will prevent any sudden change in current, since a magnetic field cannot be changed suddenly. This gives a behavior where current can flow through the inductor unhindered at DC current but will have impedance when alternating the current. $$\boldsymbol{Z_L} = j\omega C$$ We can see that the impedance is zero at DC and is proportional with the frequency. In other words, the values of impedance are low at low frequencies and high impedance at high frequencies.
Constant Phase Element (CPE)	CPE is an element that is used to model double-layer diffusion that can be seen as imperfect capacitor. Imperfections in the sample, such as finite distribution of material, roughness of electrodes, make CPE a non-ideal circuit element. CPE is represented by a depressed semi-circle that originates under Z' axis. Impedance of CPE can be found as: $$\boldsymbol{Z_{Q(w)}} = \frac{1}{Q_o(i\omega)^n}$$ Q_o is the capacitance while n is an exponent that is an empirical constant that equals 1 for a capacitor
Warburg Element (W)	W is a distributed element that represents semi-infinite or finite-length diffusion. The element models the diffusion of active ions to the electrode interface. Impedance of a Warburg element is found as: $$\boldsymbol{Z_{W(w)}} = \frac{A_w}{\sqrt{\omega}} + \frac{A_w}{i\sqrt{\omega}}$$ Where A_w is the Warburg coefficient which is a diffusion coefficient of ions in solids or in solution. Warburg coefficient can be found as the slope of a function given by real part of impedance R plotted against square root of frequency $1/\sqrt{\omega}$.

3.4.2 Modeling of the system: the Brick Layer Model

Interpreting results of impedance measurements of polycrystalline solids can be a difficult task. In case when contributions from various processes in a cell occur with different time constants, they are seen in different frequency ranges, however, when a number of processes occur with same or similar time constants and they cannot be resolved in an impedance spectrum.

A way to solve this problem is by modelling behavior of an electrochemical system by using equivalent circuit elements. A model that is commonly used to fit impedance spectra is the brick layer model (BLM) which model ion transport in conducive solids. BLM originates from Beekmans and Heyne's work who studied grain-boundary effects, and the so called "intergrain polarization", on impedance spectrum. The authors conclude that this "intergrain polarization" is the reason behind why polycrystalline materials always have smaller conductivities than single crystalline grains[62]. Their work was developed further by Van Dijk and Burggraaf who included geometrical considerations (parallel and perpendicular boundaries) in the model.[63]

According to Brick Layer Model, the contributions to the EIS spectra come from the following interfaces:

- Electrodes:
- Grain interior (bulk):
- Parallel grain boundaries:
- Perpendicular grain boundaries:

Figure 17 shows a representation of Brick Layer Model showing two types of boundaries: grain boundaries parallel with the current (thick black), or perpendicular to current flow (orange):

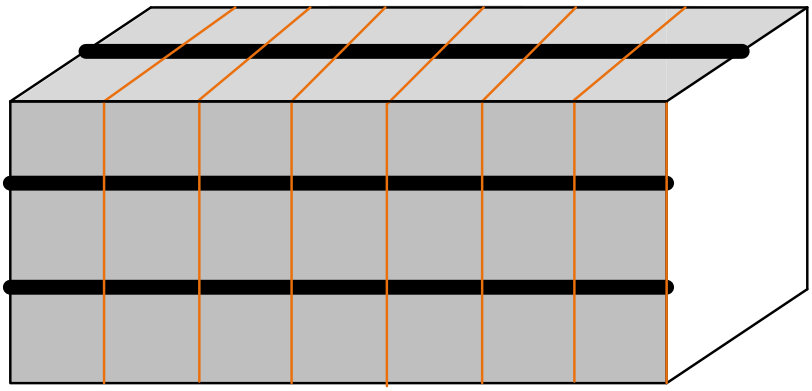

Figure 17 Representation of Brick Layer Model showing bulk (gray) and two types of grain boundaries: parallel grain boundaries (black) and perpendicular grain boundaries (orange)

Figure 18 shows an equivalent circuit for BLM shown in Figure 17. R1 and Q1 represent resistance and constant phase element (CPE) of parallel grain boundaries, R3 and Q3 represent grain (bulk) boundary, R2 and Q2 are perpendicular grain boundaries and Q_{ec} represents electrodes. The two components are in series with perpendicular grain boundaries and electrodes' response.

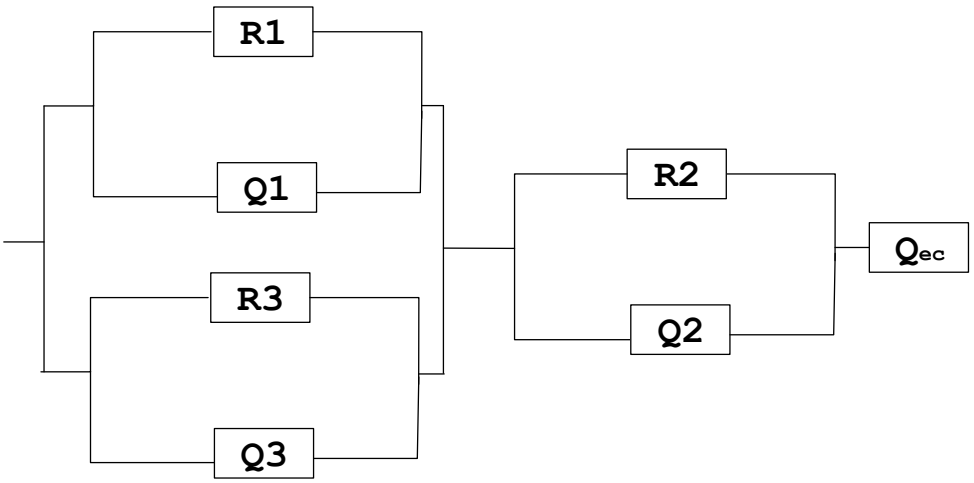

Figure 18 Equivalent circuit for polycrystalline materials representing Brick Layer Model.

The equivalent circuit from Figure 18 can be simplified by making a combination of resistors R1 and R3 where the inverse of this single resistor (R_{1+3}) will be equal to:

$$\frac{1}{R1} + \frac{1}{R3} \quad \text{Eq. 18}$$

The pseudo-capacitance of component Q_{1+3} can be found as a sum of pseudo-capacitances of single component 1 (Y_1) and 3 (Y_3):

$$Y_1 + Y_3 \quad \text{Eq. 19}$$

The resulting equivalent circuit is shown in Figure 19.

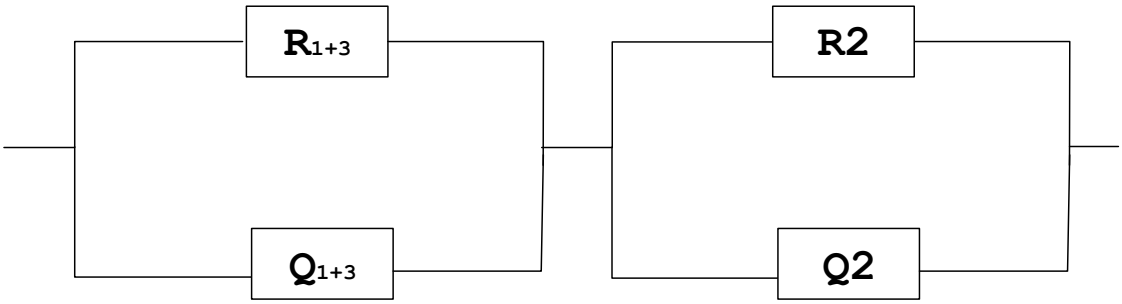

Figure 19 A simplification of equivalent circuit for Brick Layer Model where contributions from bulk and parallel grain are considered as a single element

Assuming that grain boundaries, parallel and perpendicular, are Effective conductivity of both components can be written as:

$$\frac{1}{\sigma_e} = \frac{1}{\sigma_{1+3}} + \frac{1}{\sigma_2} = \frac{1}{\sigma_{1+3}} + \frac{1}{\sigma_{1+3}} \quad \text{Eq. 20}$$

Where G is the diameter or length of grains, g is the thickness of grain boundary

The ration between conductivities for bulk and grain boundary can be written as:

$$\frac{\sigma_{1+3}}{\sigma_2} = \frac{R_2}{R_{1+3}} = \frac{g}{G} + \frac{R_2}{R_{1+3}} + \frac{g}{G} \quad \text{Eq. 21}$$

To separate the contributions in impedance spectrum, one needs to consider three scenarios:[64]

In case where conductivity of bulk is higher than the conductivity of grain, two arcs can be distinguished in the impedance spectrum of a given material:

$$\sigma_{\text{bulk}} > \sigma_{\text{g}} \quad \text{Eq.22}$$

For case where grain boundary conductivity is higher than that of the bulk, two arcs will not be distinguishable from one another:

$$\sigma_g > \sigma_{bulk} \quad \text{Eq.23}$$

For cases where bulk conductivity is similar to grain conductivity, the two arcs cannot be distinguished:

$$\sigma_g \sim \sigma_{bulk} \quad \text{Eq.24}$$

To summarize, impedance spectra of polycrystalline solids will typically show a Nyquist plot with one or with two arcs. In the latter case, bulk conductivity of the sample is higher than the conductivity of the grain boundaries. In case of single arcs, the contributions from grain interior and grain boundary cannot be separated using impedance spectroscopy.

3.5 Thermal Gravimetric Analysis (TGA)

Thermal gravimetric Analysis (TGA) is a thermal analysis method where the mass of a sample is being measured as a function of time during heating or cooling.[65] The mass of a sample is measured on a balance in a controlled atmosphere while being subjected to controlled temperature program.

The analysis shows weight loss or gain of the sample due to chemical (e.g. oxidation and reduction) or physical phenomena (e.g. sublimation). Typical applications of TGA are among other determination of thermal stability, water or carbon content and reactivity with gases. [66]

3.6 -state Nuclear Magnetic Resonance (SS-NMR)

3.6.1 Introduction to NMR experiments

Nuclear magnetic resonance (NMR) is a technique commonly used to study structure of molecules by exciting the nuclei and studying the emitted signals [67]. An NMR experiment consists of 2 steps as shown Figure 20:

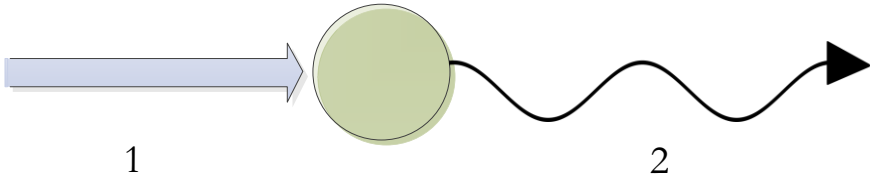

Figure 20 Pricipal of a NMR experiment. The excitation pulse is applied to a sample (1) and the frequency of the signal emitted by the the sample is measured (2)

1. Static magnetic field is applied to a sample and the nuclei are excited with a radio pulse.
2. The frequency of the signal emitted by the sample is measured by a spectrometer.

The signals are received by the spectrometer as Free Induction Decay (FID) and before they can be analyzed, need to be Fourier transformed from time domain to frequency spectrum by the software. [67]

The NMR properties of nuclei depend on its spin (I). Three cases are possible[68]:

- I = 0, e.g. ^{12}C, ^{16}O: No NMR shifts are observed and the only effect on the nuclei will be the isotope shift.
- I = ½, e.g. $^{1}H_{1}$ (1/2), $^{7}Li_{3}$ (3/2), $^{11}B_{5}$ (3/2): shifts are observed with sharp lines and observed J coupling. J-coupling, also referred to as indirect dipole-dipole coupling, is mediated through hyperfine interactions between the spin of a nucleus and spins of intervening electrons.[69] As the magnitude of J decreases rapidly with increasing number of intervening bonds, J-couplings provide information about bond distances and connectivity of atoms in molecules.
- I > ½ (quadrupolar nuclei), e.g. $^{2}H_{1}$, $^{10}B_{5}$, quadrupolar nuclei might have observable spectra, however there are often issues related to them, for example they might give broad line and no high resolution spectra can be acquired.

NMR sensitivity of commonly used nuclei in NMR are summarized in Figure 21:

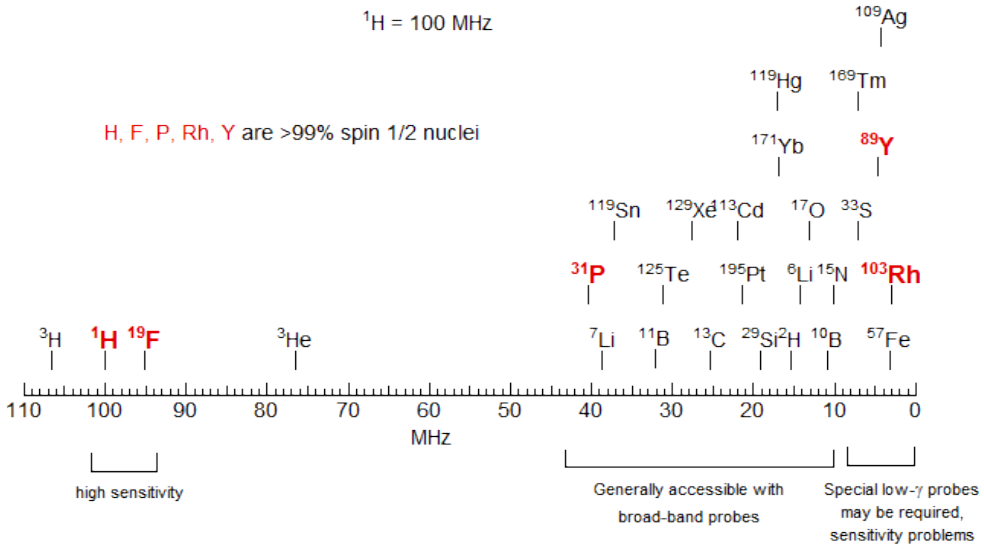

Figure 21 NMR sensitivity of commonly used nuclei

Reprinted from Reich, 2018 [68]

As it can be seen from Figure 21, H and F are highly sensitive nuclei and Li and B are accessible with broad band probes which makes the technique well suited for analysis of $LiBH_4$-SiO_2 and $LiBH_4$-$LiBF_4$ samples even with low content of $LiBH_4$.

3.6.2 Classical Vector Model

In Classic Vector Model, the formation of net magnetization arising from all nuclei is studied in a sample.[70] When no magnetic field is applied to the sample, all nuclear magnetic moments have random orientations and therefore net magnetization is equal to zero as single magnetic fields cancel out one another. When static magnetic field (B_0) is applied to the sample, magnetic moments will align with the direction of the magnetic field as shown in Figure 22. Bulk magnetization, M, is defined as volume density of all nuclear magnetic moments that are aligned and is proportional to magnetic field. The intensity of M shows the ratio between the two spin populations aligned with or against the field.

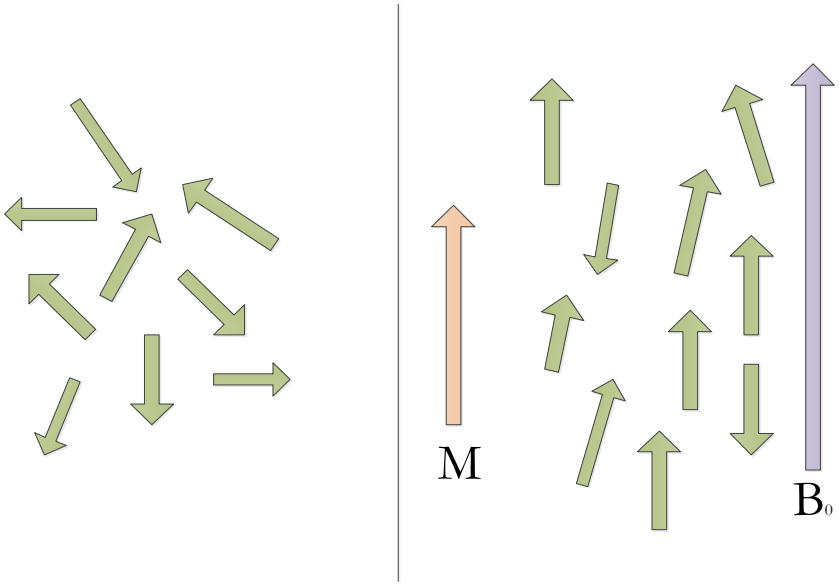

Figure 22 Formation of net magetization in a sample.
When no external field is applied (left) nuclear magnetic vectors have random orientations

When static magnetic field B_0 is applied along the longitudinal axis, an angle between bulk magnetization, M, and B_0 will be observed as M will be moving around B_0 with angular frequency ω_0 as shown in Figure 23.

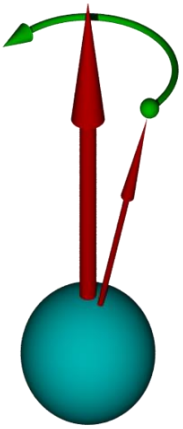

Figure 23 Angular momentum of an object in a magnetic field.
Spin angular momentum is shown as a thin arrow and external magnetic field is a thicker arrow
(graphics by Yamavu/ Wikimedia Commons /CC-BY 3.0)

The frequency ω_0 is known as Larmor frequency and is expressed as:

$$\omega_0 = \gamma B_0 \quad \text{Eq. 25}$$

where γ is the gyromagnetic ratio which is a ratio of a particle's magnetic momentum and angular momentum and B_0 is the strength of the magnetic field. As gyromagnetic ration can be positive or negative, it is the sign that determines the precession (clockwise or anticlockwise).

3.6.3 Magic-Angle Spinning (MAS)

For liquid samples, effects of anisotropy and dipolar coupling are rarely affecting the NMR spectra because of the rapid motion of molecules in solution. For samples in powder form in solid-state NMR, the obtained spectra are broad as random orientations in crystallites give different spectral frequensies[71]. For that reason, it is important to use NMR techniques that allow to obtain high resolution spectra like Magic-Angle Spinning (MAS). MAS measurements are used in a majority of solid-state NMR experiments. It helps to decrease the effects of heteronuclear dipolar coupling and chemical shift anisotropy. The dipolar coupling is the interaction between two atoms' dipole moment. The magnitude of dipolar coupling depends on spin species, distance between the nuclei and orientation of the internuclear vector as shown in Figure 24.

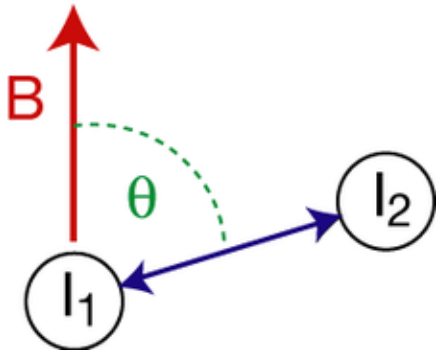

Figure 24 Dipolar coupling vector indicated as blue arrow.
Angle θ is the angle between applied magnetic field B and internuclear vector
(graphics by Ksei/ Wikimedia Commons /CC-BY 3.0)

Maximum dipolar coupling, d, is expressed as [72]:

$$d = \frac{k}{R^3}\left(\cos^2\theta - \frac{1}{3}\right) \quad \text{Eq. 26}$$

where R is the distance between two nuclei, θ is the angle between magnetic field and internuclear vector. The term K is determined by the physical constants:

$$k = -\frac{3}{8\,\pi^2}\gamma_1\gamma_2\mu_0\frac{h}{2\pi} \quad \text{Eq. 27}$$

Where γ_1 and γ_2 are the gyromagnetic ratios of the spin 1 and 2, h is the Planck's constant and μ_0 is the permeability of vacuum.

In order to minimize the contribution from dipolar coupling, it is possible to choose the angle θ such as it would satisfy following condition:

$$(3\cos^2\theta_m - 1) = 0 \quad \text{Eq. 28}$$

Angle that satisfies this condition is $\theta_m = 54{,}7°$ and at this θ the term d is equal to zero and the contribution from dipolar coupling is zero.

In practice, the sample is rotated along an axis inclined at an the angle θ_m with respect to the applied magnetic field, B_0 (Figure 25).

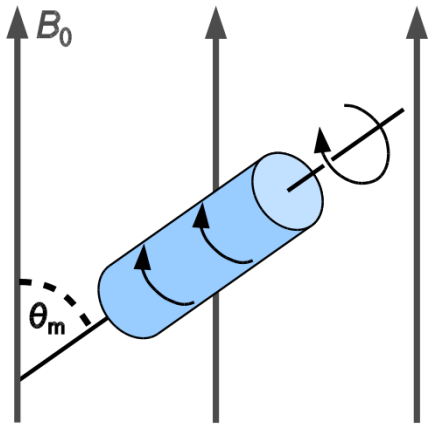

Figure 25. The principle of Magic Angle Spinning
(graphics by Dtrx/ Wikimedia Commons /CC-BY 3.0)

Magic-angle spinning averages anisotropy in the sample and can be performed at different spinning speeds depending on the size of the rotor used. It is possible to average anisotropic interactions in a sample either completely or partially depending on MAS frequency. [73] In case of partial averaging, spinning sidebands appear in the spectrum corresponding to Fourier components of spinning frequency and with intensities that depend on primary component's interaction tensor and its spinning frequency. In case of complete averaging of anisotropic interactions, narrow lines will appear, however the narrowing is achieved at loss of orientation dependence which could give information of structure and dynamics in the sample.[73]

3.6.4 Decoupling Experiments

Decoupling experiments are used when weak spins are to be observed together with some abundant spin (e.g. ^{1}H) giving broadening of spectral lines due to heteronuclear coupling.[71] To remove effects of heteronuclear dipolar coupling, high-power decoupling is used. Decoupling experiments allow eliminating bands coming from different nuclei. The technique is based on using continuous high power irradiation (up to 1 kilowatt) with the frequency of proton resonance. Figure 27 shows a typical sequence for a high-power decoupling experiment for some given nucleus, X.

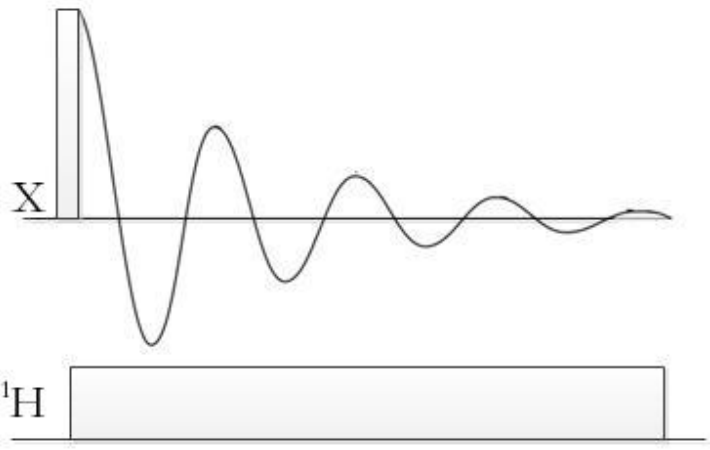

Figure 26. Typical pulse sequence for a high-power decoupling experiment for a nucleus X.

The proton irradiation is applied continuously, the pulse sequence of the measured nuclei is applied and the FID is measured which helps to remove lines coming from nearby protons in the sample.

3.6.5 Exchange Spectroscopy

In exchange spectroscopy (EXSY) experiments are used to probe molecular motions of correlation times of milliseconds or slower[74]. An initial pulse at 90° to the main external magnetic field creates transverse magnetization. The magnetization is evolving during the time period t_1 and a characteristic frequency evolves from interactions of nuclear spins (Figure 27).

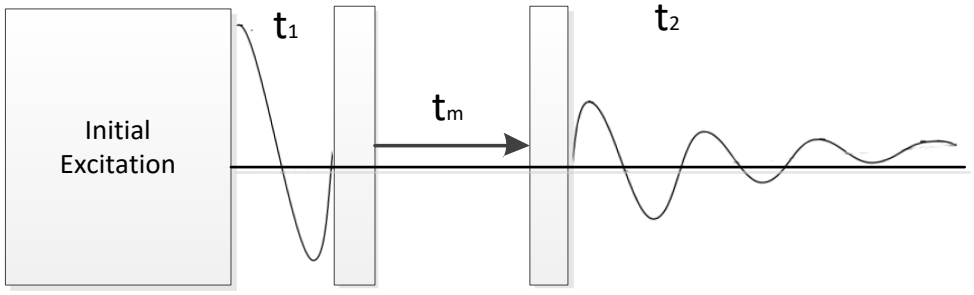

Figure 27 Typical pulse sequence of an exchange measurement

Exchange experiments are typically used to determine exchange rate between 2 or more nuclei or between anions exchange in different environments.

2D-Exchange measurements carried out with different mixing time can be used to make estimations of rate constant of a two-site exchange process which can be found as:[75]

$$\frac{a_{cross}}{a_{diagonal}} = \tanh(kt_m) \qquad \text{Eq.29}$$

Where a cross and a diagonal are the integrated cross peak and diagonal-peak intensity of EXSY spectrum and t_m is mixing time.

3.6.6 Spin-lattice Relaxation Rate

In spin-lattice relaxation rate measurements, the characteristic time needed for attainment of thermal equilibrium of spins or for the excess of energy to be given to a lattice as a results of redistribution of spins when magnetic field is applied to a sample, is measured. Longitudinal (spin-lattice) relaxation time, T_1, is defined as decay constant of recovery of z-component of magnetization vector, compared to its equilibrium value, M_0.

$$M_z(t) = M_0(1 - e^{\frac{-t}{T1}}) \qquad \text{Eq.30}$$

When spin-lattice relaxation times are measured over a range of temperatures, it allows to calculate average jump rates of ions, τ^{-1}, using the equation:[76]

$$\frac{1}{T_1} = \frac{2\pi^2}{25} \cdot C_q^2 \cdot \left(1 + \frac{n_Q^2}{3}\right) \cdot \left[\frac{\tau_c}{1 + \omega_c {\tau_c}^2} + \frac{\tau_c}{1 + 4\,\omega_c {\tau_c}^2}\right] \quad \text{Eq. 31}$$

Where C_q is the quadrupole coupling constant, n_Q is the asymmetry parameter, ω is the Larmor frequency, $1/T_1$ is the spin-lattice relaxation times, ${\tau^{-1}}_c$ is the motional correlation rates. ${\tau^{-1}}_c$ with a factor of the order of unity equal to one (c = 1) is identified as average jump rates of ions, τ^{-1}. [75]

Knowing the jump rates of ions, it is possible to calculate the activation energies using the main residence time of mobile spins, τ_X, using the Arrhenius law:[77]

$$\tau_x = \tau_o \, exp\left(\frac{E_a}{R_g T}\right) \quad \text{Eq.32}$$

Where τ_o is mean residence time at infinite temperature or inverse of the frequency factor, E_a is the activation energy, R_g is the gas constant and T is the temperature.

If average jump rates are known, it is possible to calculate the ion diffusion coefficient, D^T, using the Einstein-Smoluchowski equation:

$$D^T = f\frac{l^2}{6\tau} \quad \text{Eq. 33}$$

Where f is the correlation factor for ion movements (for completely uncorrelated ion movements f=1 is used), l is the shortest jump distance for ion and τ^{-1} is the average jump rates.

Another way to calculate diffusion coefficient D^T is by using the Nerst equation:

$$D^T = H_R \frac{k_b T}{N{q^2}_c} \cdot \sigma_{dc} \quad \text{Eq. 34}$$

Where H_R is Haven ratio that is (almost but not exactly) equivalent to the correlation factor for ion movements, f,[37] k_b is the Boltzman constant.

Mean residence time of mobile spins, τ_X, can be calculated with Arrhenius law as[77]:

$$\tau_x = \tau_o \, exp\left(\frac{E_a}{R_g T}\right) \quad \text{Eq. 35}$$

Where τ_o is mean residence time of ions inverse of frequency factor or the mean residence time, E_a is the activation energy, R_g is the gas constant and T is temperature

3.6.7 Raman spectroscopy

Raman spectroscopy is a technique aimed to study chemical fingerprint of a molecule by studying low the frequency modes, vibrations, rotations and other in molecules.[78] Raman spectroscopy is used in various laboratories due to possibility to make rapid analyses of solids, liquids and gases. No or little preparation is required for solid samples while liquids can be analyzed in glass ware or through plastics. Even samples dissolved in water can be analyzed with Raman which is a limitation of other spectroscopic techniques, such as IR [79]

Raman effect occurs only when a change in polarizability happens during normal vibration, while for infrared spectroscopy, a change in permanent dipole moment happens during vibration[79]. Schrödinger equation for particle in a box shows that a limited number of energy levels are allowed:

.

$$\mathrm{E_\nu} = \left(\nu + \frac{1}{2}\right) \bullet \mathrm{h\nu_\nu} \; (\nu = 0, 1, 2, \ldots) \quad \text{Eq. 36}$$

Where ν is the vibrational quantumnumber, h is the Planck's constant, ν_v is the molecular vibrational frequency.

From equation 3 it is clear that Raman transitions occur in steps equal to ± hν. [79]

If the difference between energy levels in equation 3 is 0, the transition is referred to as Rayleigh scattering as shown as blue and red arrows in Figure 28 , if the difference between levels is not zero, three cases are possible:

- **Infrared absorption:** is a transition from ground state v=0 to the first excited state, v=1;
- **Stokes Raman scattering:** is a transition from ground state to virtual energy state, i.e. photon lost energy to a molecule
- **Anti-stokes Raman scattering:** is a transition from first excited state to ground state, i.e. photon gained energy from a molecule

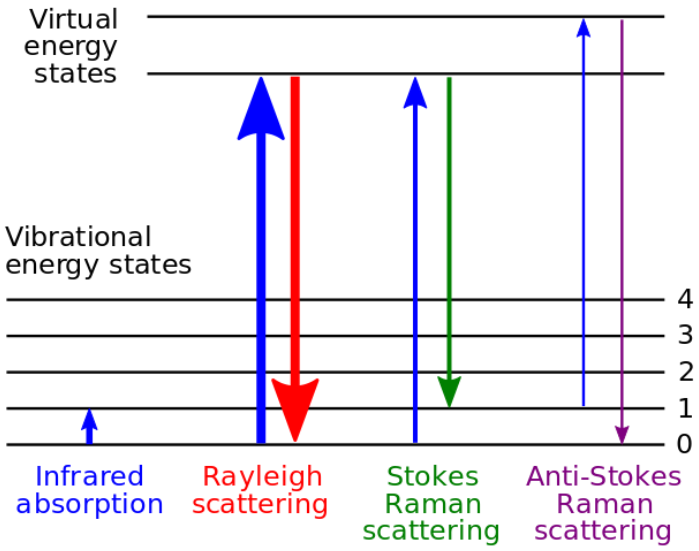

Figure 28 Energy levels difference Principle of Raman scattering
(graphics by Moxfyre/ Wikimedia Commons /CC-BY 3.0)

For a case where molecules are excited from v = 0 to v = 1, the symmetry of wave function in the ground state is equal to that of the molecules. As a consequence, for a vibrational transition to be allowed, it is required that the symmetry of the wave function in the excited state should be the same as the symmetry of the transition moment operator. While for infrared spectroscopy, this transition moment operator must transform as x or y or z and the excided state wave function should transform as at least one of the vectors. For Raman spectroscopy, the transition moment operator must transform as one of the second-order terms. For example, consider adamantine molecule with point group T_d [80]

Table 4 Character table for Td group (adopted from Salthouse, et al[80])

	E	8 C_3	3 C_2	6 S_4	6 σ_d		
A_1	1	1	1	1	1		$x^2 + y^2 + z^2$
A_2	1	1	1	-1	-1		
E	2	-1	2	0	0		$(2z^2 - x^2 - y^2, x^2 - y^2)$
T_1	3	0	-1	1	-1	(R_x, R_y, R_z)	
T_2	3	0	-1	-1	1	(x, y, z)	(xy, xz, yz)

For adamantine molecules, four vibrations are Raman active and one is infrared active.

Raman shifts are often reported as wavenumbers in inverse centimeters:

$$\omega = \frac{\nu_m}{c} - \frac{\nu_0}{c} \qquad \text{Eq. 37}$$

Where ν_m is the frequency of scattered light, ν_o is the incident radiation and c is the speed of light.

3.6.8 Scanning Electron Microscopy

Scanning Electron Microscopy (SEM) is a type of microscopy based on using a focused electron beam. The technique is commonly used in research when information is needed in the surface or in the near-surface regions of bulk specimens.[81] Essential components of a SEM microscope include following parts: electron optical column that is shown in Figure 29, vacuum system, infrastructure requirements (e.g. cooling, power supply) and a computer with software for data analysis.[82]

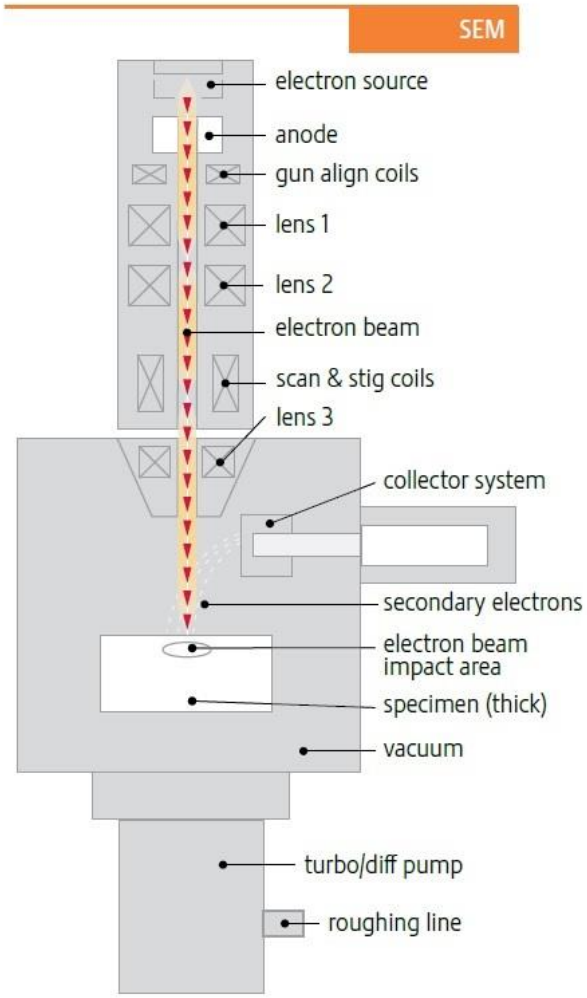

Figure 29 Main components of SEM Microscope (Reprinted from ThermoFisher Scientific, 2010[81])

The optical column in SEM is much shorter that the ones used in transmission electron microscopes (TEM) as only lenses above the specimen are used in SEM while TEM uses both lenses above and below the specimen.[81] At the same time, specimen chamber in SEM is larger than in TEM as there are no restrictions on the sample size in SEM.

The electron source at the top of the column (e.g. hairpin tungsten or lanthanum hexaboride) generates an electron beam by accelerating electrons to 0,1-30 keV. As the diameter of the beam emitted by the electron gun is too big to produce image with high resolution, a set of lenses is used in the optical column to generate a beam with a smaller diameter that can form a required spot on a specimen.[83]

The beam scans the surface of the specimen in a raster pattern and intensities of various types of signals that are caused by beam electrons interacting with the specimens are recorded. Various signals that are produced in SEM are illustrated in Figure 30 (reprinted from Zhou, et al).[83]

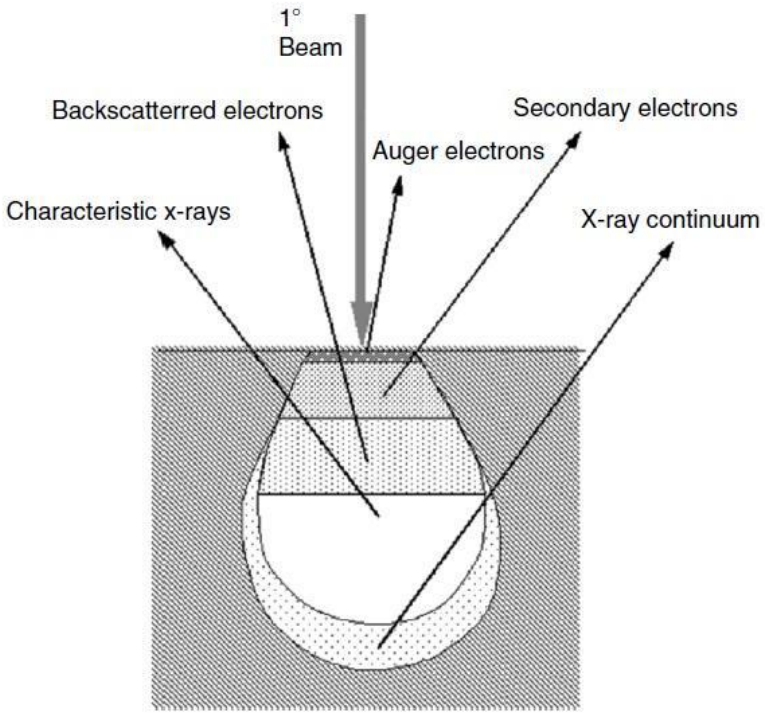

Figure 30 Types of signals analyzed in SEM (reprinted from Zhou, et al [83])

- **Secondary Electrons (SE):** is the most widely used signal in SEM. The signal is produced when the primary beam hits the surface of the sample which leads to ionization of atoms in the specimen and emission of loosely bound electrons that are referred to as secondary electrons. Since SE have average energies of 3 to 5 eV, which is low, they are emitted within a region of few nanometers on the specimens' surface which gives topographic information (texture and roughness of the surface) with high resolution.[83]

- **Back-Scattered Electrons (BSE):** are electrons that are scattered elastically at the angle >90° and have energy greater than 50 eV.[83] BSE gives both topographic and compositional information of the surface which allows phase discrimination in samples with multiple phases.[82]

- **Characteristic X-Rays:** the signal is produced by inelastic collisions of electron beam andelectrons in the shells of the atoms at the specimen surface. When excited electrons fall back to lower energy states, an X-ray photon is emitted to reestablish right charge balance. Characteristic X-rays are used mainly for chemical analysis in Energy-dispersive X-ray spectroscopy (EDS) which will be discussed in the next section.[82]

- **Auger Electrons:** are the electrons emitted when ion beam ionizes the atom causing outer shell electrons to fill inner shell vacancies. Auger electrons have characteristic energies and give chemical information about the surface .[83]

- **Transmitted Electrons:** allows examining the internal structure of thin specimens (thinner than 1μ). It is used in scanning transmission electron microscopy (STEM). The major advantage of STEM compared to SEM is improved spatial resolution as electron scattering in the bulk is eliminated by using focused beam. [82]

- **Cathodolumineschence (CL):** are the phonons of various wavelengths; Infrared (IR), Visual (VIS) and Ultraviolet (UV) emitted by some materials, for example fluorescent dyes and zinc sulfide.[83]

SEM is one of the most widely used techniques for analysis of solid materials, both in science and in industry. The majority of SEM machines today are user-friendly and easy to operate and for many applications, limited sample preparation is required and spectra acquisition takes short time. The limitations of SEM are the limited size of the specimen and that it has to be stable in vacuum, however low vacuum machines also exist. [82]

3.6.9 Energy-dispersive X-ray spectroscopy

Energy-dispersive X-ray spectroscopy (EDS) is a technique that allows non-destructive chemical characterization of solids. EDS microscopes are normally integrated with SEM or electron probe micro-analyzers.[84]

An EDS system consists of an x-ray detector that is mounted on the sample chamber of SEM instrument, a nitrogen tank for cooling and a software to record and analyze obtained spectra. An EDS detector that is used to separate x-ray signals of various elements contains typically of Si (Li) crystals absorbing energy of x-rays and thus yielding free electrons in the detector crystals and causing electrical charge bias. These electrical voltages correspond to characteristic x-rays of the elements.[84]

The advantages of using EDS are that it is possible to rapidly (within a few seconds) acquire a full elemental spectrum of a sample and to get information of unknown phases, furthermore EDS gives semi-quantitative information by peak-height ratio. One of the disadvantages, is that EDS peaks may overlap because of emissions of different energy shells with same energies for example k-alpha in Mn and k-beta in Cr. [84] Another disadvantage is that EDS cannot analyze light elements (H, He) and many instruments cannot analyze the elements before sodium. Finally, due to use of solid state X-ray detectors, EDS has a lower sensitivity and lower energy resolution compared to electron probe micro-analyzers or wavelength dispersive X-ray spectroscopy[82].

3.6.10 X-Ray diffraction

X-ray Diffraction (XRD) is a non-destructive technique used for the characterization of crystalline materials. XRD makes possible phase identification in crystalline samples and measuring their unit cell dimensions. The technique is based on using monochromatic X-ray beam interfering with a sample. Consider two beams of x-rays that hit a crystal lattice as shown in Figure 31:

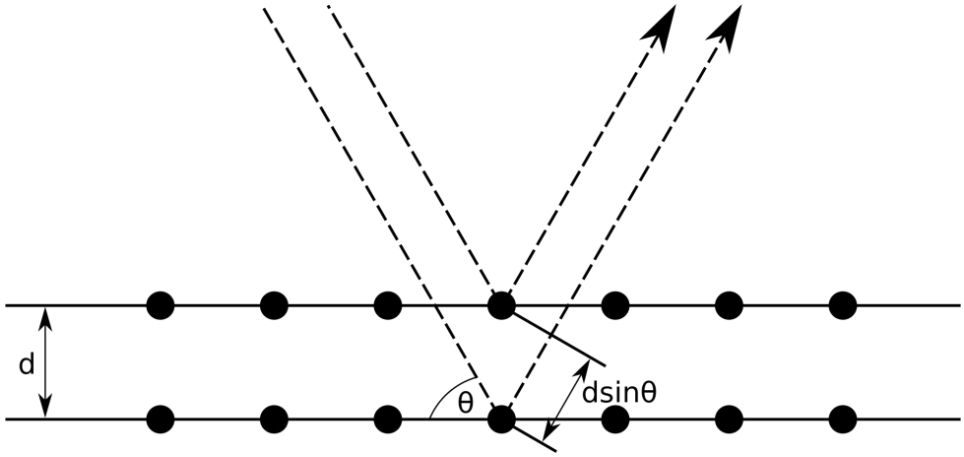

Figure 31 The principle of Braggs Law
(graphics by Furiouslettuce/ Wikimedia Commons /CC-BY 2.0)

The two beams are diffracted by the electron clouds of atoms sitting on two different plans of the crystal lattice. When the Braggs Law is obeyed:

$$\eta\lambda = 2d \cdot sin\Theta \qquad \text{Eq. 38}$$

Constructive interferences are obtained giving diffraction peaks in the diffraction pattern. When the Bragg law is not fulfilled, destructive interferences occur and no intensities are recorder by the detector except for the background.

Interactions between X-Ray beam and the atoms depends on their atomic numbers – atoms with higher atomic numbers will produce stronger signals due to higher electron density, while atoms with lower numbers produce weak signals. Apart from the size of the atoms, signal intensity is also influenced by statistical distribution of planes – if a set of planes is predominant, a higher intensity of the peak is expected.

3.6.11 Synchrotron Measurements

3.6.11.1 Microtomography

X-Ray microtomography is a technique that allows studying internal structure of a specimen by making a reconstruction of transverse sections of a sample irradiated by a monochromatic X-Ray beam. X-Ray Microtomography is a combination of X-Ray imaging and computed tomography (CT).

In tomography, a number of images are taken in different sections. Consider a case, where the detector and the intensity at a transverse section *i* can be written as: [85]

$$i_{ik} = \left(\frac{I_0}{I_{ik}}\right) = \sum_{j=1}^{N} \mu_{ir} r \quad \text{Eq. 39}$$

Where I is the intensity of the incoming beam, I_{ik} is the intensity, μ_{ir} is the absorption coefficient and r is the dimension of a single pixel.

3.6.11.2 X-Ray Absorption Spectroscopy (XAS)

X-Ray absorption spectroscopy (XAS) uses the absorption coefficient of a given element as a function of energy above its absorption edge to give information about the atomic energy.[86] XAS measurements are performed at synchrotron radiation sources where the X-ray beams are intense and tunable.[87] A XAS spectrum consists of 2 major regions as shown in Figure 32.

- X-ray absorption near-edge structure (XANES).
- Extended X-ray absorption fine structure (EXAFS)

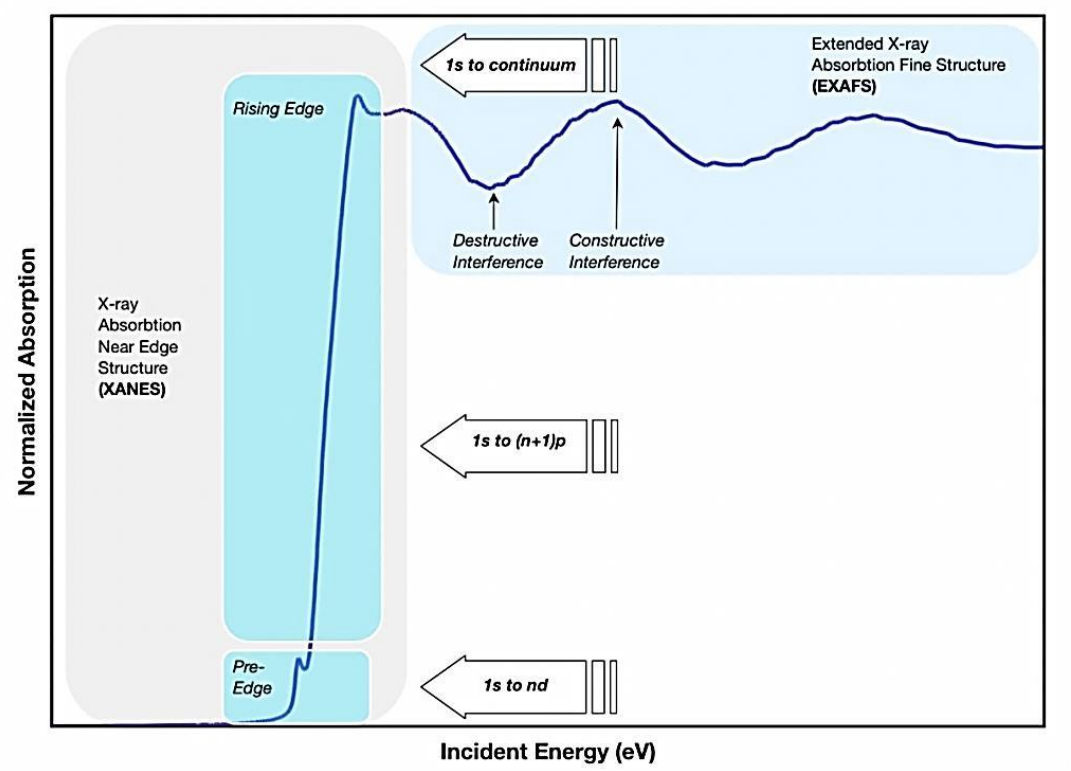

Figure 32 The areas of XAS spectrum: XANES shows in the cyan rectangles, EXAFES shown as a light bue rectangle (graphics by Munzarin/ Wikimedia Commons /CC-BY 2.0)

The difference between the two regions is that XANES is the structure close to the absorption edge, while the structure starting after 5 eV is referred to as EXAFES. [88]

XANES gives information such as valence state, bond angles and energy bandwidths. The location of an absorption edge shows the active charge of the atom. If any resolvable features are present, the final states' occupancy can be found based on location and intensity. It is also possible to study anisotropy in the final states for single crystals due to polarized nature of synchrotron radiation.[89]

In XANES measurements, the absorption process comes from exciting the inner level electrons to higher energy level with incident photons. The final states are determined by selection rules for a given ground state and symmetry.

There are several ways to collect XANES data:

- **Transmission mode (Fluorescence mode):** X-Ray are detected
- **Electron yield count mode:** Secondary electrons are detected

EXAFES is the effect caused by interaction between outgoing photoelectrons that are ejected from the inner shells of the atom and backscattered electrons from atoms nearby. The technique is useful for determination of distances between atoms and also lattice dynamics.[89]

There are several way in which one can collect EXAFES data:

- **Transmission mode:** is the most common mode in EXAFES for powder samples pressed into pellets, thin single crystals or foil;
- **Fluorescence:** Fluorescence (photons emitted by the sample) is measured by a Germanium detector. This mode is typically used for cases of dilute or self-absorbing samples;
- **Energy Dispersive:** The method performs a scan over the entire energy range to obtain an EXAFS spectrum.

Chapter 4

Experimental: Materials Preparation and Battery Setup

4.1 Preparation of $LiBH_4$-SiO_2 electrolyte

$LiBH_4$ powder (Alfa Aesar, 95% purity) and SiO_2 aerogel (Alfa Aesar, Silica gel 60, 400-600 mesh) were mixed in various ratios (10/90, 20/80, 30/70, 40/60, 50/50 wt%). The SiO_2 was dried for 12 hours at 393 K in a vacuum oven (Buchi, Switzerland) prior to mixing to remove the surface water. A Fritsch purverisette P6, planetary mill, with 5 tungsten carbide balls placed in a stainless-steel (80ml) container was used for mixing at, at a rotation speed of 300 rpm for a duration of 5 hours. The vials were rotated for 5 min. followed by 5 min. dwell to limit the temperature increase of the vial. 5 tungtsen carbide ball (10 mm) were used with typically 1 g of sample giving a ball to powder ration of BPR = 125:1. All the samples handling were performed in an argon glovebox.

4.2 Preparation of $LiBH_4$-$LiBF_4$ electrolytes

$LiBH_4$ –$LiBF_4$ composites were prepared by Peter Ngene from Utrecht University by mixing $LiBH_4$ and $LiBF_4$ in various ratios (5 to 35 wt% of LiBF4 using steps of 5 wt%). $LiBH_4$ and $LiBF_4$ were mixed in a mortar after which the powder was packed in a steel vessel and inserted in an autoclave. Packing was performed in argon atmosphere. The autoclave was then pressurized with 50 bar of hydrogen and heated to 200-250 ˚C at rate 5◦ C/min for and left at maximum for 30 minutes.

4.3 Preparation of the C+S and Li electrodes

The C+S positive electrodes were chosen due to their high specific capacity of 1675 $mAhg^{-1}$ based on sulfur. The cathodes were prepared by a procedure describe by Das et al[90] where Ketjen Black EC 600 JD (surface area 1400 m^2g^{-1}, pore volume of 4.80-5.10 m^3g^{-1}, Shanghai Tengmin Industry) was mixed with Maxsorb activated carbon MCS 30 (surface area 3000 m^2g^{-1}) in ration 1:1 by weight. Sulphur (Sigma Aldrich, 99.9% purity) was mixed with carbon in weight ration 45:55 for 30 min (400 rpm) in Fritsch Pulverisette P7. After mixing, the resulting powder was heated at 155◦ C durring 6 hours in sealed steel vessels (under argon atmosphere) at a rate of 0.2◦ C/ min. When the mixture cooled down to room temperature, 10-15% polyvinylidene fluoride (PVDF) was added followed by N-methylpyrrolidinone (NMP). The resulting slurry was stirred overnight, casted on aluminum foil and dried for 24 hours at room temperature. Once dried, the electrodes were punched into disks of 10 mm in diameter.

For Li electrodes, lithium foil (99.9 %, Sigma Aldrich, thickness of 40 μm) was cut in disks of 10 mm in diameter for the electrochemical measurements.

4.4 Preparation of Li-S battery with $LiBH_4$-SiO_2 electrolyte

All-solid-state LiS cells with $LiBH_4$-SiO_2 electrolyte were made in in-house made cells with the design shown in Figure 33. The battery casing is made of a cylindrical die in polyethertherkethone (PEEK) with inner diameter of 10 mm. PEEK was chosen due to its high tensile strength (90-100MPa) and high melting point (343°C). [91]

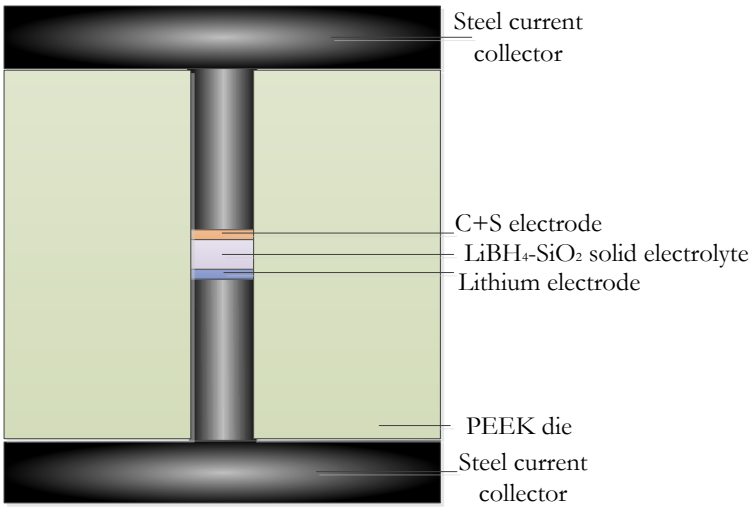

Figure 33 The deisgn of the inhouse LiS cell

The cell assembly was done in a glovebox in argon atmosphere. The assembly was performed in layers starting from Li anodes punched as 10 mm disks, thereafter about 50 mg of solid state electrolyte was added to the cell and with C+S disks as the cathode. The assembled cells were pressed to 2 ton cm^{-2} to achieve good contact between the constituent elements.

4.5 Cell Measurements

4.5.1 Electrochemical Measurements

After assembly, the batteries were connected to a VMP3 potentiostat (Bio-Logic SAS, France) and put in a heating chamber for 1 hour at 55°C. During this period, Open Circuit Voltage (OCV) was measured followed by electrochemical impedance spectroscopy (EIS) which was also performed after each discharge/charge cycle. Impedance measurements were performed in the frequency range from 1Hz to 1 MHz.

Charge and discharge of Li-S batteries were performed using Galvanostatic cycling with potential limitation (GCPL) set with cutoff voltages of 1 V (discharge) and 3.5 V (charge). The current was set to 5 μA which is equivalent to C-rate of 0.03 C calculated from the theoretical specific capacity of 1675 $mAhg^{-1}$ based on sulfur. Cyclic Voltammetry (CV) measurements were performed in voltage range from 1 to 3.5 V with sweeping rates of 0.1 mVs^{-1}

4.5.2 Three-electrode setup

For measurements in a three electrode setup mode, a modified cell was used as shown in Figure 34.

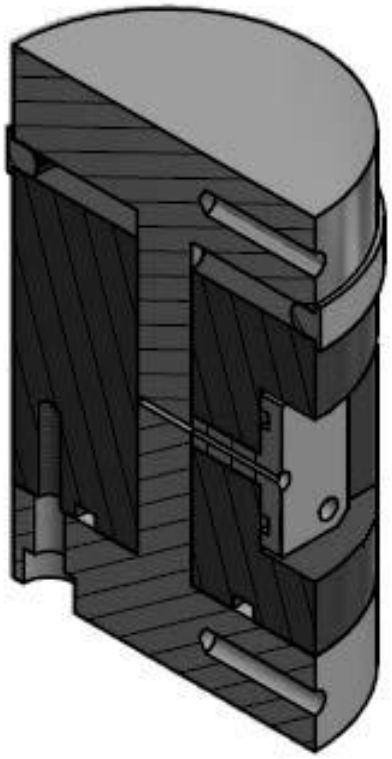

Figure 34 The design of the inhouse LiS cell modified for three electrode setup

In order to be able to perform impedance measurement at a third electrode, a hole with a diameter of 0.6 mm was drilled in the middle of the PEEK casing. Figure 35 shows the setup that was used for Li-S battery cycling.

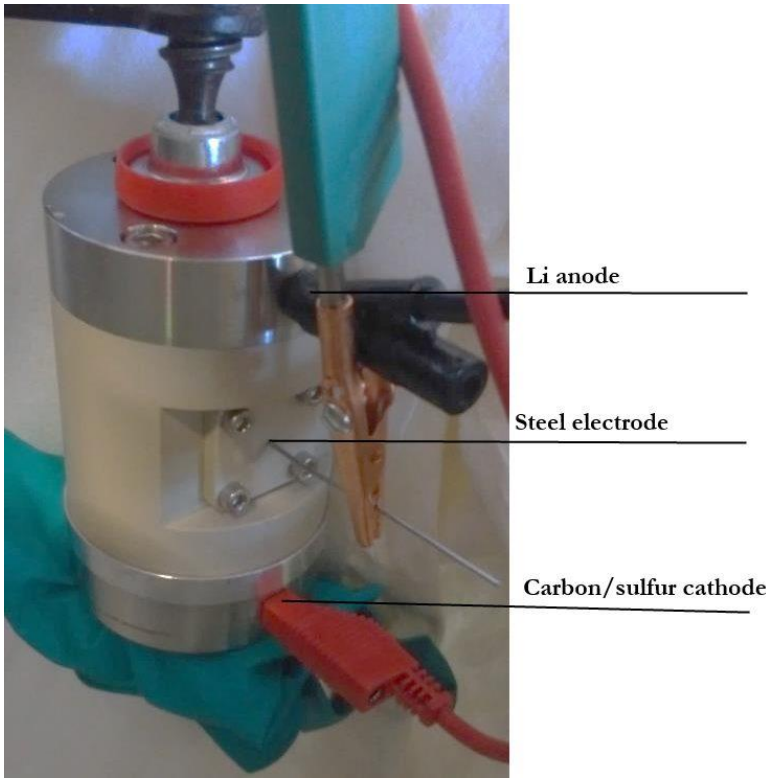

Figure 35 Three electrode setup during measurment with steel wire as third electrode

Steel was chosen as third electrode material mainly due to its mechanical strength. The first test with copper were indeed not successful and we suspected the wire to bend and provoke short-circuit. Before inserting the steel wire, it was platted with Li to serve as Li/Li^+ reference.

4.5.3 SEM/ESD/TEM

SEM images were recorded using the following microscopes:

- Hitachi TM3000 tabletop microscope (Hitachi High technologies American Inc) with acceleration voltage of 15 keV,
- Carl Zeiss Supra 35 with acceleration voltage of 10 keV,
- Carl Zeiss Merlin Field Emission Scanning Electron Microscope with acceleration voltage of 9-15 keV

SEM measurements were performed using a specially designed transportation chamber that allows transport from the glovebox to the microscope, preventing the contact with air and moisture.[92] EDS spectra were recorded using the Hitachi TM3000 tabletop microscope (Hitachi

High technologies American Inc). TEM images were recorded using a JEOL JEM 300F microscope with a 300 kV field emission gun.

4.5.4 Raman Measurements

Raman measurements were performed using a Renishaw inVia spectrometer and the laser diode of wavelength 785 nm. For most of the measurements, an Olympus 50x MPlan objective was used. For the heating measurements, a Linkam stage (TS1200, Linkam Scientific) was used.

4.5.5 X-Ray Measurements

XRD measurements in this work were performed using a Bruker D8 Advance diffractometer. The samples were set in a rotating sample holder to improve representability of the sample. To protect $LiBH_4$ from moisture, polyethylene films were used to seal the sample in the sample holder. We used Cu-Kα radiation.

4.5.6 NMR

Magnetic angle spinning nuclear magnetic resonance (MAS-NMR) measurements for pure $LiBH_4$ were performed using a Bruker AVANCE III HD 400 WB spectrometer with an Ascend wide-bore (89 mm) using a 4 mm probe and MAS frequency of 6 kHz. MAS-NMR measurements for $LiBH_4$-SiO_2 and $LiBH_4$ - $LiBF_4$ composites were measured using a 9.4 T magnet and a Bruker AVANCE III HD 700 WB spectrometer with Ultra Shield Plus wide-bore (89 mm) and a 16.4 T magnet using a 2.5 mm probe and MAS frequency of 15 kHz.

MAS-NMR spectra for ^{7}Li and ^{11}B nuclei were recorded with pulse powers of 130 kHz and 100 kHz respectively. For decoupling measurements, low power ^{1}H continuous wave decoupling program was used with the decoupling power optimized to achieve best spectral resolution. MAS-NMR spectra for ^{1}H nuclei were recorded with "Depth" pulse sequence [93] to minimize the contribution from background signals coming from the probe and the components of the rotors. In these "depth" experiments, ^{1}H pulse power of 110 kHz was used. Temperature calibration for the variable temperature experiments has been performed using lead nitrate following a procedure described by Bielecki, et al.[94]

4.5.7 LiPON Layer Deposition

All experimental work with Lipon thin layer deposition was performed by Senior researcher Eugen Stamate, Section of Electrochemical Materials and Interfaces, DTU Energy.

Lipon thin films were deposited with reactive radio frequency (RF) magnetron sputtering, using 2 inch Li_3PO_4 targets (Kurt Lesker) under nitrogen atmosphere. In order to remove any impurities from the surface of the targets, presputtering of the target was performed for 1 h before deposition. Sputtering of Lipon thin layers was done using low nitrogen pressure (5 mTorr) and moderate RF power (100 W). For a more detailed description of sputtering parameters, see Christiansen, et al. [95]

4.5.8 Synchrotron Measurements

Microtomography

The measurements at the micro-tomography setup at P05 beamline at DESY Petra III (Hamburg, Germany) were made in the EH2 mode with absorption contrast tomography. The detector-to-sample distance was 30 – 40 mm using edge-enhanced absorption contrast setting. The schematic and picture of the capillary Li-S battery used for the microtomography at P05 beamline is shown in Figure 36.

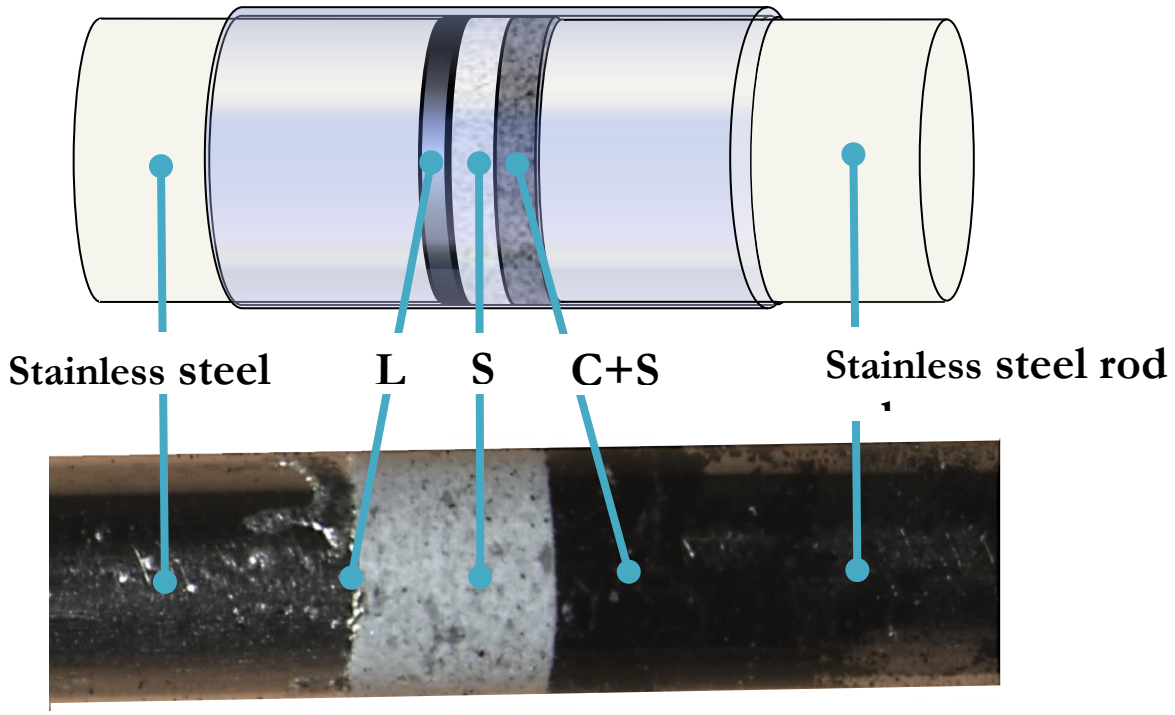

Figure 36 Schematics of a Li-S solid state battery in a quartz capillary. The gray layer is a 30 wt% $LiBH_4$-SiO_2 solid state electrolyte.

The setup used for the measurements on the capillary cells at ESRF (ID20) is shown in Figure 37.

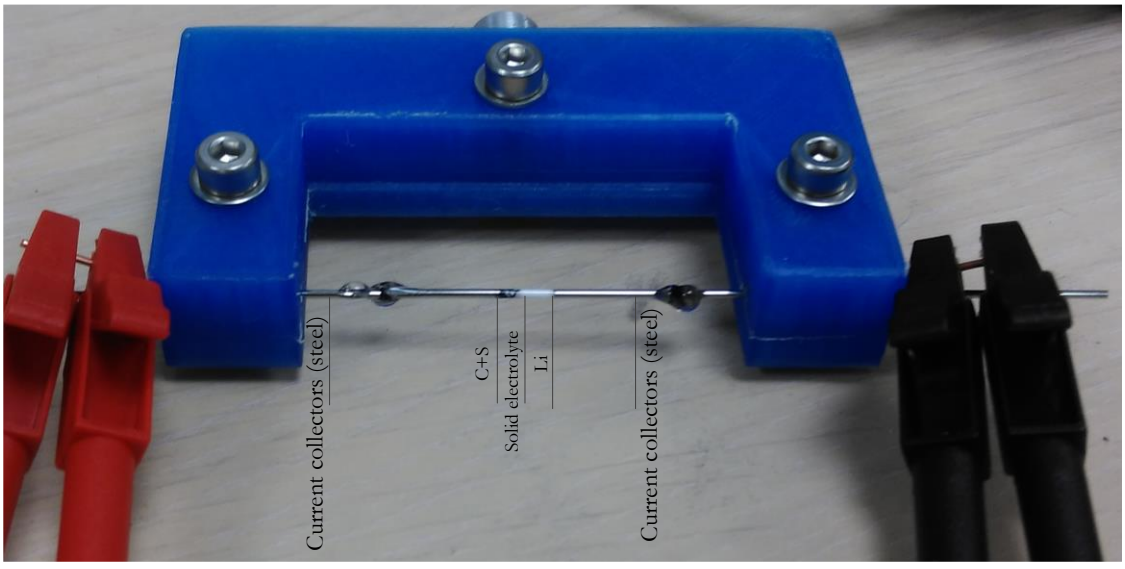

Figure 37 In-house cell made for in-situ measurements at ESRF beamline ID20

XAFS

Figure 38 shows the cell used at the Elettra synchrotron. The setup consists of carbon in sulfur as powder at the cathode side, lithium on the anode side and a steel grid serving as a current collector. In between a pressed pellet of electrolyte was placed.

Figure 38. Cell for in-situ measurements for Elettra showing steel current collector and cathode material

Figure 39 shows the setup at Elettra synchrotron. Assembled cell from Figure 38 is seen connected to electrodes inside of vacuum chamber connected to pumps.

Figure 39 Experimental setup at Elettra: the cell is placed inside a vaccum chamber connected to pumps

Chapter 5

Results and Discussion

This section presents results of studies on all-solid-state batteries with Li-S batteries with solid-state electrolyte based on lithium borohydride, $LiBH_4$-SiO_2 composites and $LiBH_4$-$LiBF_4$.

5.1 Solid State Electrolyte

5.1.1 $LiBH_4$-SiO_2 solid state electrolyte

There has been studies on $LiBH_4$ among other members of complex borohydrides family, nanoconfined $LiBH_4$ in ordered mesoporous silica scaffold has shown to increase conductivity of $LiBH_4$ below phase transition temperature. [96]

5.1.2 Structure and Morphology of $LiBH_4$/SiO_2 composites

Size of $LiBH_4$-SiO_2 domains

In order to make a model to account for Li ion diffusion in $LiBH_4$-SiO_4 solid electrolyte, it is important to study the properties of electrolyte and particle size distribution. Figure 40 shows SEM images of 30/70 wt% $LiBH_4$-SiO_2 electrolyte. Grains in the micron range, agglomerates of $LiBH_4$-SiO2 particles are visible.

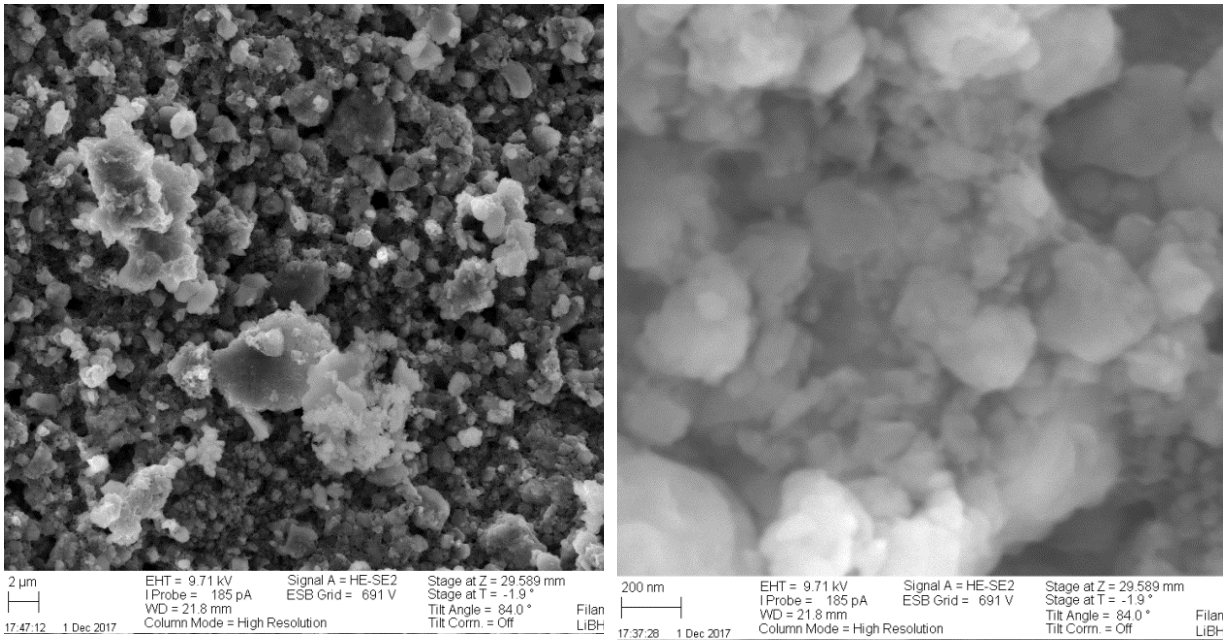

Figure 40 SEM images of 30 wt% $LiBH_4$-SiO_2 composites showing grains in the micrometer range

In order to analyze the distribution of $LiBH_4$ in silica, EDX analysis was performed on the composites. Figure 41 shows an EDX and corresponding SEM image of a 30/70 wt% ball-milled $LiBH_4$ – SiO_2 composite.

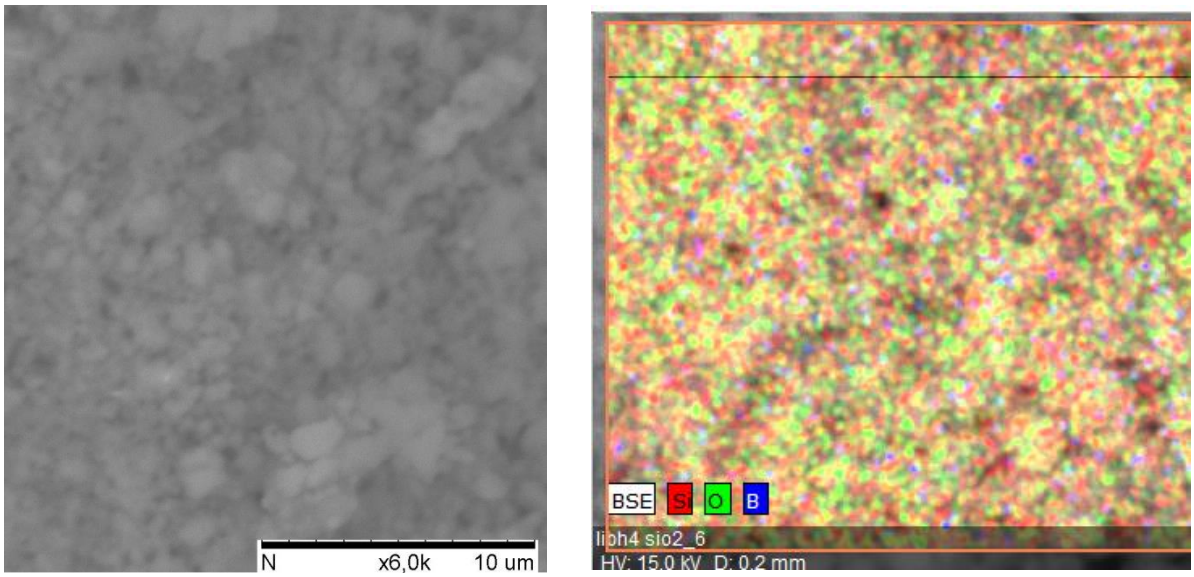

Figure 41 SEM and corresponding EDX image of a 30wt% $LiBH_4$-SiO_2 composite showing distribution of silicon (red), oxygen (green) and boron (blue)

As it can be seen from Figure 41, the distribution of $LiBH_4$ and SiO_2 appears homogeneous. Particle size analysis was performed on dried SiO_2 sample prepared from 30 wt% LiBH4-SiO2 ball milled and washed in acetone to remove LiBH4, the obtained results for put particle size distribution shown in Figure 42 and Table 5.

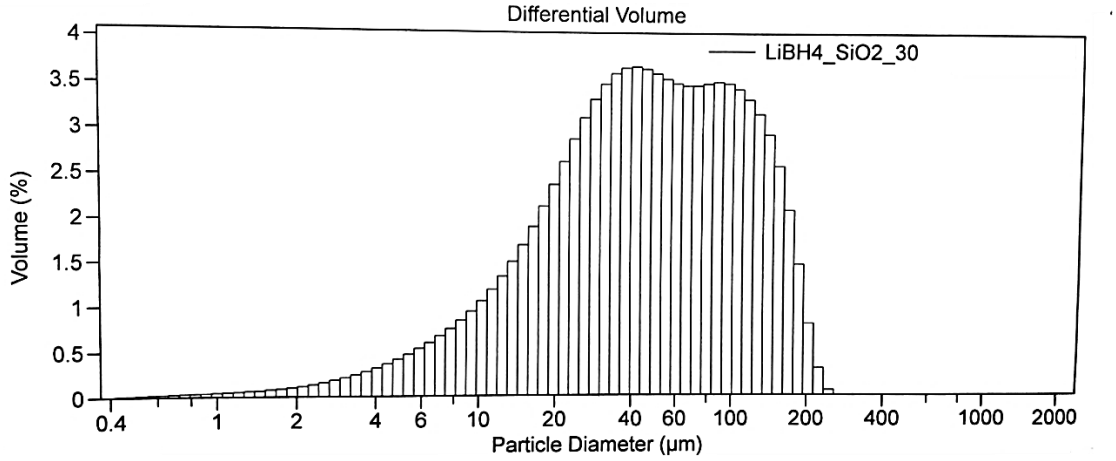

Figure 42 Measured particle size distribution diagram for silica from 30/70 wt% $LiBH_4$-SiO_2 mixtures

Table 5 Particle size distribution for 30/70 wt% $LiBH_4$-SiO_2 composite

	<10%	<25%	<50%	<75%	<90%
Particle size	11.93 μm	24.32 μm	48.16 μm	93.04 μm	140.3 μm

It follows from particle size distribution data, that while smaller particles (<12 μm) are present in powder, the average size of particles is ~ 30μm which corresponds to 40% of the total volume, while the rest is made up by aggregates of several particles. The average size of particles is important to know to model the conductivity as described below.

5.1.3 TGA analysis of SiO_2 aerogel

In order to analyze the stability and find the appropriate temperature to dry the SiO_2 aerogel, Thermal Gravimetric Analysis (TGA) measurements were performed in temperature range from 299 to1168 K. The obtained TGA curve is shown in Figure 43.

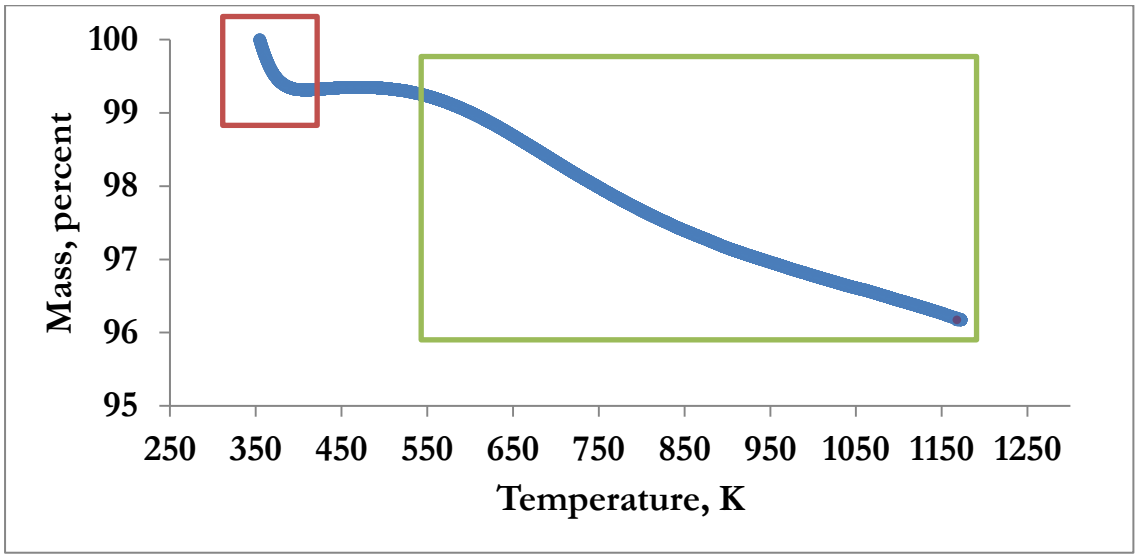

Figure 43 TGA analysis of SiO_2 aerogel. The two major regions where mass losses are observed are due to loss of water (red rectangle) and loss of various types of OH groups in silica skeleton and on the surface.

As it can be seen from Figure 43, two different regions of weight losses are observed. The first region which is marked with a red square is due to removal of surface water.

- Removal of H_2O monolayer from 350 to 375 K

The second region, green rectangle in Figure 43 is due to loss of OH groups:

- Vicinal bridged OH: 550 to 750 K
- Internal and germinal OH from 750 to 1150 K.

During this work and from the analysis of the TGA, the drying of the silica aerogel was performed at 393 K for 12 hours to remove the surface water and avoid its reaction with $LiBH_4$. However, and from the analysis presented in the theoretical section on the hydroxylation and removal of hydroxyl groups based on Zhuravlev's model it could have been beneficial to use a slightly higher temperature, up to 463 K to ensure highest degree of hydroxylation of the silica particles.

5.1.4 Ionic Conductivity of Electrolyte

The results of the ionic conductivity studies of $LiBH_4$-SiO_2 have been previously published in Paper I (Lefevr et al, 2018). [97] This chapter proves new and complimentary results that have not been published to this day.

Electrochemical Impedance spectroscopy (EIS) measurements were carried out on $LiBH_4$ – SiO_2 composites with various composition labelled as wt% of $LiBH_4$ in the below text. Figure 44 shows an example of EIS spectra for a 30 wt% LiBH4 – SiO2 composite where a single semi-circle is observed. Despite of the presence of a single arc, it cannot be excluded that two arcs are overlapping in the spectrum, representing the contribution from bulk and grain boundary conductivity.

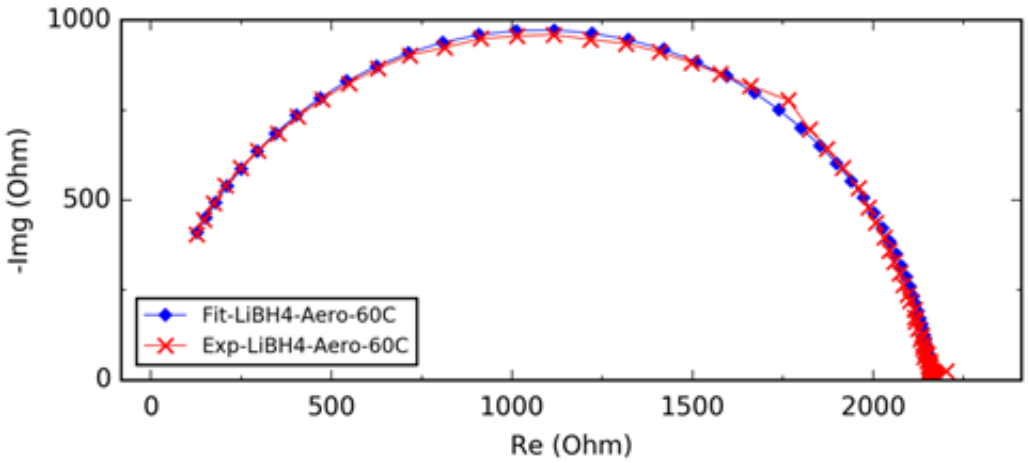

Figure 44 Example of EIS for 30 wt% $LiBH_4$-SiO_2 composite at 333 K (Adapted from Lefevr, et al[97])

Figure 45 show the Arrhenius like plot of the conductivity for the different composites compositions. A large conductivity drop is seen for the pure $LiBH_4$ while $LiBH_4$-SiO_2 composites do not have a significant conductivity drop below the phase transition temperature. It can be seen from Figure 45 that the best conductivity results were achieved for 30 and 40 wt% composites.

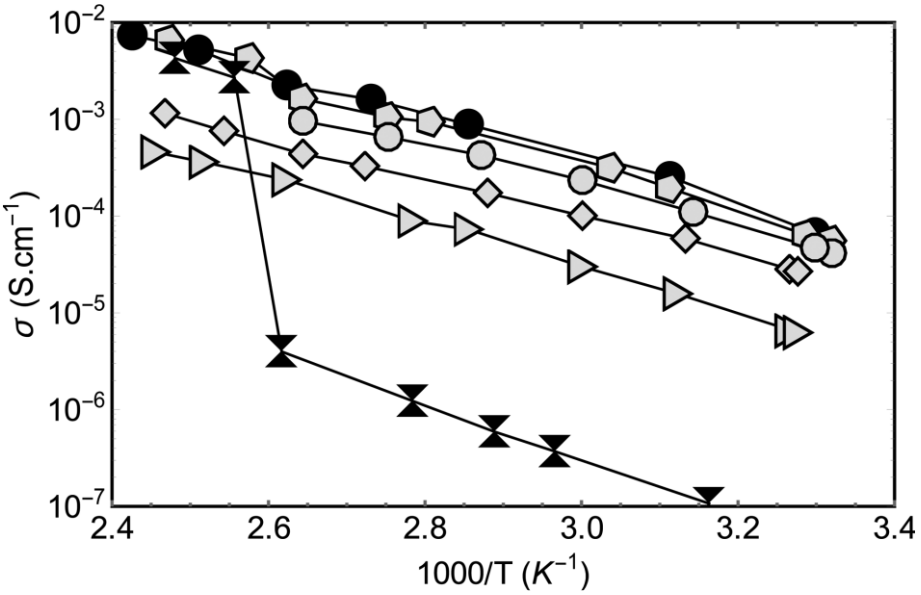

Figure 45 Arrhenius plots of Li^+ conductivity for different ratios of $LiBH_4$ in $LiBH_4$-SiO_2 composites with following wt% of $LiBH_4$: black triangles (90%), gray circles (50%), gray pentagons (40%), black circles (30%), gray sqaure (25%), gray triangles (15%). (Adapted from Lefevr, et al[97])

While no obvious conductivity drop is seen for composites with lower loadings of $LiBH_4$ in Figure 45 and Arrhenius plots may look like straight lines for all composites, smaller conductivity drops do exist for higher loadings of $LiBH_4$. These changes in conductivity are similar to the one of pure $LiBH_4$ show that for higher loadings, a major part of $LiBH_4$ is not affected by mixing with silica. For lower loadings, only smaller curvatures are observed. The reasons for this will be discussed in details in section 5.1.7.

Logarithms of the conductivities at 303 K, normalized to the conductivity of pure $LiBH_4$ at the same temperature are shown in Figure 46. The activation energies for Li conduction, obtained from the Arrhenius plots logarithms of conductivities are shown in inset in Figure 46. It is clear that the lowest activation energy among the composites is obtained for the 30 wt% sample.

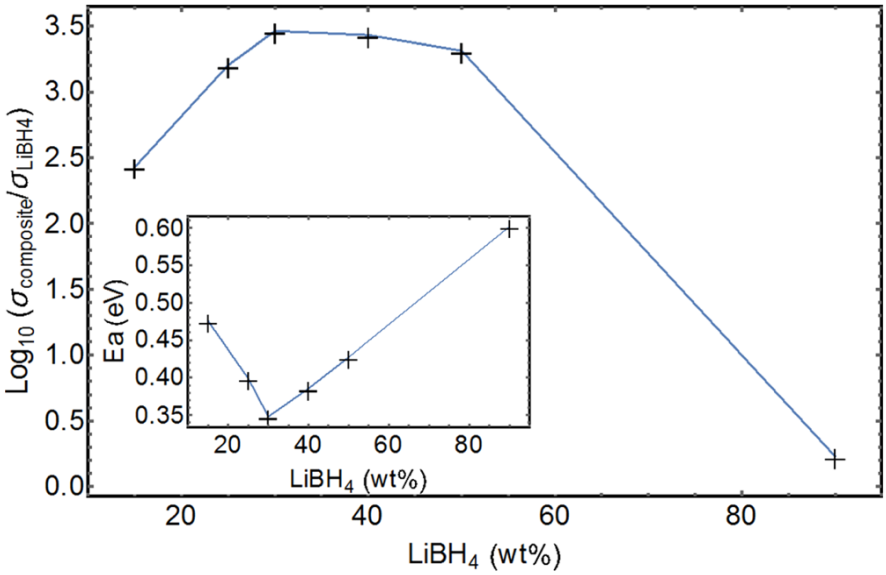

Figure 46 Logarithm of conductivities of $LiBH_4$-SiO_2 electrolyte normalized to conductivity of pure LiBH4 at 303 K. The insert shows activation energies obtained from slopes of Arrhenius plots (Adapted from Lefevr, et al[97])

Choi, et al[53] have also investigated $LiBH_4$ ball milled with MCM-41 and fumed silica, and obtained higher values of conductivities for their $LiBH_4$-SiO_2 composites (55 vol% equivalent to our 30 wt% composites). We obtained lower conductivity values but also lower activation energies (0.35 eV compared to 0.43 eV as calculated by Choi, et al[53]) for an equivalent stoichiometry. As for the difference in conductivity values, that are slightly lower than those obtained by Choi, the discrepancy can come from difference in sample preparation or pressure applied when producing the electrolyte pellet. Another important difference could be the size of silica particles, drying temperature and presence of pores that will have an important effect for surface chemistry.

The highest conductivity values, for the composites, are seen for 30 and 40 wt% of $LiBH_4$. The optimal $LiBH_4$-SiO_2 composition is due to a competition between the surface area of the SiO_2 particles, providing the interfacial conductive layer (this will be explain later on in section 5.1.7) and the need to have a percolation network of the interfacial conductive layer.

5.1.5 XRD Measurements

The diffraction patterns for 30/70 wt% $LiBH_4$-SiO_2 composite and pure $LiBH_4$ are shown in Figure 47. For the comparison, the intensity of the pattern for pure $LiBH_4$ has been divided with 100 to match the intensity of the pattern for the $LiBH_4$-SiO_2 composite. It reflects that there is less amount of $LiBH_4$ in the second sample. The part of the diffractogram between 21 and 23

degrees is removed as it contains peaks coming from polyethylene film used to protect $LiBH_4$ from exposure to air and moisture.

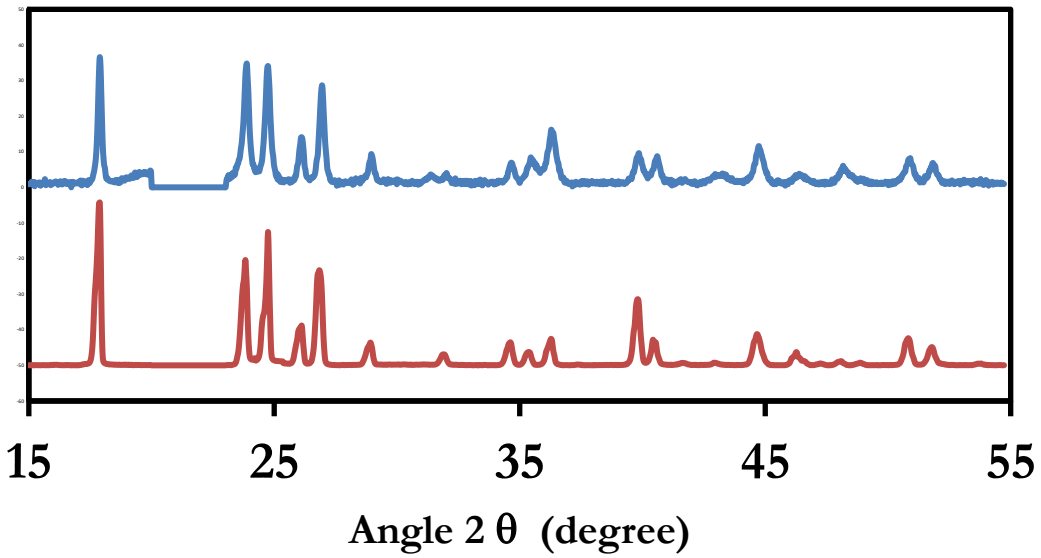

Figure 47 XRD patterns of 30/70 wt% $LiBH_4$-SiO_2 (blue) compared to pure $LiBH_4$ (red)

It can be seen from Figure 47, that overall the position of the peaks for pure $LiBH_4$ and 30/70 wt% $LiBH_4$-SiO_2 composite are the same. There are otherwise a few mismatches in the peak intensities. It could be due to formation of lattice defects during ball-billing of the composite but also there is overlapping with the peak from the polyethylene film and SiO_2 aerogel (Figure 48).

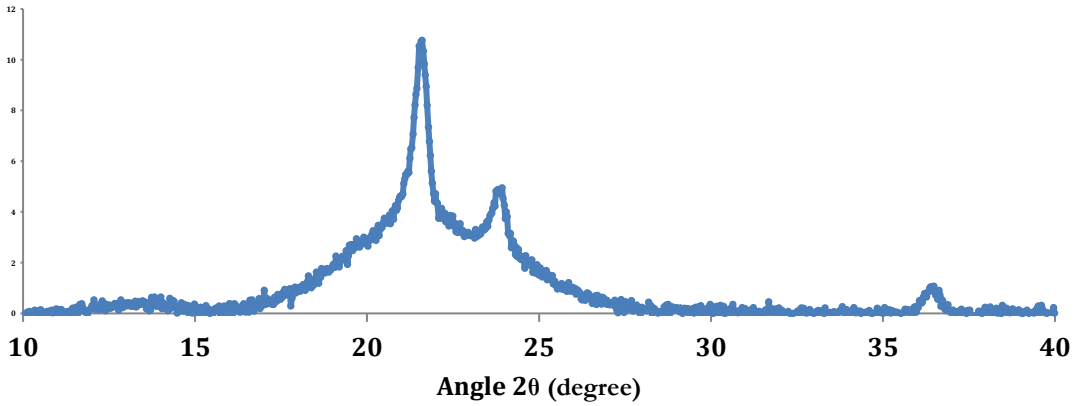

Figure 48 XRD pattern of $SiO_2$with protective polyethylene film. Most of the peaks come from the film.

One can conclude here that most of the $LiBH_4$ is in the low temperature orthorhombic structure after ball-milling with SiO_2.

5.1.6 Raman Measurements

As it was shown in section 5.1.4, the conductivity values for 30/70 wt% $LiBH_4$-SiO_2 are several orders of magnitude higher than the conductivity of pure $LiBH_4$ which indicates modification of some part of the $LiBH_4$ in the mixture already at room temperature. The XRD studies did not show the formation of new compounds in the composites that could account for higher ionic conductivity of the composites.

We have performed Raman measurements on the 30/70 wt% $LiBH_4$-SiO_2 sample in temperature range from 293 to 393 K to analyze changes in vibration of the BH_4^- with increased temperatures and how these might be related to increased conductivities of the composites.

Pure $LiBH_4$ at room temperature has point group symmetry Cs (space group Pnma). Figure 49 shows Raman spectrum of pure $LiBH_4$ at 293 K measured in range 2100-2600 cm^{-1}. Three internal BH_4^- vibrations ($4\upsilon_4$, υ_3, υ_1), out of the seven, are present in the studied range together with combination bands. The υ_2 mode is present in the spectrum at 1286 cm^{-1} but is not shown in Figure 49.

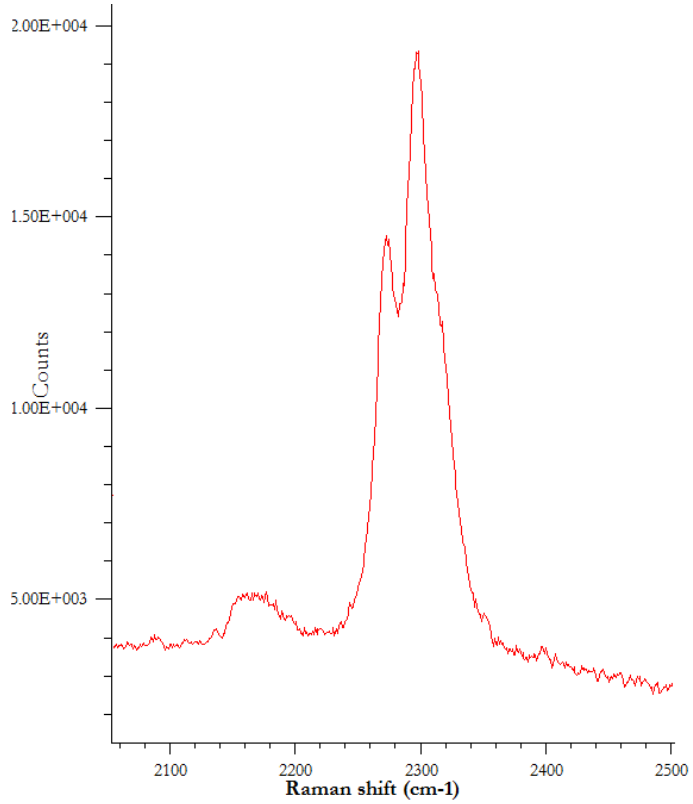

Figure 49 Raman spectrum of pure $LiBH_4$ at 293 K showing $4\upsilon_4$, υ_3, υ_1 modes

Table 7 shows assignment of observed peaks on the basis of previously reported values for pure $LiBH_4$.[98] No new peaks or signs of decomposition (H_2 gas has been reported in previous studies[99]) have been observed in the range 2100-2600 cm^{-1}.

Table 6 Experimentally observed peaks for pure LiBH4 at 293 K and their assignment

Peak, cm^{-1}	Mode
2160	$4\upsilon_4$
2275	υ_3
2300	υ_1
2321 (shoulder)	Observed in the literature but not assigned[98]
2390	Combination bands
2490	Combination bands

After the phase transition at 384 K, the symmetry of $LiBH_4$ is increased to C_{3v}. As reported in the literature, broad υ_3 mode is observed masking the presence of other peaks in the range from 2200 to 2400 cm^{-1}. [98] Figure 50 shows the recorded Raman spectrum of pure $LiBH_4$ above the phase transition temperature showing a single broad peak at 2300 cm^{-1} due to the overlapping υ_3, υ_1 and 4 υ_4 modes.

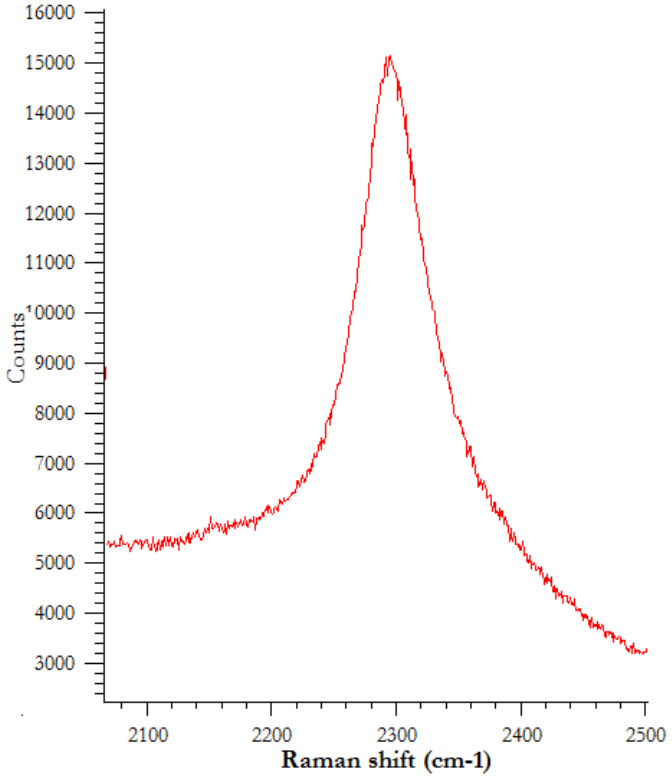

Figure 50 Raman spectrum of pure $LiBH_4$ at 393 K showing broad υ_3 mode masking the $4\upsilon_4$ and υ_1 modes

While the ν_1 and ν_3 can be distinguished at temperatures below 384 K, clear line broadening is observed with increased temperatures. While the symmetry of the system is increased above the phase transition temperature, the broadening of the spectra shows presence of disordered array, although borohydride anions are becoming more symmetric: from m-C_s to 3m - C_{3v}.[98] The observed spectral changes, during the heating process, indicate dynamic disorder of the borohydride anions, with large amplitude of the librational motions rather than free rotations.[98]

After obtaining spectra of pure $LiBH_4$ below and above the phase transition temperature, we have recorded the spectra of $LiBH_4$-SiO_2 composites. As the composites show no significant drop of conductivity below and above the phase transition temperature, we expected to see a broader υ_3 mode as for the high temperature $LiBH_4$ but at room temperature. Figure 51shows Raman spectrum of a 30-70 wt% $LiBH_4$-SiO_2 composite at 293 K. As expected, the spectrum is broader than the one for pure $LiBH_4$ which is showing higher level of disorder in the arrays of borohydride anions.

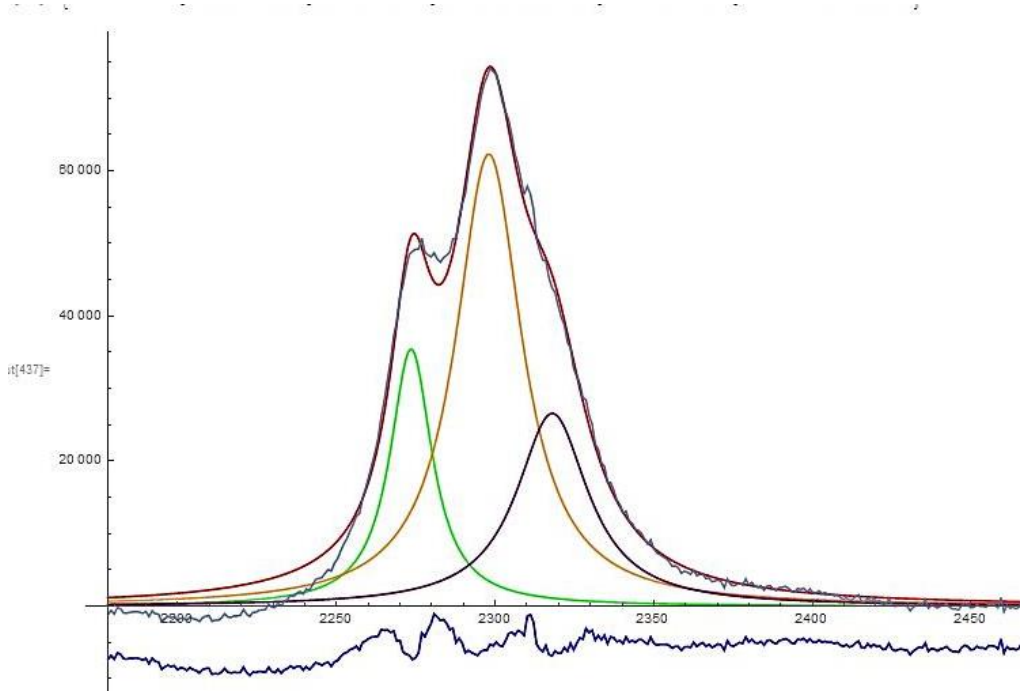

Figure 51 Raman spectrum of a 30/70 wt% LiBH4 SiO2 at room temperature (green, orange and purple lines υ_3, υ_2, modes, blue line is the difference between calculated and actual spectrum)

Similar peak broadeing is observed for pure $LiBH_4$ however at higher temperatures (in range 323-333 K). Table 7 is showing assignment of observed peaks for pure $LiBH_4$ range 2100-2600 cm^{-1}:

Table 7 Observed peaks for pure $LiBH_4$ at 343 K and their assignment

Peak, cm^{-1}	**Mode**
2160	**Weak:** υ_4
2275	υ_3
2300	υ_1
2321 (shoulder)	Observed in the literature but not assigned[98]
2390	**Not observed:** Combination bands
2490	**Not observed:** Combination bands

For the composite, the combination peaks are disappearing already at room temperature while it was first observed around 360 K for pure $LiBH_4$.

Figure 52 shows spectrum of a 30 wt% $LiBH_4$-SiO_2 composite at 343 K. As it can be seen, already at temperatures close to 343 K, υ_3 and υ_1 modes in the vibrational spectrum of 30 wt% LiBH4-SiO_2 composite are becoming so broad that they merge into one peak. With heating above 343 K, only one broad peak is observed.

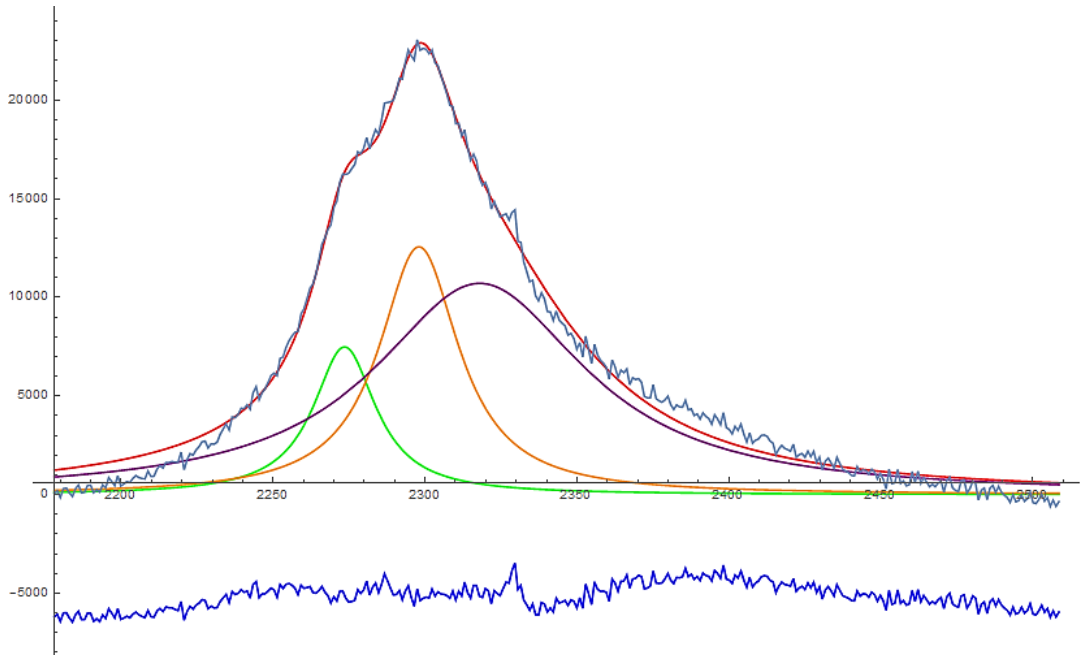

Figure 52 Raman spectrum of 30/70 wt% LiBH4-SiO2 composite at 343 K (green, orange and purple lines υ_3, υ_2, modes, blue line is the difference between calculated and actual spectra)

This spectrum corresponds to spectra of pure $LiBH_4$ after phase transition temperature at 384 K. This indicates that the rotations/vibrations of the borohydride anion

This Raman study revealed that the 30/70 wt% composite has rotational/vibrational characteristics similar to pure $LiBH_4$ but with shifted temperatures. Already at room temperature the composite got similar Raman Spectrum of the pure at 360 K and at 343 K it a spectrum seen for pure $LiBH_4$ just before the phase transition. This means that by ball-milling with silica causes structural changes, providing a greater level of disorder in the system resulting in broader Raman shifts and reduced number of visible peaks.

As for the fitting of components shown in Figure 52, different bonds have different polarizability, therefore it is not possible to make a quantitative analysis of the amount of the phases present in the spectra of the 30/70 wt% composite based on the results of Raman measurements alone. The quantification of phases is however possible by means of NMR spectroscopy which will be discussed in detail in following sections.

5.1.7 Ion mobility studied by NMR

In this section, ion dynamics in $LiBH_4$ were studied by solid-state NMR. MAS-NMR spectra of ^7Li, ^{11}B and ^1H were recorded and analyzed, furthermore spin-lattice relaxation times and exchange studies were performed for ^7Li nuclei to study the time scale of Li ion motions in $LiBH_4$-SiO_2 composites.

Some of the results of ion mobility studies shown in this section have been previously published in Paper I (Lefevr et al, 2018).[97] 6This chapter proves new and complimentary results that have not been published yet.

5.1.7.1 Proton NMR

The behavior of pure $LiBH_4$ is well-studied in the literature and a study of the BH_4^- reorientations was carried out by Corey et al. who studied the mobility of H ions by relaxation of the dipolar-ordered state, T_{1D}, times and full width at half maximum (FWHM) line widths.[100] Previous studies of proton NMR in pure $LiBH_4$ show a broad central transition at room temperature with slight narrowing towards phase transition temperature. [101] Single pulse proton resonance of

$LiBH_4$-SiO_2 composites was measured and compared to that of pure $LiBH_4$ which shown in Figure 53.

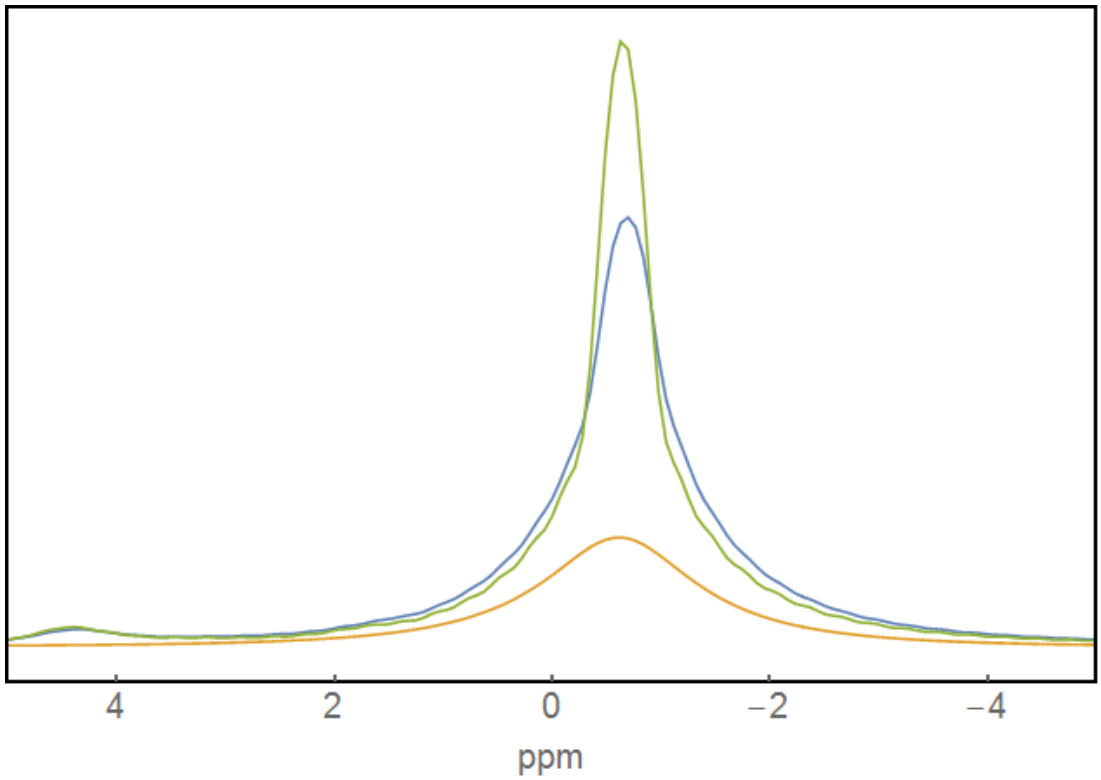

Figure 53 Proton NMR of pure LiBH4 (orange) at 293 K compared to 30/70 wt% LiBH4-SiO2 composites at 293 K (blue) and 325 K (green)

While a single component is seen in spectrum of pure $LiBH_4$ (shown as orange) which is in agreement with previous results by Corey, et al [101], proton resonance of 30/70 wt% composite shows 2 components that are overlapping: a Gaussian component similar to the one of pure $LiBH_4$ and a narrower Lorentzian component that is only present for the $LiBH_4$-SiO_2 composites. Already at room temperature the recorded spectra show greater line narrowing than the spectrum of pure LiBH4 and as it can be seen it becomes even more pronounced with increasing temperatures.

In order to study motional narrowing as a function of temperature, single pulse ^1H experiments were carried out for different loadings of silica and at different temperatures. Fitting of the two components was performed for different loadings of silica in $LiBH_4$-SiO_2 composites and pure $LiBH_4$ and obtained results are shown in Figure 54.

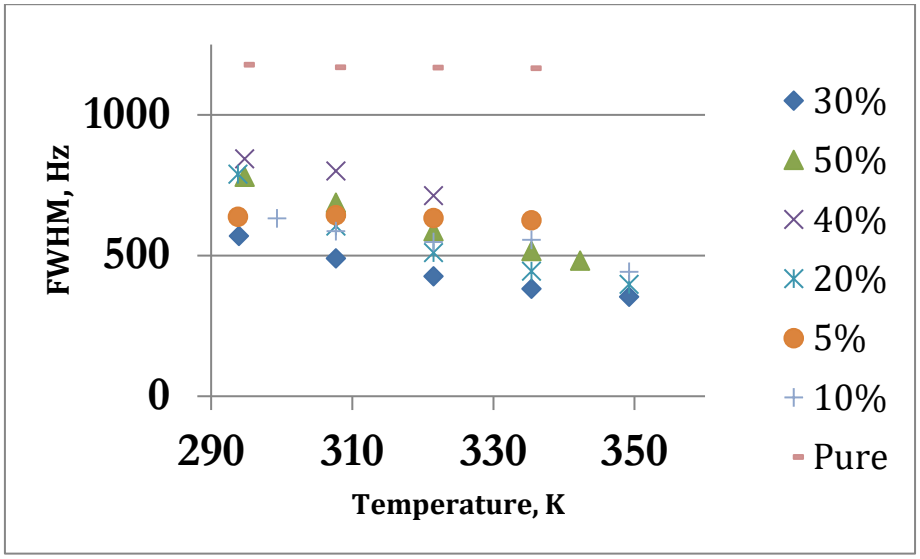

Figure 54 FWHM for the Lorentzian component as a function of temperature

As it is shown in Figure 54, the width of the central transition of pure $LiBH_4$ did not change significantly during heating which was expected and in agreement with previous studies showing that the proton resonance for pure $LiBH_4$ does not change below the phase transition temperature. [100] The mixtures exhibit a significant line narrowing until th e phase transition temperature indicating higher mobility of the protons. The narrowing is observed especially well for the 30 wt% composite where the mobility is the highest.

Motional narrowing of the Lorentzian component has been previously seen in literature for mixtures of e.g. $LiBH_4$ in carbon networks[102] and was associated with two types of proton environments: inside and outside of carbon scaffolds which is likely to represent two types of environment in the $LiBH_4$-SiO_2 as well.

^{7}Li NMR

In order to study lithium ion mobility, four types of experiments were performed on pure $LiBH_4$ and 30/70 wt% $LiBH_4$-SiO_2 composite: single pulse measurements, high-power decoupling, spin-lattice relaxation time measurements (T1 times) and exchange measurements (EXSY). While the former two methods provide data on types on Li ion motions in the samples, the former two methods give an estimate of the time scale at which the Li jumps are occurring between sites in crystal lattices.

^{7}Li Single pulse spectra

Study of lithium ion mobility was performed for pure $LiBH_4$ and composites with different wt% of SiO_2. The single 7Li resonance of pure $LiBH_4$ is showing a single peak at -1.4 ppm while the composites are showing an overlap of a Lorentzian component at -0.69 ppm and a Gaussian component at -1.1 ppm which as shown in Figure 55.

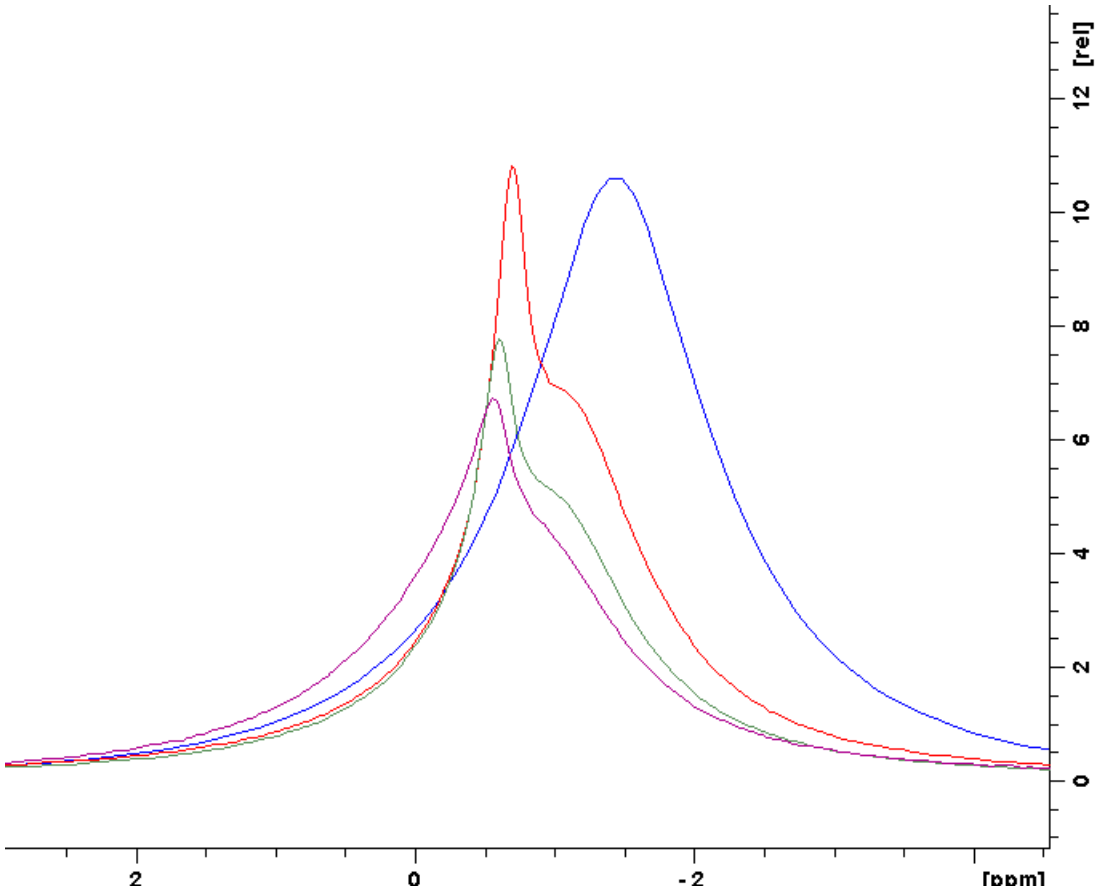

Figure 55 ^{7}Li single pulse spectra for 10 (purple), 20 (green), 30 (red) wt% $LiBH_4$-SiO_2 composites compared to pure $LiBH_4$ (blue)

It is clear from Figure 55 that the two components for the composites are different from the single component for pure $LiBH_4$ proving the assumption that during ballmilling of $LiBH_4$ and SiO_2, not only size reduction has occurred but a new Li environment is created that is clearly different from the one in pure $LiBH_4$. We can assume that the two peaks represent two Li populations where one is more mobile (Lorentzian component) and the other one is more like the population in pure $LiBH_4$ and is less mobile (Gaussian component).

Fitting of the areas under the peaks for the two components was performed for different wt% of SiO_2 and the results are shown in Figure 56.

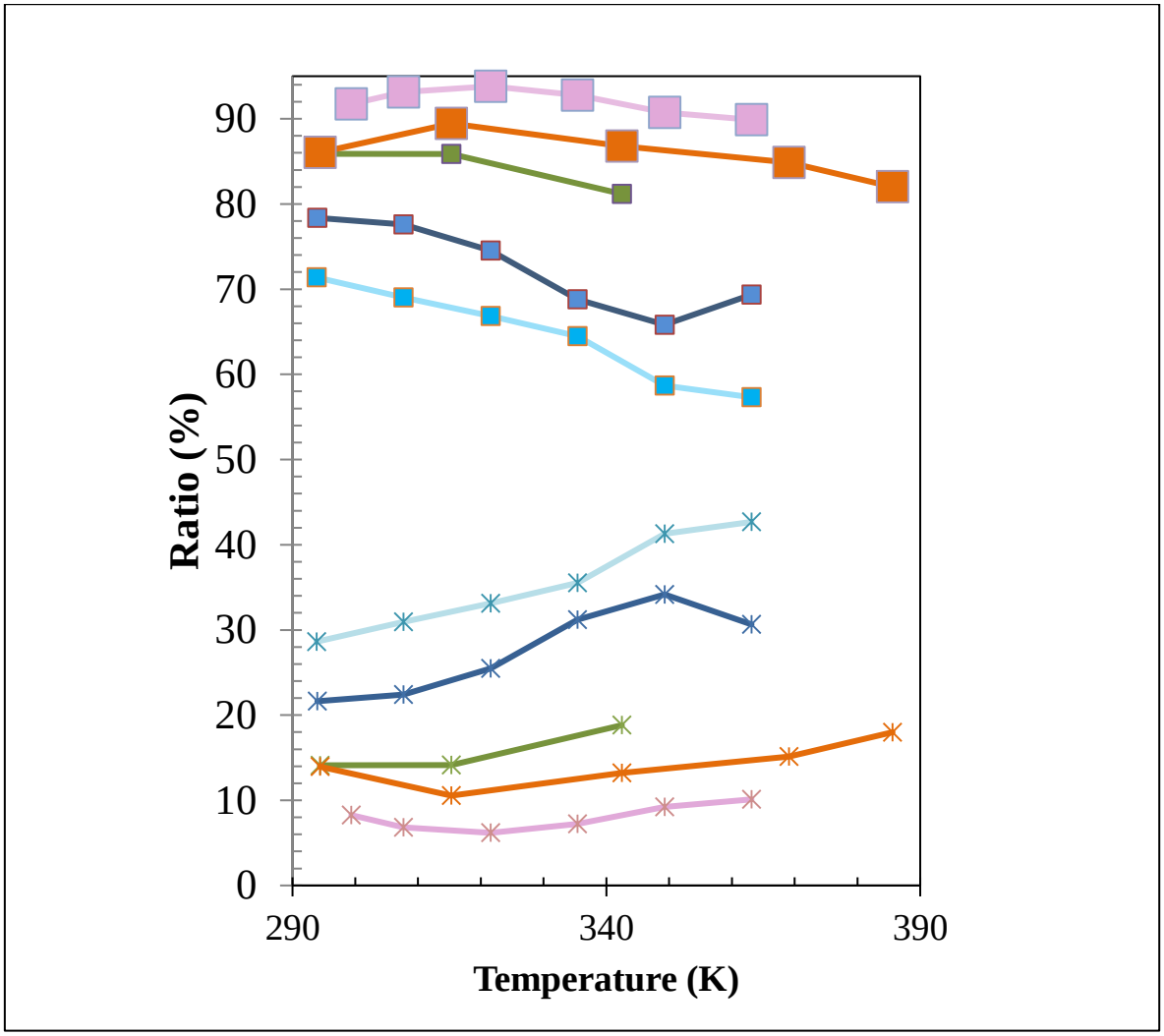

Figure 56 Ratios of the two components: Pink (10%), Light blue (20%), blue (30%), green (40%), orange (50%)

The highest ratios of the second component is observed for the 20 and 30wt% samples which is in good agreement with the results of conductivity measurements. Lowest values are observed for 10 wt% and 50 wt%. The model of Li ion conductivity in $LiBH_4$-SiO_2 will be discussed in detail in the following section.

T1 measurements for ^{7}Li

T1 measurements were performed on pure $LiBH_4$ and $LiBH_4$-SiO_2 composites to study if the composites would show two Li populations, a "fast" and a "slow" one, which was seen from single pulse measurements reported in the previous section.

Figure 57 shows T1 times measured for pure $LiBH_4$. It can be seen that T1 times are increasing with increasing temperatures which was expected in the temperature range up to phase transition

temperature from previous studies. [103] Fitting of signal intensity to one T1 component gave a good fit which supports the idea that only one type of Li is present in pure $LiBH_4$.

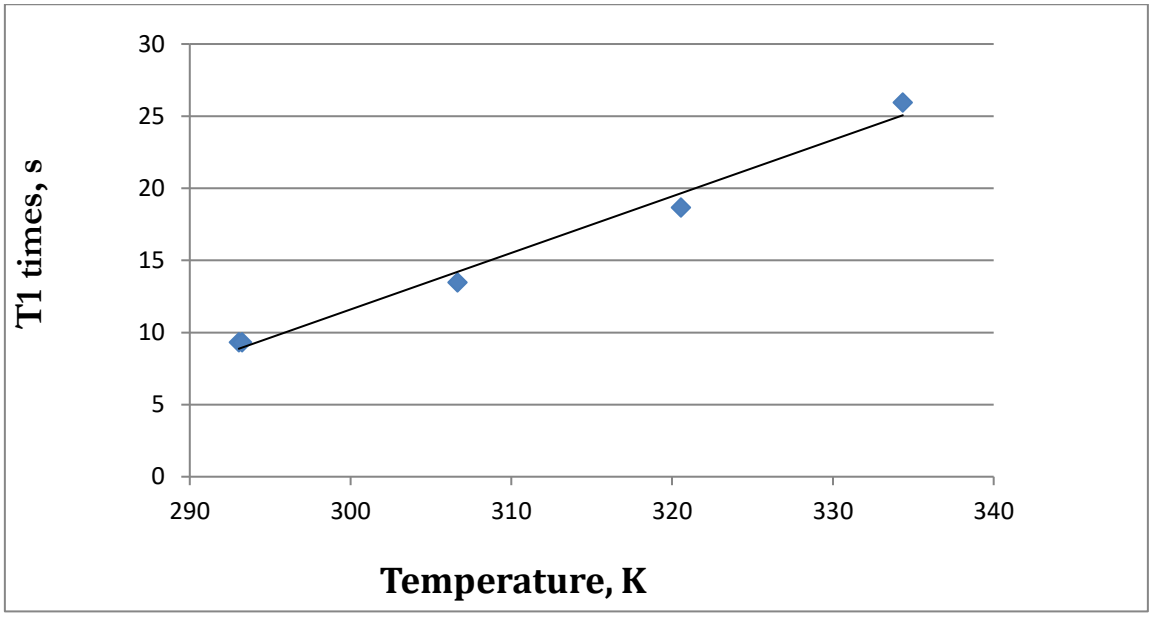

Figure 57 T1 times for pure $LiBH_4$ sample

T1 measurements were carried out on $LiBH_4$-SiO_2 composites with different ratios of SiO_2. Obtained signal intensity as a function of temperature was fitted with 1 component which gave a poor fit as shown in Figure 58.

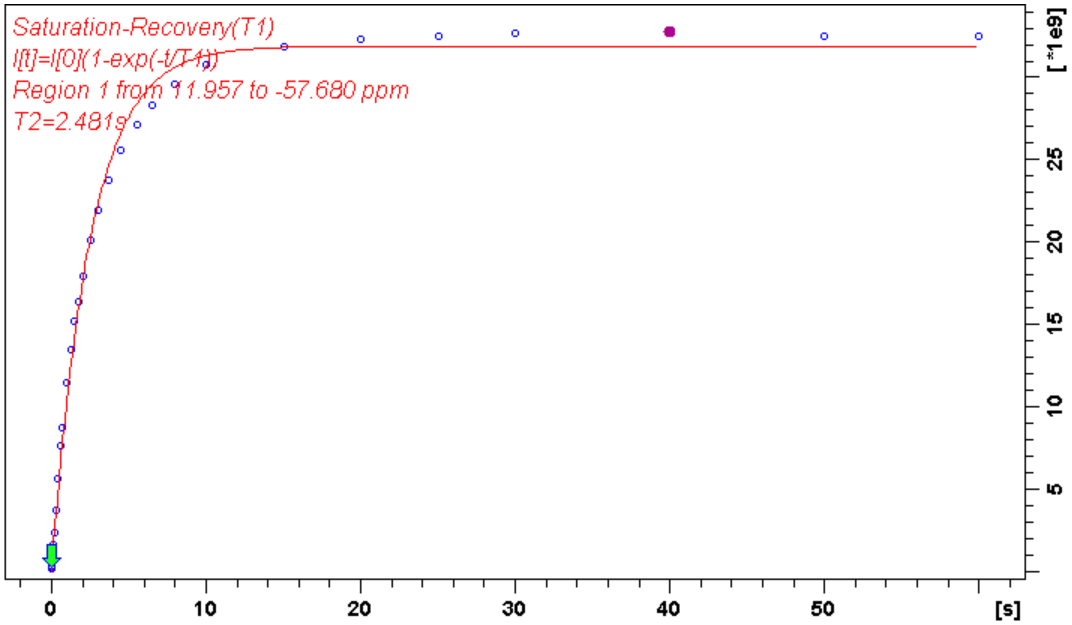

Figure 58 Fit of reovery time to a single component

Therefore, fitting was performed with 2 components and better results were obtained. It shows that more than one type of behavior is observed in the composites unlike pure $LiBH_4$ where only

one population is observed. A fast and a slow components for the composites are observed. For example, for a 15/85 wt% composite, a component with T1 3-4 seconds and a component in the millisecond range were found. While the first component is constant with increasing temperature, the second component is decreasing with temperature, as shown in Figure 59.

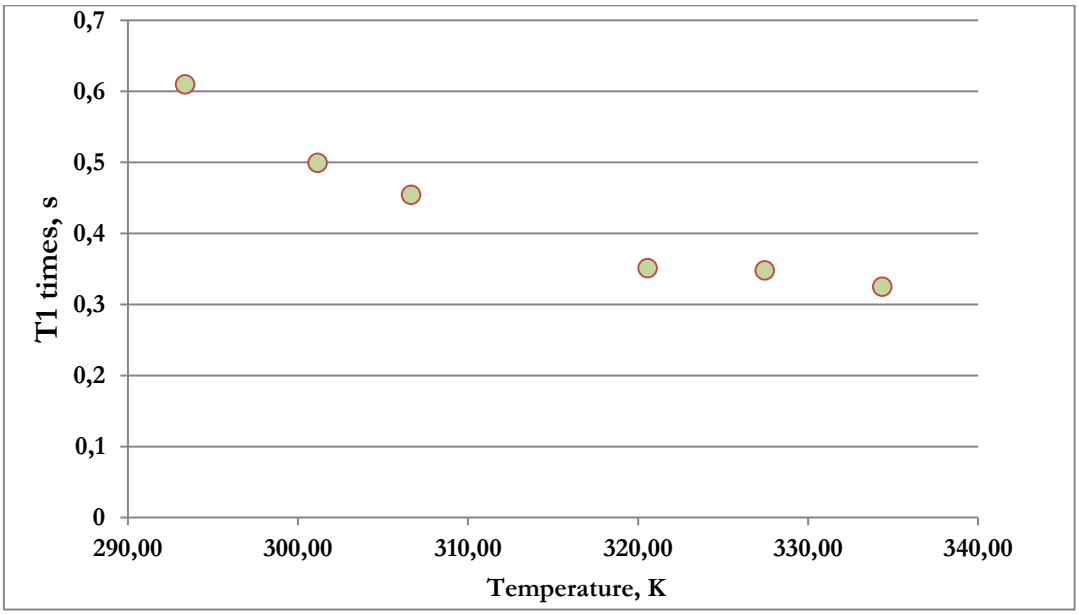

Figure 59 T1 time for "fast" component in 85/15 wt% $LiBH_4$ SiO_2 sample

Fitting was performed for different wt% of SiO_2 and obtained T1 times for "fast" and "slow" components differ between different loadings of silica. It indicates that firstly the mechanism of spin-lattice relaxation are different for different loadings due to a percolation threshold, secondly that the techniques used for the T1 relaxation measurements is limited and won't allow to distinguish between 2 or more components with different but may be closed T1 times. While pure $LiBH_4$ clearly shows one lithium population, the T1 relaxation measurements for the composites show more than one component and we fitted the results, with a reasonably good accuracy, with 2 T1 making the assumption that two different populations of Lithium were present. In reality, the transition between these two populations, if they exist, must be smooth and most probably a "continuous distribution" of population should be used.

EXSY for Li

Exchange measurements are a good tool to investigate exchange between different Li sites in crystal lattice. Exchange measurements were performed at different time scales (delays of 10, 20, 50 and 200ms) and at different temperatures (293 – 341 K). The spectra can be found in appendix in Figure A 1.

Figure 60 shows exchange spectrum for 30/70 wt% recorded at room temperature. It is clear from the figure that off-diagonal peaks indicated with arrows are present in the EXSY spectrum which is indicating that already at room temperature exchange is taking place between the two Li populations corresponding to the "fast" population and the "slow" population..

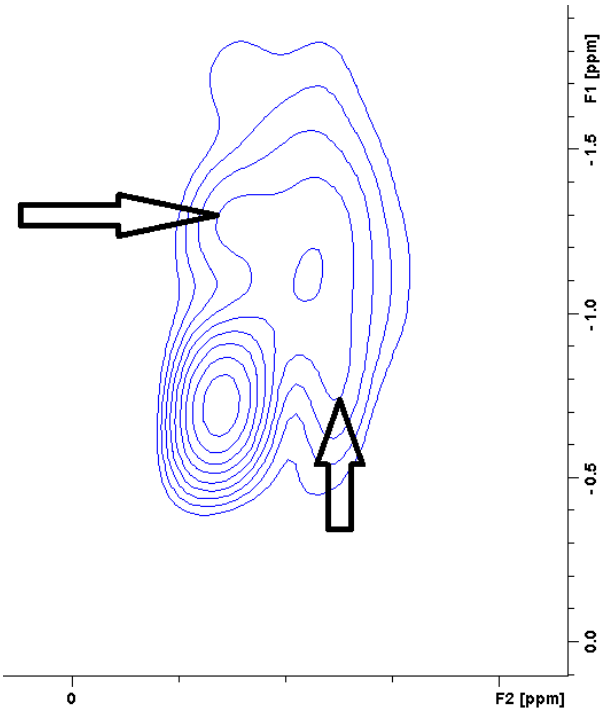

Figure 60 EXSY spectra of Li in LiBH4-SiO2 taken at RT 293 K showing clear evidence of cross peaks.

As it can be seen from Figure 60, the intensities of off-diagonal peaks is not resolved well enough to make quantitative analysis of the data, furthermore it is it likely that the peaks show a distribution of exchange rates, and fitting the intensities to a model would be a difficult task similar to modelling the T1 times presented earlier in this section. However exchange measurements do provide information on time scale of Li jumps and from the obtained spectra it is possible to say that exchange is taking place at time scale of 10 or less ms already at room temperature.

^{11}B NMR

Since we saw seen different populations of Li for the composites, we have performed ^{11}B measurements to see if we could also find different boron population. Figure 61 shows high-power decoupling spectra of 30/70wt% $LiBH_4$-SiO_2. Three components can be seen in the boron resonance

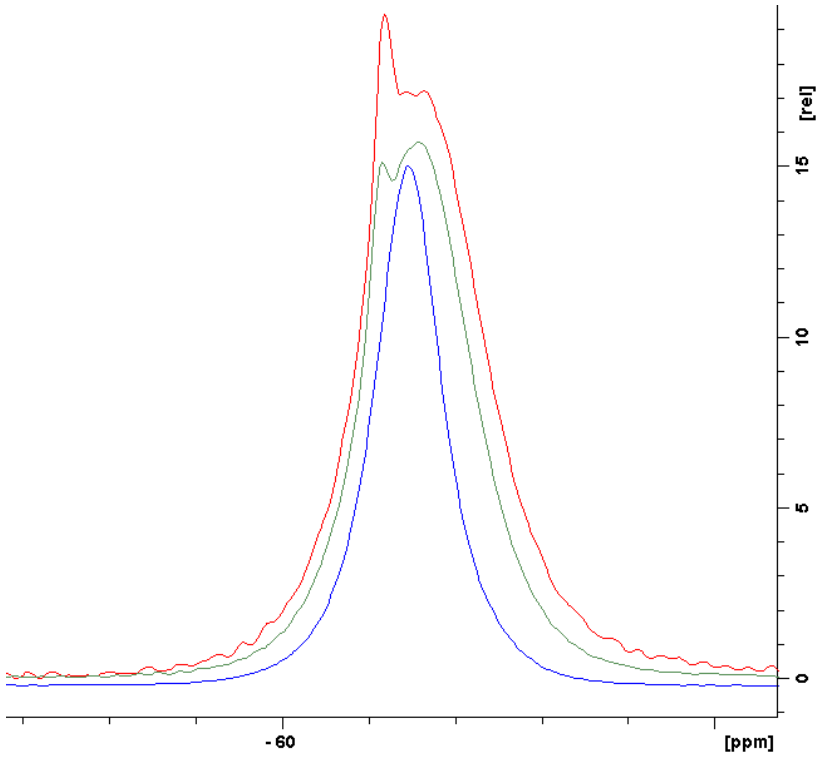

Figure 61 11B high power decoupling spectra of 30 (red), 40 (green) wt% LiBH4-SiO2 compared to pure LiBH4 (blue)

The spectrum collected for the 30 wt% composite was fitted using three Gaussian/Lorentzian components (Figure 62).

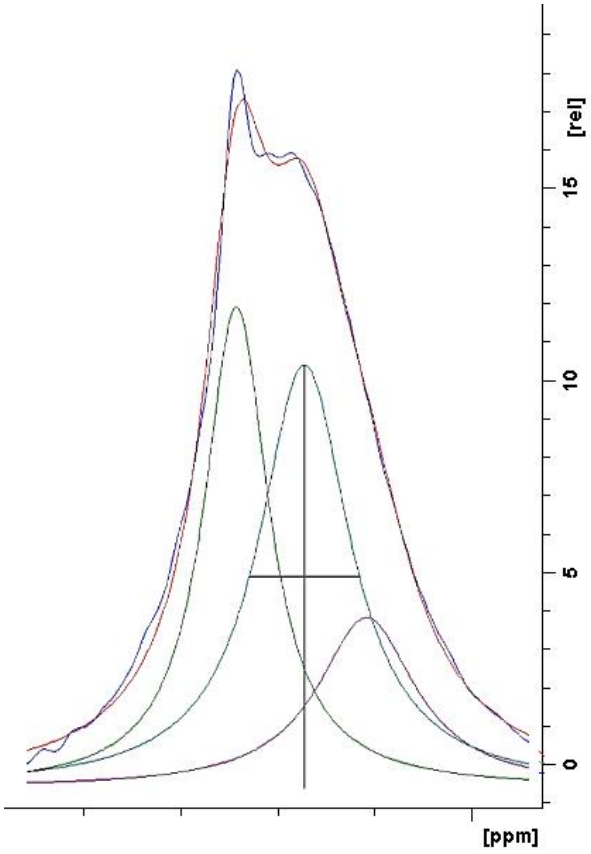

Figure 62 High-power decoupling spectrum of 30/70 wt% $LiBH_4$-SiO_2 composite fitted with 3 components in DMFit Software

The decomposition with 3 components was performed for various temperatures and the obtained percentages of populations calculated from the total area under the peaks are plotted in Figure 63.

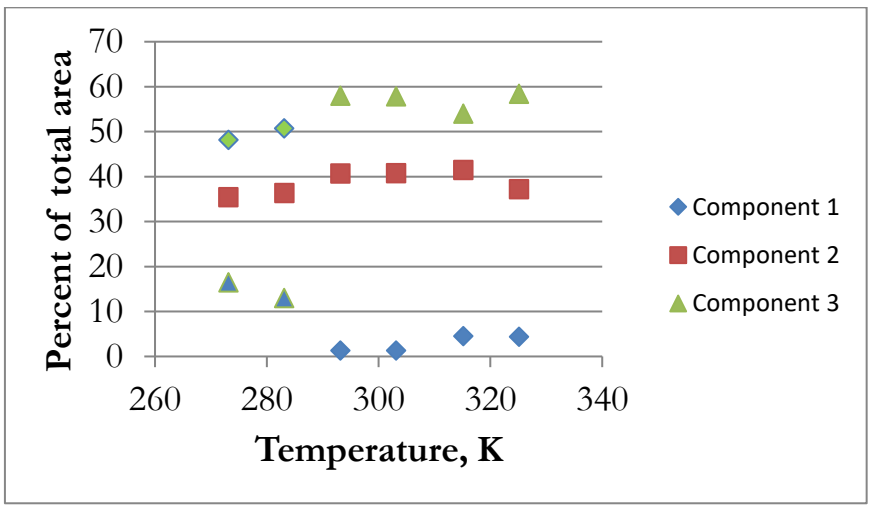

Figure 63 Percent of areal under the peak as a function of temperature

As it can be seen from Figure 63, 3 components are observed at lower temperatures while above 300 K basically only 2 components were fitted, the third one almost disappearing. Similar to the results obtained for the T1 measurements of Li, the fitting results show that there is more than 1 population.

5.1.7.2 Mobility model

On the basis of analysis NMR spectra, we can conclude that there are at least three environments for Li ions which are schematically illustrated in Figure 64.

Figure 64 Model for layer distribution in the $LiBH_4$-SiO_2 electrolyte: orange color is representing the core region (silica regions), blue is representing the interface between $LiBH_4$ and silica and purple is the $LiBH_4$

Following areas are represented in the model for $LiBH_4$ - SiO_2 electrolyte:

- **Layer 1 (orange):** $LiBH_4$ at the interphase with SiO_2. This layer is likely the observed "fast" component in the ^7Li spectra.
- **Layer 2 (blue):** Interphase between "fast" Li at silica surface and "slow" lithium
- **Layer 3 (purple):** is the "slow" population seen in the ^7Li measurements. This population is similar in properties to bulk $LiBH_4$

On the basis of this model and obtained values for areas under the peaks for Li populations, we have calculated layer thickness of the "fast" Li population. The results for different wt% of silica are shown in Figure 65.

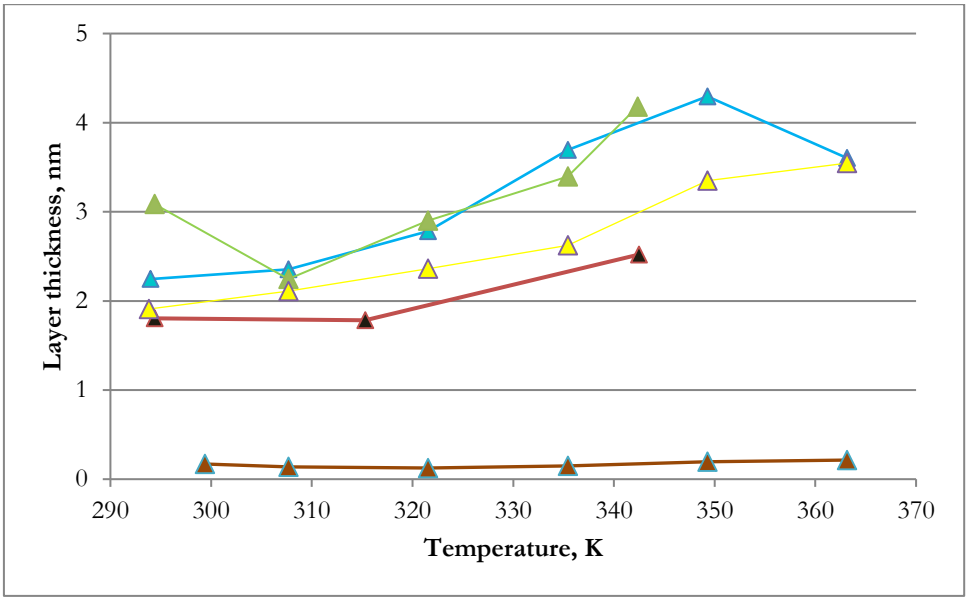

Figure 65 Calculated thickness of highly conductive Li ion layer: Green 50%, Blue 30%, Yellow 20%, Brown 10% $LiBH_4$

As it can be seen from Figure 65, highest layer thickness was calculated for the 30 wt% composite (2-4 nm). The thickness of the $LiBH_4$ layer on top of the SiO_2 particles was calculated (Choi, et al.)[53] In their calculations, they obtained a value of 1 nm at various temperatures and different loadings of silica. We assume that the thicknesses of the layers will vary with temperature as there occur exchange between the two populations as shown from EXSY measurements and therefore variable thickness should be included in the model. It also follows that the optimal composition for $LiBH_4$-SiO_2 is around 30-40%, which seems to be optimal to create an even layer of $LiBH_4$ on SiO_2 particles. When taking the size of the areas under the peak into consideration, then is it reasonable to assume that below 10 wt% of $LiBH_4$, the volume of $LiBH_4$ is under the percolation threshold, as $LiBH_4$ particle are too far away to allow Li ion motion. At the same time for loadings with 50 wt% $LiBH_4$, the area of silica particles is not sufficient to create an interface with $LiBH_4$. For that reason, optimal weight ration lies in range 20-40% percent, as it both allows Li ion diffusion in the percolation network and sufficient area of silica particles that provide interface necessary for creating B-O bonds with $LiBH_4$.

5.1.8 Conclusions on $LiBH_4$-SiO_2 solid-state electrolyte

The $LiBH_4$-SiO_2 is a promising material for solid-state lithium-sulfur batteries. $LiBH_4$-SiO_2 composites have higher Li ion conductivity compared to pure $LiBH_4$ and no significant drop of conductivity is observed for composites with lower loadings of $LiBH_4$. While XRD

measurements showed no new phases formed for composites, NMR and Raman measurements show that behavior of composites is clearly different from the one observed for the bulk.

Our assumption is that after mixing, Li ions that are found in interface at the silica particles are involved in formation of $SiO\text{-}BH_3$ bonds which pas a positive effect in Li ion conductivity. This population is clearly seen in NMR results as sharp Lorentzian peaks. The rest of $LiBH_4$ that is not in contact with silica particle exhibits behavior similar to the one of bulk $LiBH_4$ with slower Li motions seen as Gaussian peaks in 7Li NMR.

The thickness of the formed "fast" Li ion layer was calculated to be in nanometer range, which is in good agreement with previously published results. [53] As layer thickness depends on hydroxylation of the surface f silica particles, as there are participating in the formation of B-O bonds between $LiBH_4$ and silica, a way to improve conductivity and increase "fast" layer thickness would be by surface modifications of silica particles to improve number of OH groups available for bonding with boron. An important aspect of electrolyte preparation is also drying of silica and from the TCA and Zhuravlev model, the optimal drying temperature for silica would be 463 K

5.2 LiBH4-LiBF4 electrolyte

As it has been shown in the previous chapters, $LiBH_4$-SiO_2 solid-state electrolyte exhibits higher ionic conductivity than pure $LiBH_4$ because of the existence of an interfacial layer having higher ionic mobilities than bulk $LiBH_4$. Instead of creating this interfacial layer a second approach was used, to increase the bulk conductivity by modifying the crystal structure of $LiBH_4$. The possibility to form solid solution with $LiBF_4$ has been studied. Since BF_4^- anions have larger diameter than BH_4^- modification of the LiBH4 cell parameters or even stabilization of the high temperature phase could be obtained with some benefit on the ionic conductivity.

The first part of this study was to examine the composition of the electrolytes synthesized with different $LiBH_4/LiBF_4$ ratio and to measure their conductivities. The first conductivity and XRD results presented herein are extracted from measurements carried out by Giovanni Crivellaro during his master thesis at DTU Energy. [104]

5.2.1 Conductivity of $LiBH_4$-$LiBF_4$ solid state electrolyte

Conductivity measurements have been carried out on $LiBH_4$-$LiBF_4$ pellets. the results, for a series with composition 5 to 35 wt% $LiBF_4$ are shown as Arrhenius plots in Figure 66.

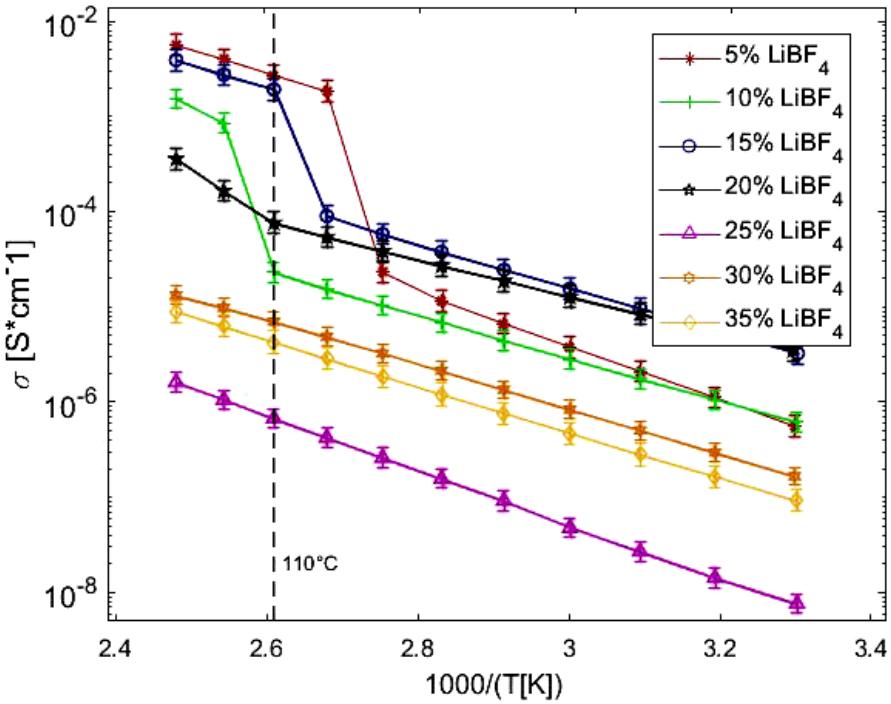

Figure 66 Arrhenius plots of Li^+ conductivity for different ratios of $LiBF_4$ in $LiBH_4$-$LiBF_4$ composites. The data was obtained by Crivellaro (Crivellaro, 2018[104])

As it can be seen in Figure 66, the 5 to 20 wt% compositions show a significant conductivity drop at 110 ˚C (383 K), similar to pure $LiBH_4$ for which a drop of conductivity to values in range 10^{-5} to 10^{-6} Scm^{-1} is observed at temperatures below 383 K. The $LiBH_4$-$LiBF_4$ compounds show however larger conductivities than pure $LiBH_4$ but lower than those of $LiBH_4$-SiO_2 composites with conductivities in range 10^{-2} to 10^{-3} below phase transition.

The 25-35 wt% composition do not show the typical LiBH4 phase transition drop in conductivity but their conductivity is much lower compared to the composition with lower weight percent of $LiBF_4$, indicating that while $LiBH_4$ is present in some amount for mixtures with lower wt%, new products with lower conductivities are formed at higher wt%. In order to investigate what crystalline phases might have formed in these compounds, XRD measurements were carried out on $LiBH_4$-$LiBF_4$ samples.

5.2.2 XRD Measurements on $LiBH_4$-$LiBF_4$ solid state electrolyte

Figure 67 shows an example of XRD pattern for the sample with the composition 10 wt% $LiBF_4$- 90 wt% $LiBH_4$. A Rietveld refinement was performed and the following phases identified: $LiBH_4$, LiF and compounds that are commonly seen in decomposition of $LiBH_4$, i.e $Li_2B_{12}H_{12}$ and $Li_2B_{10}H_{10}$. [105106] Those were the only phases observed in the different samples but with the abundance depending on the ratio of the initial constituents.

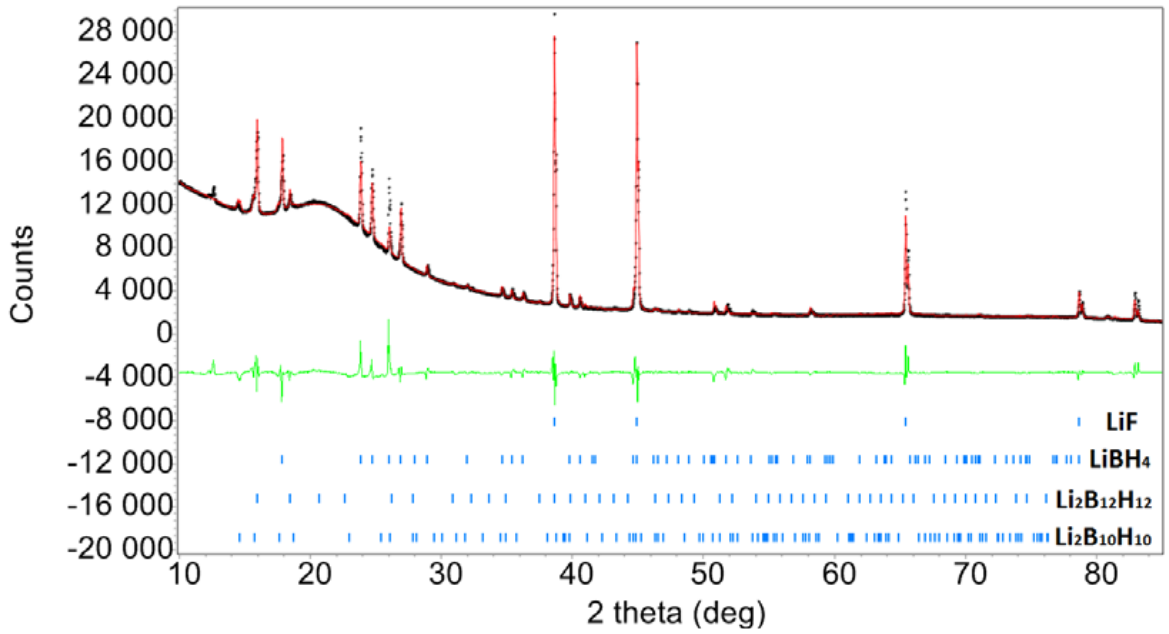

Figure 67 XRD pattern of 10wt% $LiBF_4$-$LiBH_4$ mixture showing LiBH4, LiF and decomposition products. The data was obtained by Crivellaro (Crivellaro, 2018[104])

Figure 68 shows a diagram of the composition of the $LiBH_4$-$LiBF_4$ different ratios obtained from Rietveld refinement of their XRD patterns. It also includes their respective conductivities.

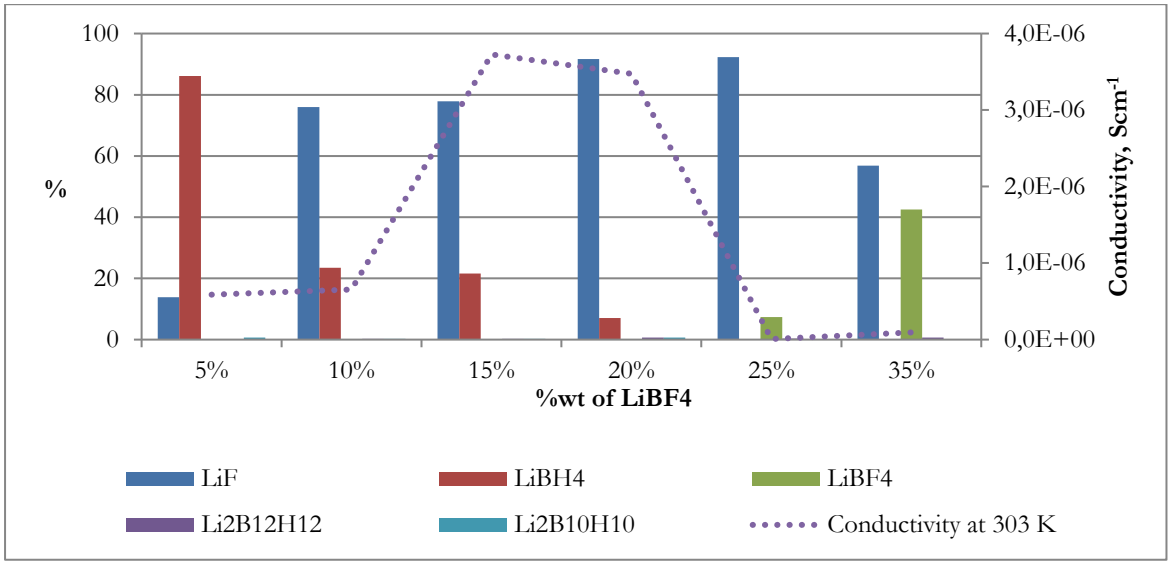

Figure 68 Composition of $LiBH_4$-$LiBF_4$ mixtures obtained from XRD measurements compared to their respective conductivities (purple dotted line). The data was obtained by Crivellaro (Crivellaro, 2018[104])

It is clear from Figure 68 that $LiBH_4$ and $LiBF_4$ react to form different product depending on the initial composition. The final composition has an effect on the conductivity. The reaction can result in two products depending on the wt% of $LiBF_4$:

- **Below 25 wt% of $LiBF_4$:** Lithium borohydride reacts with lithium boroflouride forming lithium borohydride, lithium fluoride and lithium dodecahydrododecaborate $Li_2B_{12}H_{12}$:

$$LiBH_4 + LiBF_4 \rightarrow LiBH_4 + LiF + Li_2B_{12}H_{12} \text{ Eq. 40}$$

  Apart from the three products, there is a forth one that has been observed but not been identified yet from the XRD pattern. A small amount of lithium decahydrodecaborate $Li_2B_{10}H_{10}$ is formed. Both $Li_2B_{10}H_{10}$ and $Li_2B_{12}H_{12}$ are decomposition products of $LiBH_4$.[106]

- **Above 25 wt% of $LiBF_4$:** $LiBH_4$ undergoes full decomposition and the overall reaction can be written as:

$$LiBH_4 + LiBF_4 \rightarrow LiBF_4 + LiF + Li_2B_{12}H_{12} \text{ Eq. 41}$$

It is seen from the reactions above that the expected stabilization of the $LiBH_4$ high temperature or modification of the $LiBH_4$ crystal structure via a solid solution with $LiBF_4$ Did not occur.

However as it is shown in Figure 68, the conductivity of $LiBH_4$-$LiBF_4$ is higher for 15 and 20 wt% samples than the conductivity of pure $LiBH_4$. This indicates that the Li ion mobility is higher for theses composition than for pure LiBH4 and therefore further investigation were performed on the ionic mobilities using, MAS-NMR measurements. NMR Measurements on $LiBH_4$-$LiBF_4$ solid state electrolyte

5.2.3 NMR Measurements on $LiBH_4$-$LiBF_4$ solid state electrolyte

NMR measurements have been performed for the 4 nuclei: ^{1}H, ^{7}Li, ^{11}B and ^{19}F to find their mobility when mixed with $LiBF_4$. As shown from the conductivity measurements, the properties of <25 wt% and >25 wt% samples are different due to different reaction products For that reasons the two sets of results will be treated differently (where a significant difference is seen between the series).

^{7} Li NMR

The lithium resonance does not show significant differences between the sample of composition having weight percentage of $LiBF_4$below or above 25 wt%. In fact, the signals from LiF, $LiBH_4$, $LiBF_4$ and $Li_2B_{12}H_{12}$ overlap in the spectra because of similar shifts: -1.2 ppm, -1.4 ppm, -1.9 ppm and -1.9 ppm respectively It makes it difficult to quantitatively analyze the results of the measurements. . Figure 69 shows single pulse ^{7}Li measurements performed on 5, 10, 20, 30 wt% $LiBF_4$-$LiBH_4$ showing that all products have a central transition in range -1.4 to 1.9 ppm.

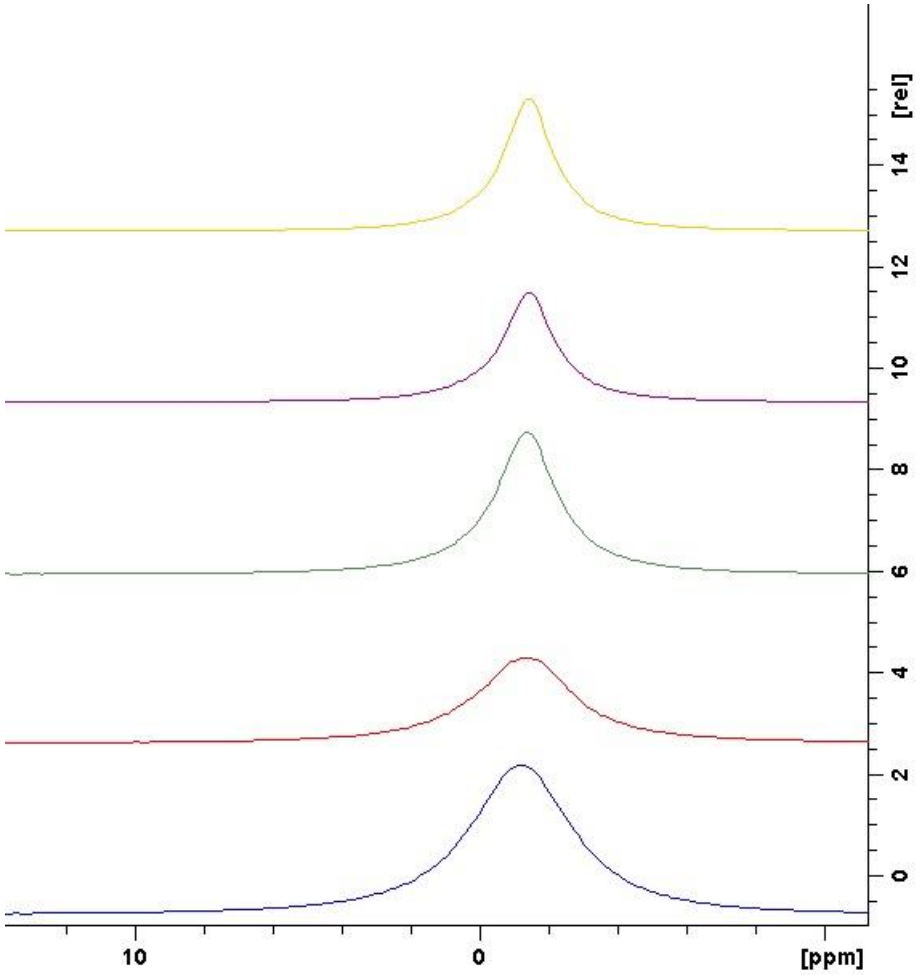

Figure 69: Single pulse 7Li resonance of pure LiF (blue) compared to 30 (red), 20 (green), 10 (purple), 5 (yellow) wt% $LiBF_4$- $LiBH_4$

We know from the XRD results that the following products are formed in the reaction between $LiBH_4$ and $LiBF_4$ below 20 wt% of $LiBF_4$:

$$LiBH_4 + LiF + Li_2B_{12}H_{12}$$

While ^{7}Li NMR spectra for 5, 10, 15 wt% shows a single peak at -1.4 ppm, which can be attributed to pure $LiBH_4$, for 20 wt% sample the peak is broader and two components are observed: one at -1.4 ppm and one at -1.3 ppm. The latter peak is likely to be the contribution from LiF . These results are in good agreement with the XRD results showing a growing amount of LiF and decreasing amount of $LiBH_4$ up to the 35 wt% composition. The results of XRD measurements also showed presence of a fourth phase , however no extra peak appear in the NMR measurements. Could be that this phase does not contain Li or gives peak overlapping with the previous ones.

Single pulse ^{7}Li measurements have been performed on a 20 wt% sample to see if $LiBF_4$-$LiBH_4$ mixtures follow the same trend as $LiBH_4$-SiO_2 where different Li populations are observed. It can be seen from the spectra in Figure 70 that a central transition shows splitting at temperatures around 318 K.

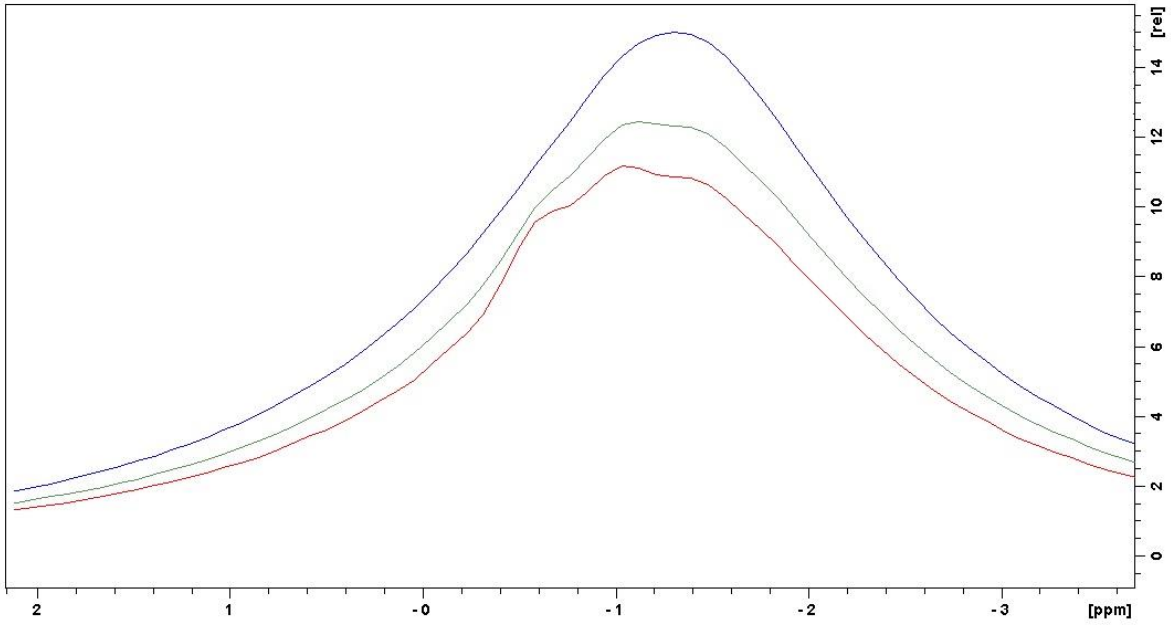

Figure 70 Single pulse 7Li resonance 20 wt% $LiBF_4$- $LiBH_4$ at 293 K (blue), 318 K (green), 323 K (red)

The three peaks appear at -0.6 pm, -1 ppm and -1.4 ppm. The former two peaks have the same shifts as the "fast" lithium ions in $LiBF_4$-$LiBH_4$, which explains higher conductivity values compared to pure $LiBH_4$. "Fast" lithium ions are indeed present in $LiBF_4$-$LiBH_4$, which proves similarities in Li ion motions with $LiBH_4$-SiO_2, however this "fast" population is appearing at higher temperatures compared to $LiBH_4$-SiO_2 meaning that the activation energy barrier is higher for $LiBF_4$-$LiBH_4$.

For the samples with initial $LiBF_4$ contents >25 wt% it is expected from the results of the XRD measurements that the following products will be formed:

$$LiBF_4 + LiF + Li_2B_{12}H_{12}$$

As it can be seen in Figure 69, the spectrum of the 30 wt% sample is broader and is clearly shifted towards -2 ppm due to a contribution from $LiBF_4$. The spectra of 30 and 35 wt% samples that can be found in Figure A 2 in Appendix show overlapping peaks at -0.9 ppm, -1.4 ppm and -2 ppm. The two former peaks were compared to peaks in $LiBH_4$-SiO_2 to study where

the new peaks could be the "fast" lithium ions. Figure 71 shows an example of single pulse Li resonance for 30 wt% $LiBF_4$-$LiBH_4$ (blue) at 293 K compared to 30/70 wt% $LiBH_4$-SiO_2 composites at 293 K (red), 303 K (green) and 313 (purple) (left) and spectra of 30 wt% $LiBF_4$-$LiBH_4$ with increasing temperature (right, top to bottom: 293, 312, 348 and 353 K) on the right.

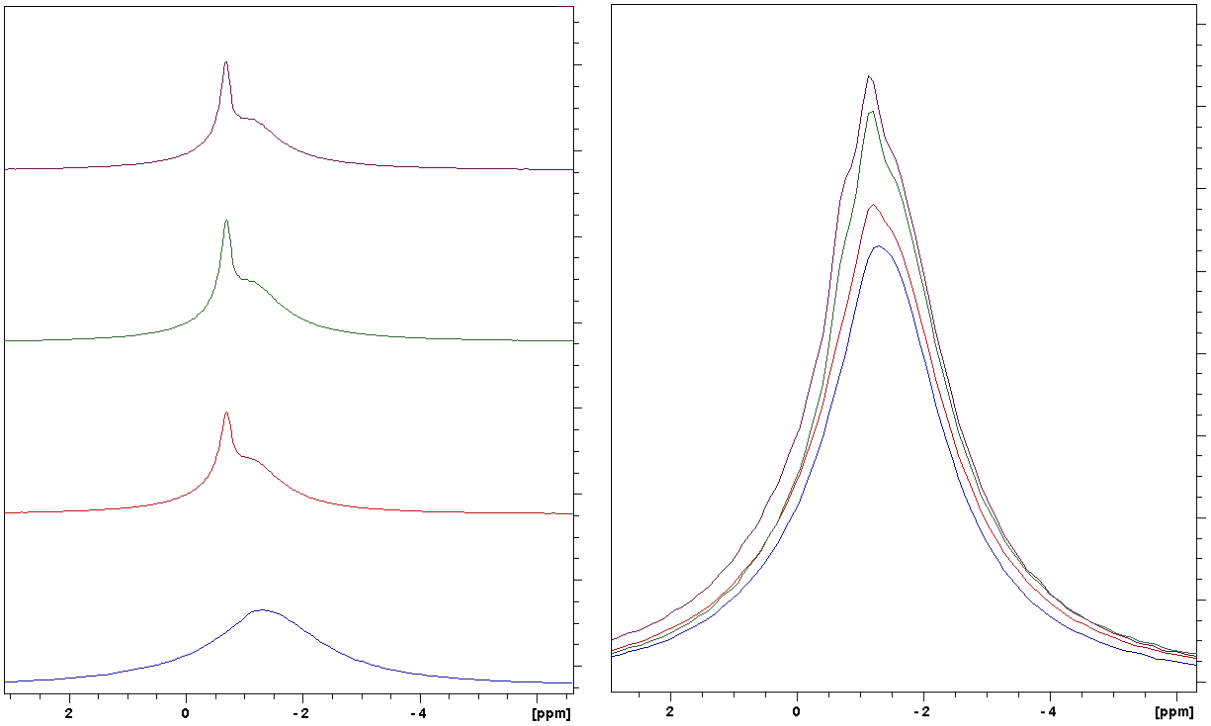

Figure 71 Left: Single pulse ^{7}Li resonance of 30 wt% $LiBF_4$- $LiBH_4$ (blue) compared to 30/70 wt% $LiBH_4$-SiO_2 composites at 293 K (red), 303 K (green) and 313 (purple)
Right: Single pulse ^{7}Li resonance of 30 wt% $LiBF_4$- $LiBH_4$ (blue) with increasing temperature (right, top to bottom: 293, 312, 348 and 353 K).

Clearly, lithium resonance for 30 wt% $LiBF_4$-$LiBH_4$ is broader and does not show a peak splitting that is characteristic for $LiBH_4$-SiO_2 already at room temperature. It can be seen from the spectra in Figure 71, that for $LiBF_4$-$LiBH_4$ the type of Li ion motion is similar to the one of "immobile" resonance in the 30/70 wt% $LiBF_4$-SiO_2 composite, which is the slow motion associated with pure $LiBH_4$. When taking FWHM into consideration both peaks are observed at -1.4 ppm. The mobile component in $LiBH_4$-SiO_2 was previously observed at -0.68 ppm which is likely to be the same trend in $LiBF_4$-$LiBH_4$ where a -0.9 ppm peak is becoming more clear with increased temperatures. However the "fast ions" do not appear as mobile in $LiBF_4$-$LiBH_4$ compared to $LiBF_4$-SiO_2 which are already seen at room temperature.

^{11}B NMR

As it was shown in section 5.2.2, lithium decahydrodecaborate and dodecahydrododecaborate are expected to be formed when $LiBH_4$ and $LiBF_4$ react which is causing changes in the boron environment and new peaks are expected in the boron spectra.

Figure A 3 in Appendix shows ^{11}B high-power decoupling spectra of 30/70 wt% $LiBH_4$-$LiBF_4$ (blue) compared to 30/70 wt% $LiBH_4$-SiO_2 composite (red) at 293 K. A close-up on the spectra is shown Figure 72. It should be noted that the broad peak between -70 and 50 ppm, presents in all the measurements originates from boron in the rotor walls and not from the samples.

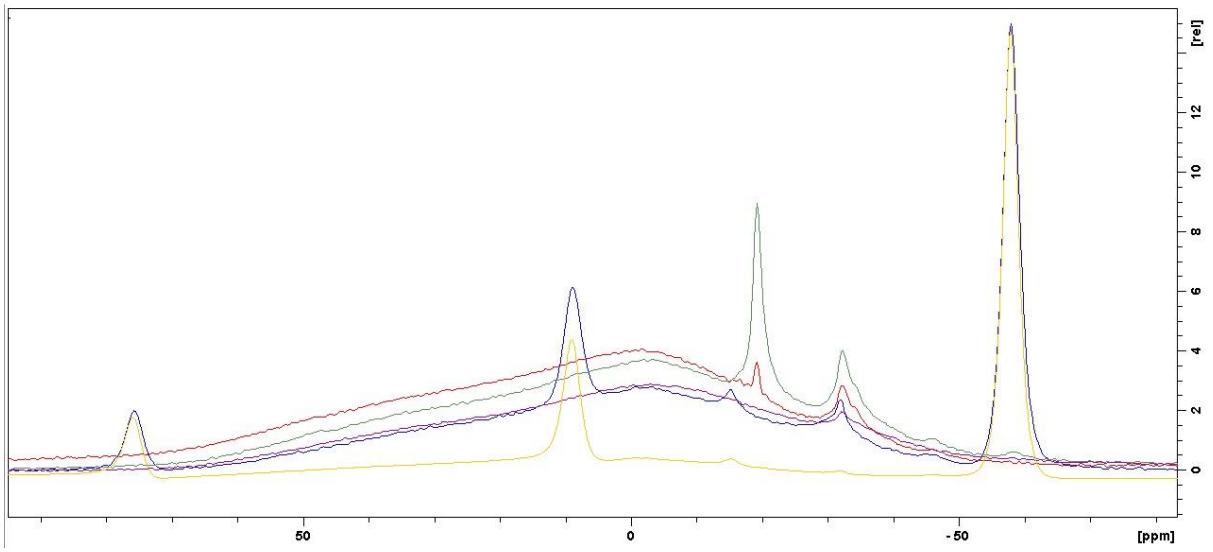

Figure 72 11B High-power decoupling spectra 5 (yellow), 20 (blue), 30 (red), 35 (green) wt% $LiBF_4$-$LiBH_4$ compared to pure $Li_2B_{12}H_{12}$ (purple)

As it can be seen from the Figure 72, the spectra of 5 and 20 wt% samples are identical and have same peaks as $LiBH_4$-SiO_2. except for two new peaks at -15.3 ppm and -31.1 ppm. Similarly, for $LiBF_4$-$LiBH_4$ above 25 wt% of $LiBF_4$, a new peak appears at -19.3 ppm which is due to contribution from pure $LiBF_4$; and a peak at -31.1 ppm that is coming from lithium dodecahydrododecaborate.

The unaccounted peak at -15.3 ppm for <20 wt% $LiBH_4$-$LiBF_4$ sample could be the result of decomposition of $LiBH_4$ or alternatively coming from new compounds that are formed in the reaction between $LiBH_4$ and $LiBF_4$.

There are two suggested mechanisms for decomposition of $LiBH_4$ which depend on the back pressure and heating ramp. One includes $Li_2B_{12}H_{12}$ (in some cases has $Li_2B_{10}H_{10}$ been observed)

as intermediate and the other the formation B_2H_6. [106] The final products of decomposition will be either lithium decahydrodecaborate or dodecahydrododecaborate depending on temperature of decomposition following one of the two reactions:

- At 150°C (in presence of 5/2 B_2H_6):

$$LiBH_4 \rightarrow \frac{13}{2}H_2 + \frac{1}{2}Li_2B_{12}H_{12}$$

- At 200°C (in presence of 2 B_2H_6):

$$LiBH_4 \rightarrow \frac{13}{2}H_2 + \frac{1}{2}Li_2B_{10}H_{10}$$

It is likely that for 5-20 wt%, the peak at -15.3 ppm originates from $Li_2B_{12}H_{12}$ which is seen from the XRD measurements by inspecting the areas under the peak for the two components.

From the NMR studies on the boron species, one can conclude that the starting products ($LiBH_4$ and $LiBF_4$) are identified in the spectra together with the decomposition products of $LiBH_4$ (lithium decahydrodecaborate or dodecahydrododecaborate). No new compounds containing boron are observed and the forth component in the reaction between $LiBH_4$ and $LiBF_4$ is not likely a compound containing boron.

^{1}H NMR

Proton resonance was recorded for the 5 to 35 wt% samples. It should be noted, that the spectra in this chapter has not been referenced in the same way as for the spectra of $LiBH_4$-SiO_2 in Section 5.1.7.1 because of the absence of suitable reference standard. Therefore, the shifts are reported relative to the central transition.

For the <25% $LiBF_4$ samples, the major product containing protons is $LiBH_4$, therefore it was expected that the spectra of composites would be similar to pure lithium borohydride. Single pulse proton spectra of 5-20 wt% $LiBF_4$ - $LiBH_4$ samples was recorded and compared to pure $LiBH_4$ at 293 K in Figure 73.

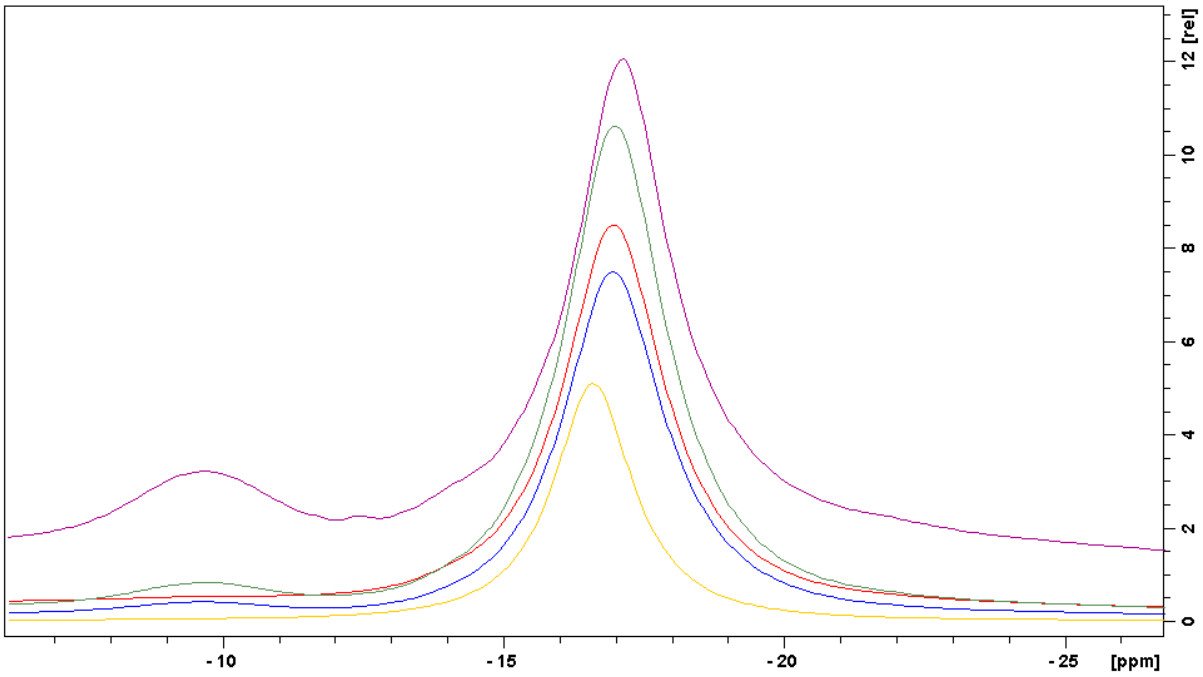

Figure 73 Single-pulse proton resonance of LiBH4 (yellow) compared to $LiBH_4$-$LiBF_4$ (blue 5%, red 10%, green 15% and purple wt 20% $LiBF_4$) at 293 K

Apart from the main peak, that are similar for all wt%, a new peak can be seen in the spectra of the composites especially pronounced in the proton resonance of the 20 wt % $LiBF_4$ samples. These peaks at around -4.5 ppm relative to the central transition have been previously attributed to hydrogen trapped in solid medium as the result of decomposition of $LiBH_4$[107]. As it has been pointed out in the previous section, hydrogen and lithium decahydrodecaborate or dodecahydrododecaborate are the products of decomposition of $LiBH_4$ and the area under the peak -4.5 ppm relative to central transition is increasing as the percent of $Li_2B_{12}H_{12}$ and $Li_2B_{10}H_{10}$ are increasing thus the new peak is likely coming from hydrogen formed during the decomposition process of lithium borohydride.

For the >25 wt% $LiBF_4$ samples, pure lithium borohydride is not among the products and the spectra are expected to be dominated by the decomposition products. Figure 74 shows single-pulse proton resonance in 30 wt% $LiBH_4$-$LiBF_4$ (red) sample compared to 30/70 wt% $LiBH_4$-SiO_2 (blue) composite at room temperature (left) and proton resonance for 30 wt% $LiBH_4$-$LiBF_4$ sample at 293 K (red), 312 K (green), 348 K (purple) and 353 K (blue).

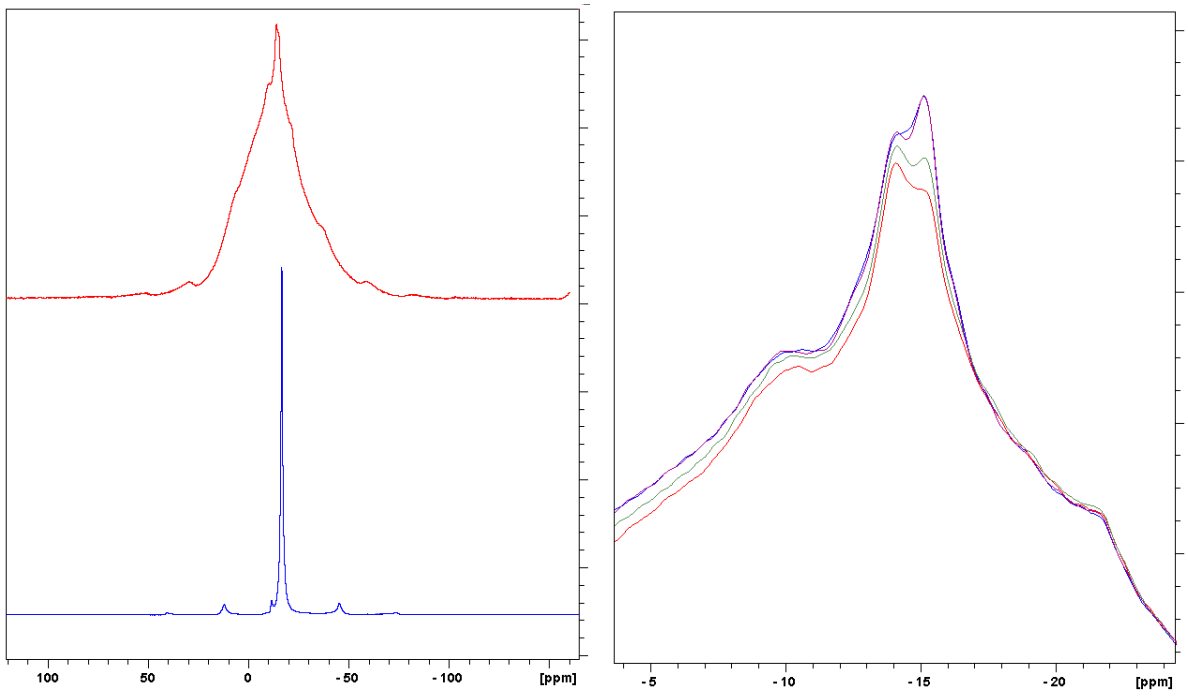

Figure 74 Left: Single-pulse proton resonance of 30 wt% $LiBH_4$-$LiBF_4$ (red) compared to 30/70 wt% $LiBH_4$-SiO_2 composite (blue) at 293 K. Right: Single-pulse proton resonance of 30wt% $LiBH_4$-$LiBF_4$ sample at 293 K (red), 312 K (green), 348 K (purple) and 353 K (blue)

It can be seen from Figure 74 that the spectra of $LiBH_4$-$LiBF_4$ is a combination of several peaks which are much broader than the central transition in $LiBH_4$-SiO_2. For 30 wt% $LiBH_4$-$LiBF_4$ while the full width at half maximum remain identical, there is an increasing shift with temperature in the central transition. This indicates that the motion of the protons is not as temperature dependent as the motions of the Li ions where a significant line narrowing was observed with increasing temperature.

Hydrogen populations in $LiBH_4$-$LiBF_4$ and $LiBH_4$-SiO_2 are clearly different which was expected as $LiBH_4$ is no longer present after the reaction. Figure 75 is showing proton resonance of 25 wt% $LiBH_4$-$LiBF_4$ (blue) compared to pure $Li_2B_{12}H_{12}$.

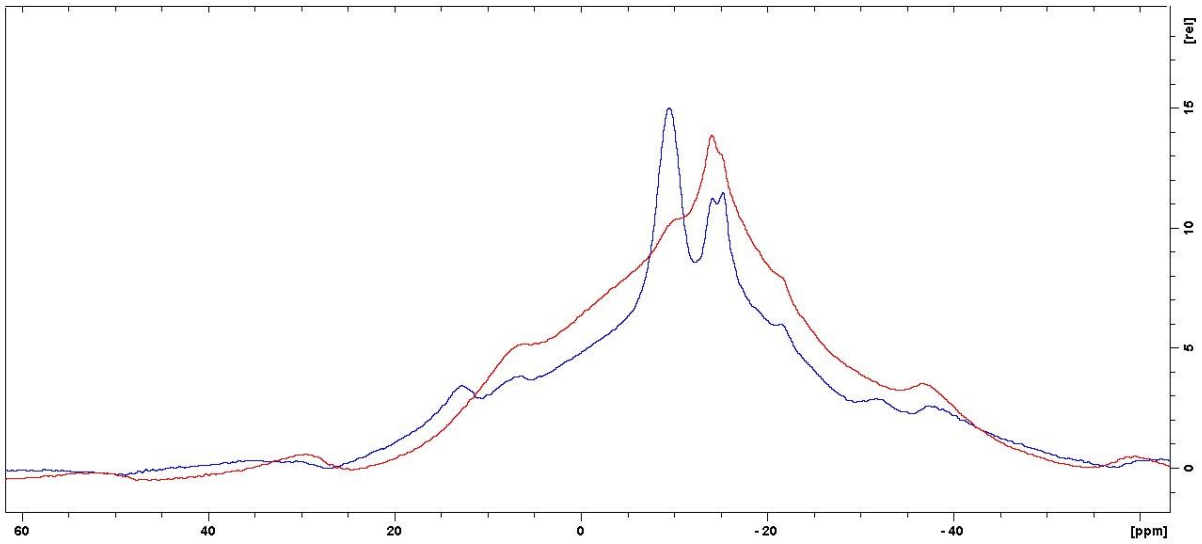

Figure 75 Single-pulse proton resonance of 25 wt% $LiBH_4$-$LiBF_4$ (blue) compared to pure $Li_2B_{12}H_{12}$

The spectrum for 25 wt% $LiBH_4$-$LiBF_4$ (blue) has clearly a contribution from $Li_2B_{12}H_{12}$ together with peaks coming from another compound. This compound is likely to be $Li_2B_{10}H_{10}$ which has a similar proton environment. The conclusion of the proton study is that no new proton environments apart from the expected products were observed for both <25 and >25 wt% samples.

^{19}F

The spectra of <25% $LiBF_4$ samples was expected to be containing LiF which is the only fluorine containing product, however the results of measurements showed that a new compound different from LiF and $LiBF_4$ was formed in the reaction.

Figure 76 shows 19F spectra of pure $LiBF_4$ compared to 20 wt% $LiBF_4$ – $LiBH_4$. The spectra were referenced against 19F signal of pure $LiBF_4$. Negative intensities in the phasing of $LiBF_4$ – $LiBH_4$ composite come from the background in the probe and are not related to the sample.

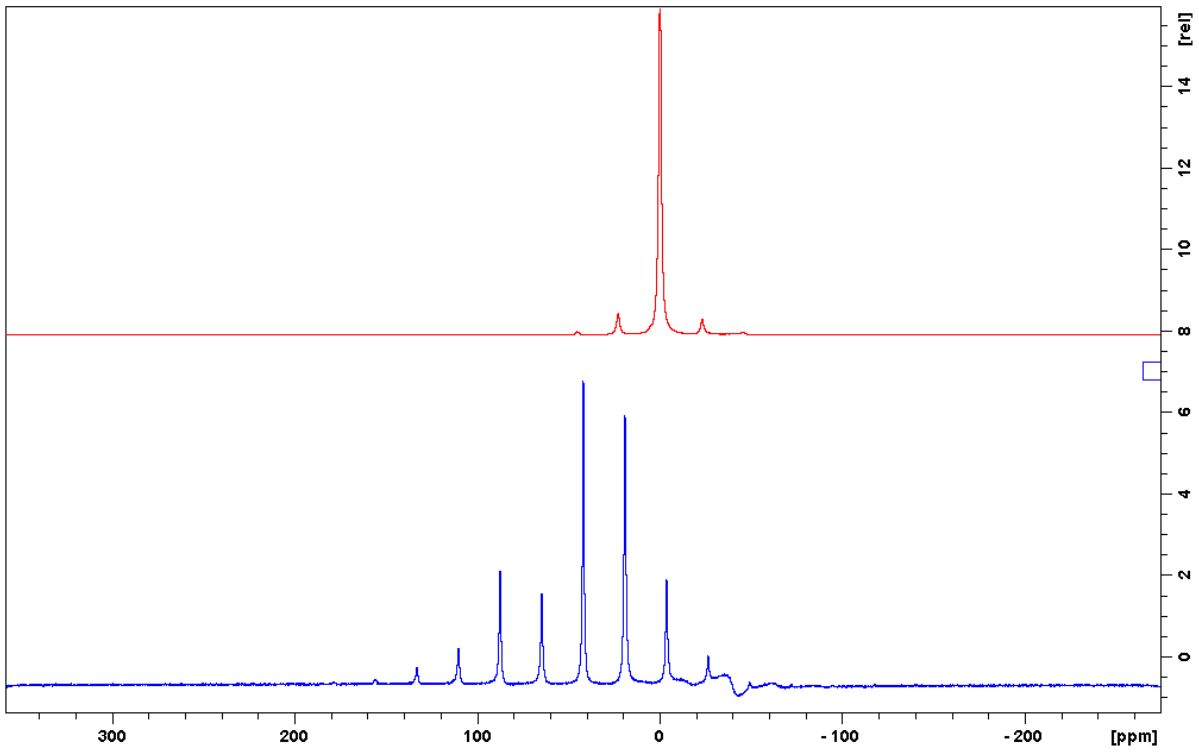

Figure 76 19F spectra of 20 wt% $LiBH_4$-$LiBF_4$ (blue) compared to pure $LiBF_4$ (red) at 293 K

As it can be seen from the Figure 76, the 19F spectra of the composite has a number of additional peaks compared to pure $LiBF_4$ which indicates that the environment of 19F nuclei has changed after the reaction with $LiBH_4$. The spectrum of composite shows chemical shift anisotropy (CSA) which indicates a much less symmetrical environment of 19F nuclei compared to isotropic shift in pure $LiBF_4$. The spectra of composite compared to pure $LiBF_4$ and LiF can be found in Figure A 4 in the Appendix. From these spectra it can be concluded that the composite is clearly different from $LiBF_4$, however a small percentage of LiF cannot be excluded due to overlap in peaks. This could be the fourth compound formed in the reaction between $LiBH_4$-$LiBF_4$.

For samples above 25 wt% of $LiBF_4$, the spectra look much different than those of lower loadings. Figure 77 shows ^{19}F spectrum of 25 wt% $LiBH_4$-$LiBF_4$ compared to spectra of pure LiF and $LiBF_4$. It can be seen from the spectra of the products that both the peaks from LiF and $LiBF_4$ are present and this is very different from the 20 wt% $LiBF_4$ – $LiBH_4$ sample where a new compound was formed while only little contribution from LiF was observed. This confirms the assumption that the only fluorine-containing products formed in the reaction $LiBH_4$ and $LiBF_4$ with more than 25 wt% of $LiBF_4$ are LiF and $LiBF_4$.

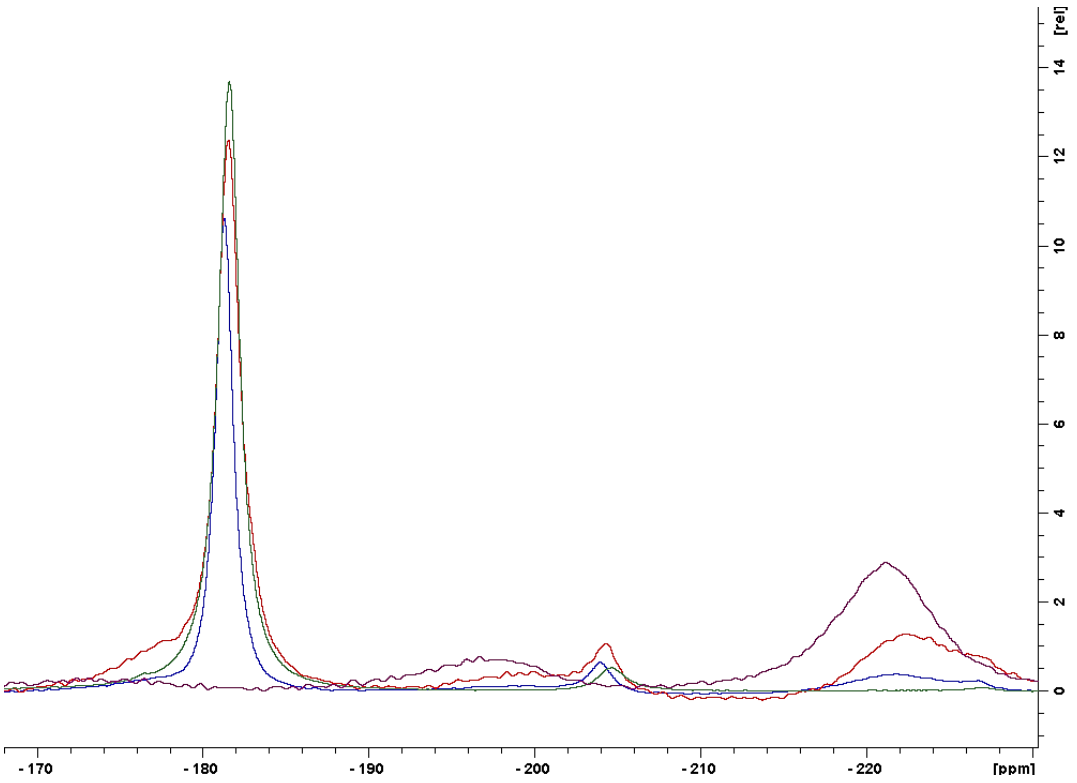

Figure 77 19F spectrum for 25 wt% $LiBH_4$-$LiBF_4$ at 299K (red) and 240 K (blue) compared to pure LiF (purple) and pure LiBF4 (green)

The spectra of the composites at two temperatures shows that there is a shift in central transition, which indicate that environment for ^{19}F nuclei has changed. However the overall spectra does not show new peaks which was seen for the 20% sample.

The results of the ^{19}F measurements show that a new fluorine compound was formed at lower wt% of $LiBF_4$, however it is not possible to say what compound is formed. A DFT study could give additional information on the origin of the new compound and the mechanism of the reaction between $LiBH_4$ and $LiBF_4$ that appears to be more complicated than originally thought.

5.2.4 Conclusions on $LiBF_4$- $LiBH_4$ electrolyte

In this part of the work, we have studied $LiBH_4$/ $LiBF_4$ mixtures with different loadings of $LiBF_4$ (5, 15, 10, 20, 25, 30, 35 wt %) to understand the reaction mechanism between the two components. The conductivity results show that while 5-20 wt% mixtures are better ionic conductors than pure $LiBH_4$, the values are lower than those of $LiBH_4$-SiO_2 composites. The conductivities of $LiBH_4$-$LiBF_4$ mixtures with higher loadings (>25 wt%) of $LiBF_4$ show conductivities lower than pure $LiBH_4$ due to higher content of $LiBF_4$ that has lower ionic conductivity. The XRD measurements show that $LiBH_4$ and $LiBF_4$ react instead of forming a solid state solution as it was expected similar to lithium hallides s and lithium borohydrides solid solutions. At lower loadings of $LiBF_4$, the reaction between $LiBH_4$ and $LiBF_4$ leads to decomposition of $LiBH_4$ and formation of decomposition products (lithium decahydrodecaborate or dodecahydrododecaborate and likely hydrogen) and LiF, furthermore an unknown fluorine compound is formed. This compound appears to have a positive contribution to conductivity as a raise in conductivity was observed for these products. For higher loadings (>25 wt%), the products show a major contribution from $LiBF_4$ which was expected both from XRD and conductivity measurements.

Overall, the compounds obtained from the reaction of $LiBH_4$ with$LiBF_4$ are not as a good electrolyte than $LiBH_4$-SiO_2 because of the existence of low conductivity compounds in the produtcs. While lower loadings of $LiBH_4$-$LiBF_4$ exhibit similar ions mobilities than the $LiBH_4$-SiO_2 composite, the existence of "fast" Li ions is occurring at higher temperature which limits the applications of $LiBH_4$-$LiBF_4$. It has not been possible to identified the actual phase bringing the conductivity and the measurements were performed on mixtures of several components with presumably some non-conductive. Therefore it could be interesting to identify and isolate the "good" phase(s) to evaluate their conductivity as pure compound.

5.3 Li-S Solid State Battery

Some of the results of battery testing in this chapter have been previously published in Paper I (Lefevr et al, 2018). [97] The sections in chapter provide new and complimentary results that have not been published yet.

5.3.1 Battery Performance

Charge-discharge curves of a Li-S battery are shown in Figure 78 (Adapted from Lefevr, et al[97]). Slight slopes are observed at charge and discharge plateaus which is different compared to flat plateaus of Li-S cells with liquid electrolyte.[108] [109] This suggest the non-homogeneity of the electrochemical reaction, it could illustrates the different reaction steps from S_8 to Li_2S or signifies that is becomes more and more difficult to reach the sulfur particles to perform the conversion reaction. The cell has also shown on average an overvoltage of 0.15 V.

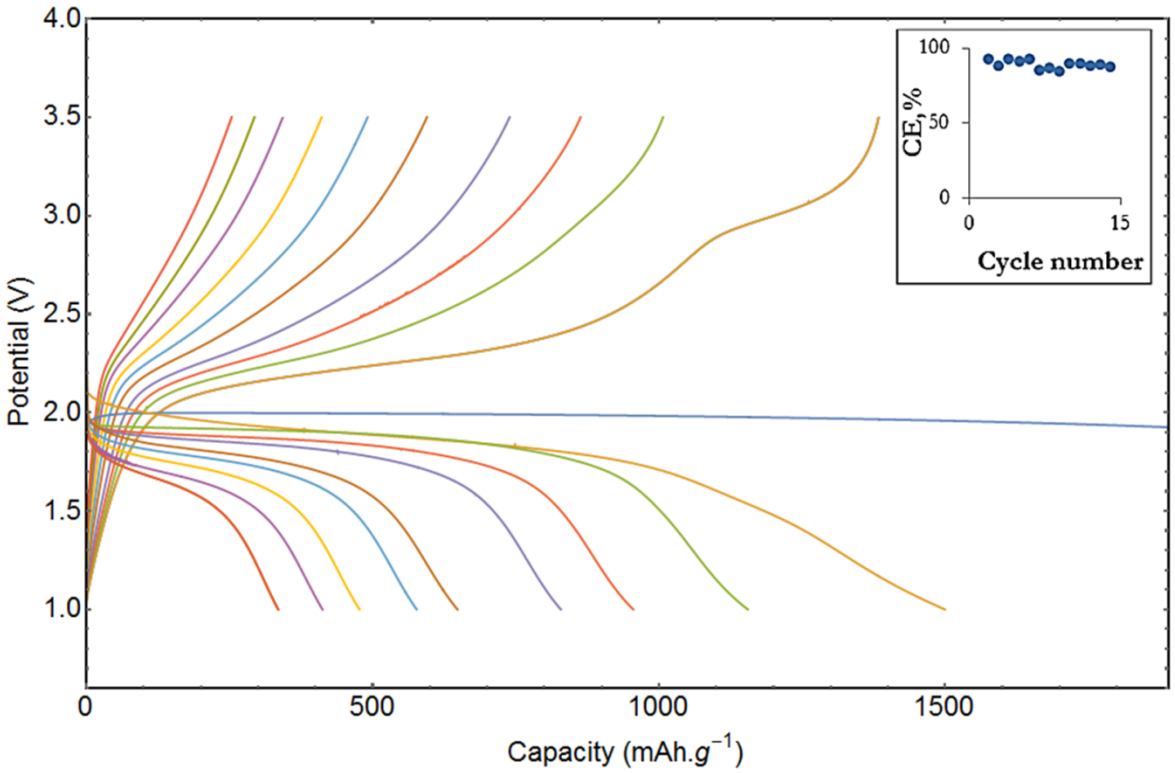

Figure 78 Discharge-charge cycles of a Li-S battery between 1 and 3.5 V (Adapted from Lefevr, et al [97]). The insert shows development of the Coulombic efficiency (CE) as a function of cycle number. The cell was cycled at 0.03 C and 328 K

As it can be seen from the figure, the first discharge and charge show larger capacity than the theoretical value for sulfur (3600 versus 1675 mAh g^{-1} sulfur), furthermore two voltage plateaus are seen (2.3 V and 2.1 V) during the first cycle. The high capacity during initial cycle is

consistent with observations of high capacity in Li-S cells using thio-LISICON electrolyte. There, it was assumed to originate from the reaction of lithium with the carbon matrix in the cathode. [110] Similar behavior was also observed for Li-S cells with $LiBH_4$ nanoconfined in MCM-41[111] and $LiBH_4$-LiI solid-state solutions [112] as solid electrolyte. In the latter case, Li_2TiO_3 was used as cathode active material and therefore we can exclude that a reaction with sulfur may lead to this too large cell capacity.

In Figure 78, the capacity reached at the second discharge was around 1500 mAh g^{-1} sulfur which is 90% of the theoretical capacity and 100 times the capacity of Li_2TiO_3 /$LiBH_4$- LiI-/Li cells that were proposed by Sveinsbjornsson.[112] 35.8 % of the capacity reached during the second discharge is found during the firth cycle and on average there is a loss of about 7 % of the capacity after each cycle.

During the first ten cycles, the coulombic efficiency is on average of 88.8%. It shows that the electrochemical reaction occurring in the cell is reversible and based on voltage plateaus that are close to the theoretical values (2.15 V),[113] the possibility of non-reversible reactions from the second and following cycles can be excluded. The decreasing capacity with cycling is more likely to be caused by a loss of contact at the electrolyte and electrode interphase, -because of the large volume changes at the cathode (200% from S to Li_2S). The cell resistivity is found to increase during the cycling. This is described in detail in section 5.3.3 and 5.3.4 below, where the results from EIS are discussed.

Li-S batteries with $LiBH_4$-SiO_2 electrolytes have been charged to higher voltages and show stability at least up to 6V and to see if the electrochemical reaction giving the too high capacity could be reversible, which is shown in Figure 79.

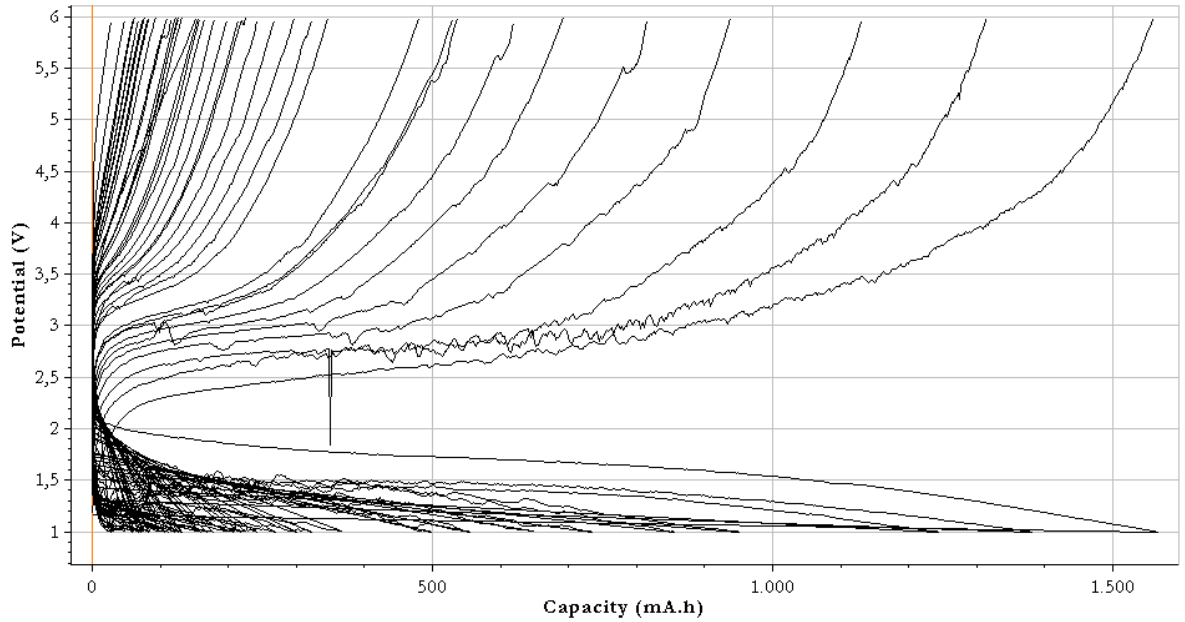

Figure 79 Charge discharge cycling of a Li-S battery between 1 and 6 V

Recorded cyclic voltammetry of a Li-S battery with 30/70wt% $LiBH_4$-SiO_2 is shown in Figure 80.

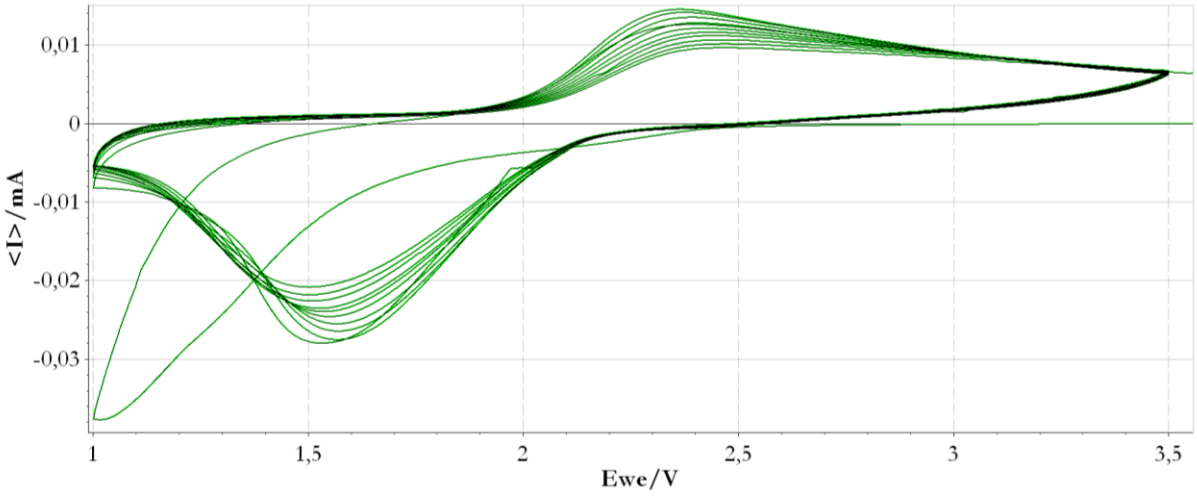

Figure 80 Cyclic voltammogram of a LiS battery with $LiBH_4/SiO_2$ composite

Figure 80 shows a Voltammogram recorded of a Li-S battery made with 30-70 wt% LiBH4-SiO2 electrolyte. Apart from the initial cycle, for second and following cycles of cyclic voltammetry, two peaks are observed at cathodic respectively anodic scans:

- Reduction peak is observed at 1.5 V for the first three cycles and shifting towards 1.6 for following cycles. The peaks can be attributed to formation or low order polysulfides (L_2S_2 and L_2S)
- Oxidation peak is observed at 2.4 V which is due to conversion of polysulfides back to elemental sulfur and lithium.

While the batteries show good cycling ability, the area of the cathodic peak is larger than the area of the anodic peak which is likely due to an increase in internal resistance of the battery during cycling which has been previously reported for Li-S batteries.[111]

5.3.2 Morphology of C+S cathodes

As it was shown in Figure 78, there is a significant drop in capacity between first and second discharge. This drop could be due to following reactions:

- Reaction between $LiBH_4$ and cathode material (carbon matrix, the reaction between $LiBH_4$ and sulfur is unlikely which was discussed in section 5.3.1)
- Formation of a blocking layer on the cathode or anode side due to difficulties of converting Li_2S to high order polysulfides and to elemental sulfur.
- Charge transfer resistance i.e the Li transfer form solid electrolyte to sulfur

The possibility of direct reaction between $LiBH_4$ and carbon matrix have been previously reported in the literature. [110] The second possibility is the formation of interphases on cathode side due to incomplete conversion of lithium sulfide back to elemental sulfur. In order to investigate this, we have cycled a Li-S battery and studied the cathode at different stages of charge/discharge to see if any changed in structure are observed after cycling. Figure 81 shows a sample of a surface of pristine C+S cathode showing uniform coating on the surface and no cracking. The sharp particles in the figure to the left are pieces of elemental sulfur.

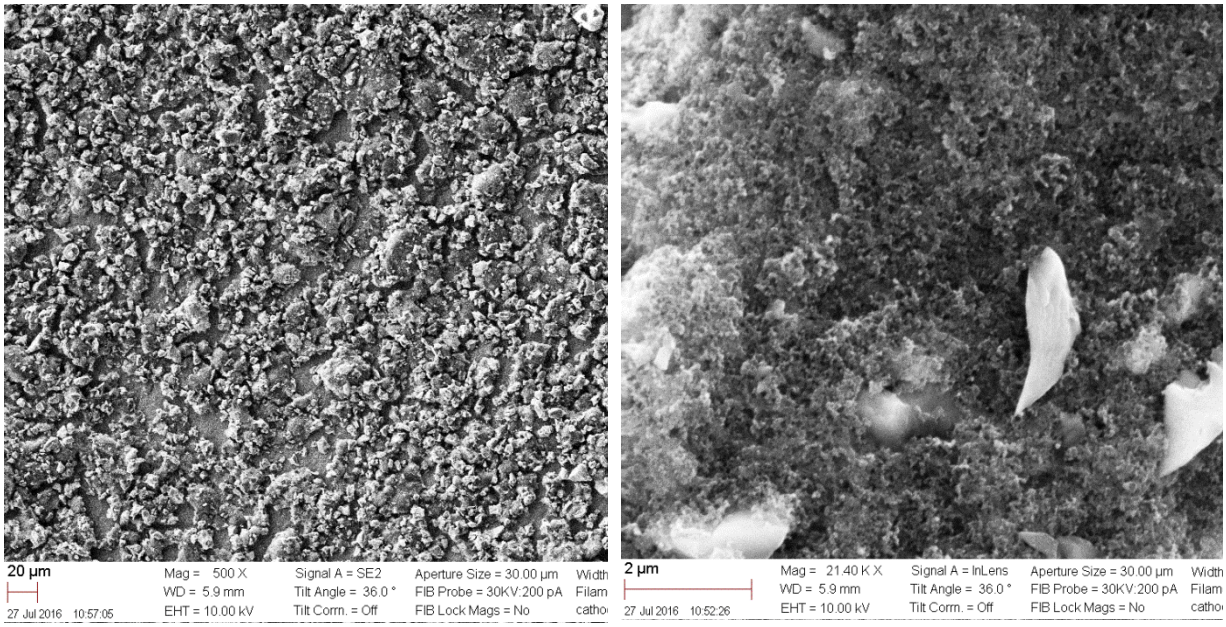

Figure 81. SEM image of a surface of pristine C+S cathode at magnification 50 X (left) and 2140 X (right)and showing carbon layer and sharp particles (elemental sulfur)

Figure 82 shows SEM image of a cross section of a pristine C+S cathode on aluminum support. The thickness of deposited C+S layer on the support was calculated to be 10 µm. As it can be seen from SEM image, the surface of cathode is homogenous.

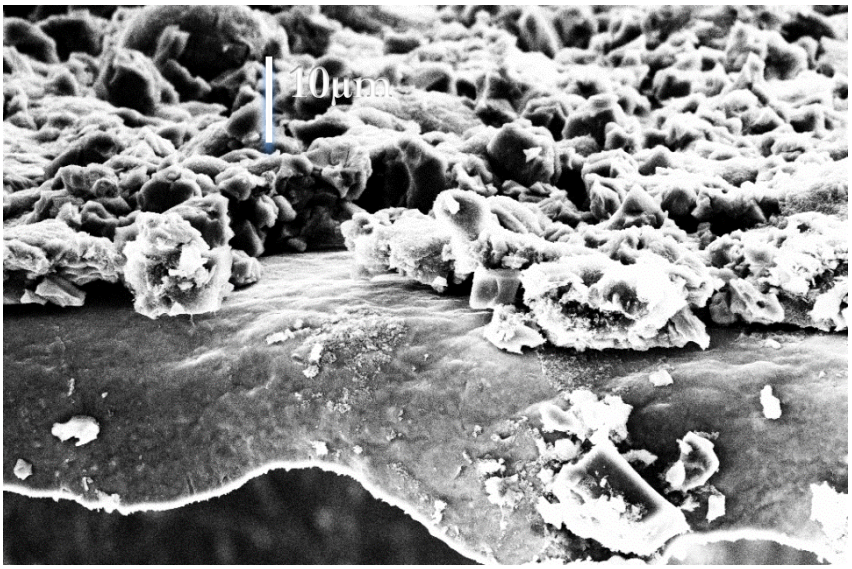

Figure 82. SEM image of a pristine cathode showing Al support and C+S layer on top

AFM images were taken on the surface of cathode showing large height variations which are seen in Figure 83. As it can be seen from Figure 81, the surface shows particles of elemental sulfur in range 2-3 microns also seen on the AFM images.

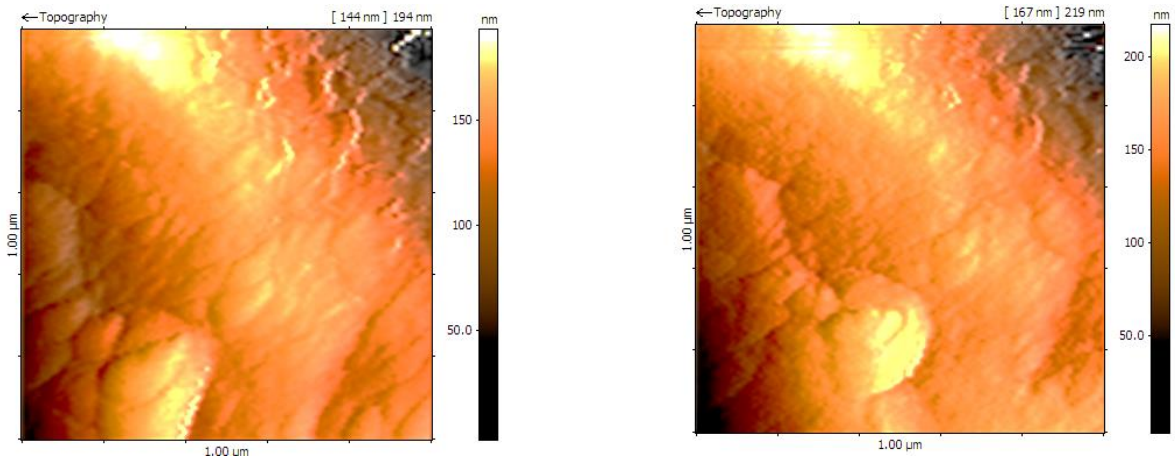

Figure 83 AFM image of C+S cathode surface showing sulfur particles

In order to study the changes in the cathode, a Li-S battery was discharged to 1 V, voltage eat which low order polysulfides are formed. SEM images of the cathode of that battery are shown in Figure 84.

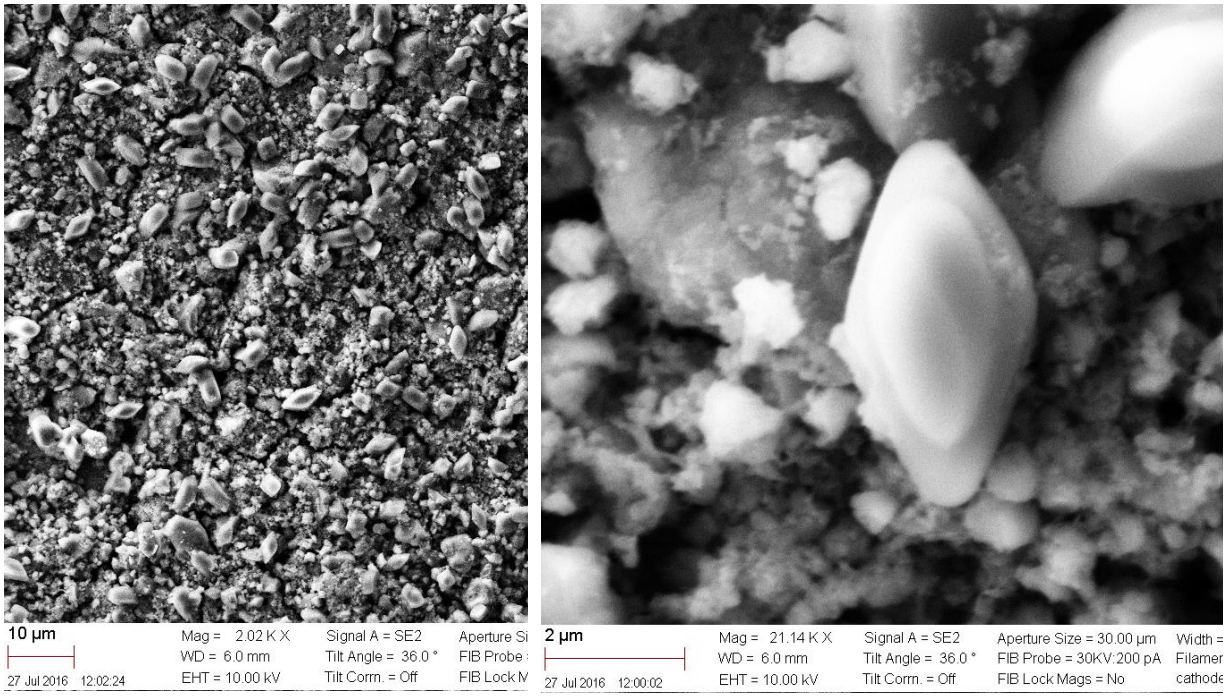

Figure 84 SEM image of C+S cathode after initial discharge to 1 V

As it can be seen from Figure 84, after the initial discharge, rhombus-like grain structures with size 1-3 µm are formed on the surface of electrode. The EDS showed that the sulfur was distributed evenly on the surface, therefor have we decided to perform TEM imaging and synchrotron tomography (for further details see section 5.3.7) on the cathode material to study shape evolution of the formed structures.

TEM imaging was performed on the cathode after first discharge and compared to images of pristine cathode material. Obtained TEM micrographs are shown in Figure 85.

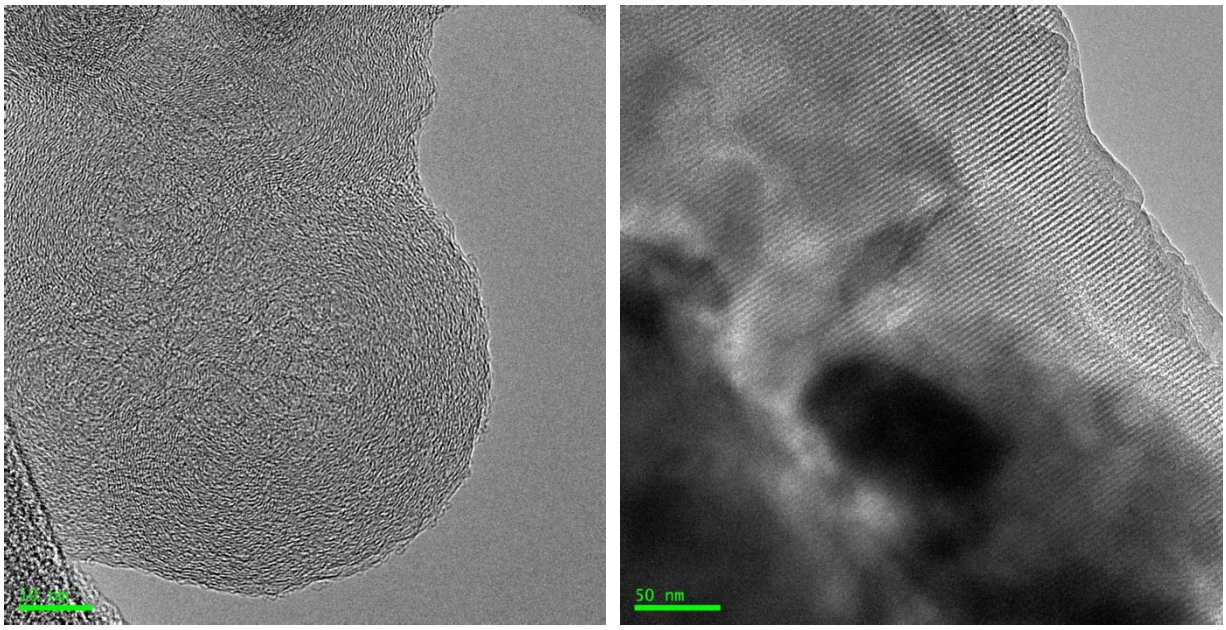

Figure 85 TEM images of cathode material: pristine (left) and after 1 cycle (right)

The images show that for the pure carbon and sulfur the domains are in size range 0.3-0.5 nm while for the cathode material extracted from the battery after 1st discharge, the size of domains were much larger, 2 – 2.5 nm. Furthermore, in the first case the material appears amorphous while it looks more crystalline in the second case. We have not been able to identify the formed substance for the cycled cathode but it is clear that new compounds were formed.

The method has one major limitation, the sample that is used for TEM sample preparation is limited to the amount of particles that can be peeled of pressed cathode. As in a Li-S battery, pressure is applied, making it difficult to separate electrolyte from the cathode. It is also difficult to separate bulk, unreacted sulfur from the bottom of the layer and interfacial layer where the reaction is taking place.

5.3.3 Electrochemical Impedance Measurements

Electrochemical Impedance measurements have been performed on Li-S batteries with $LiBH_4$-SiO_2 electrolyte during charging and discharging. Figure 86 shows the impedance spectra taken on a pristine battery (blue) and after the 6 following discharge/charge cycles. The part of the spectra to the left of the minimum is the contribution from the solid state electrolyte. While a single arc is observed in EIS spectrum, it cannot be excluded that two arcs are overlapping from bulk $LiBH_4$ and the interphase between silica and $LiBH_4$. However, if this is the case, it is not possible to separate the different contributions from the two conductivities on the basis of EIS alone.

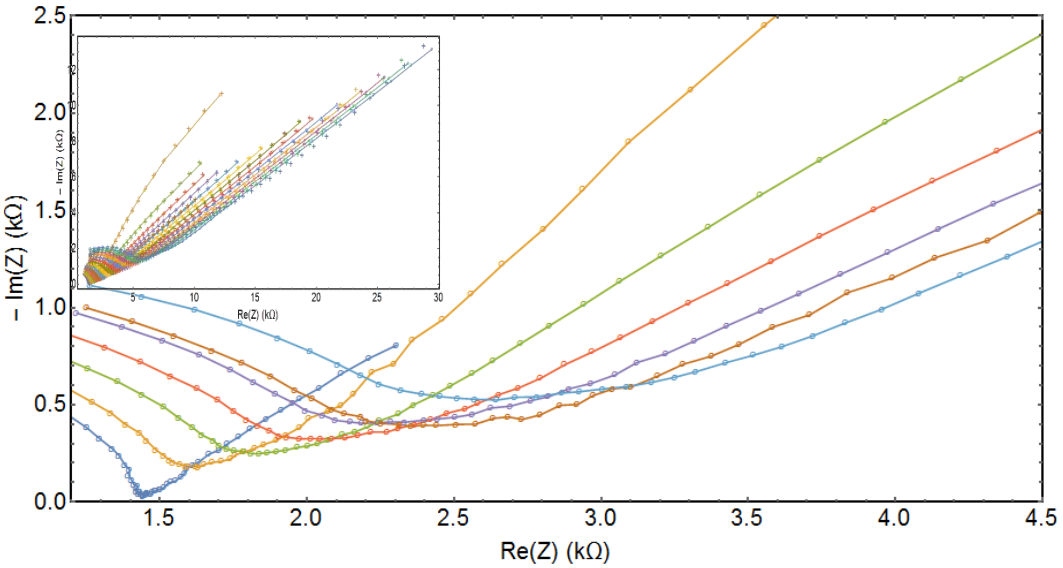

Figure 86 Impedance spectra of a pristine Li-S battery (blue) and after the 6 first discharge-charge cycles – Insert: EIS spectra on the same battery for 14 cycles

The equivalent circuit model that can be used for fitting the spectra of the solid-state Li-S batteries is shown in Figure 87:

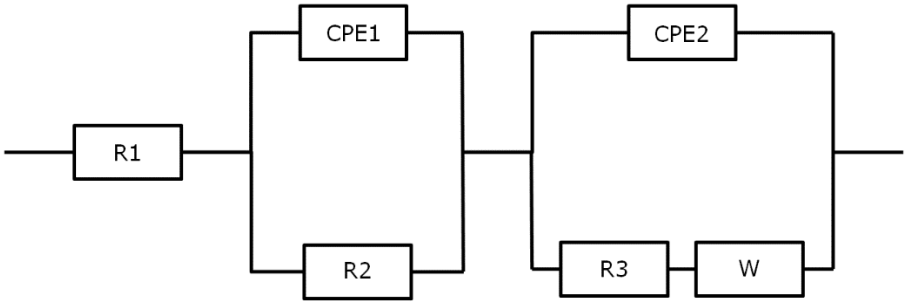

Figure 87 Circuit elements used to model the EIS of the Li-S sold state batteries

In the model shown in Figure 87, R_1 is a resistor to take into account any wire resistance and contact resistance in the circuitry and cells. In principle, R_1 is found to be very small, if not negligible (< 1 mΩ). The parallel elements, R_2 and CPE_1, model the electrolyte as explained earlier, while R_3, W and CPE_2 model the cathode behavior. The CPEs are the constant phase element which are used to model the imperfect capacitance of the electrolyte and the double layer capacitance in the cathode. R_3 would represent the charge transfer at the electrode /electrolyte interface and W, the Warburg element, represents finite-length diffusion of lithium ions in the cathode. Figure 88 shows selected spectra, every five discharge/charge cycles of a Li-S battery using the model shown in Figure 87.

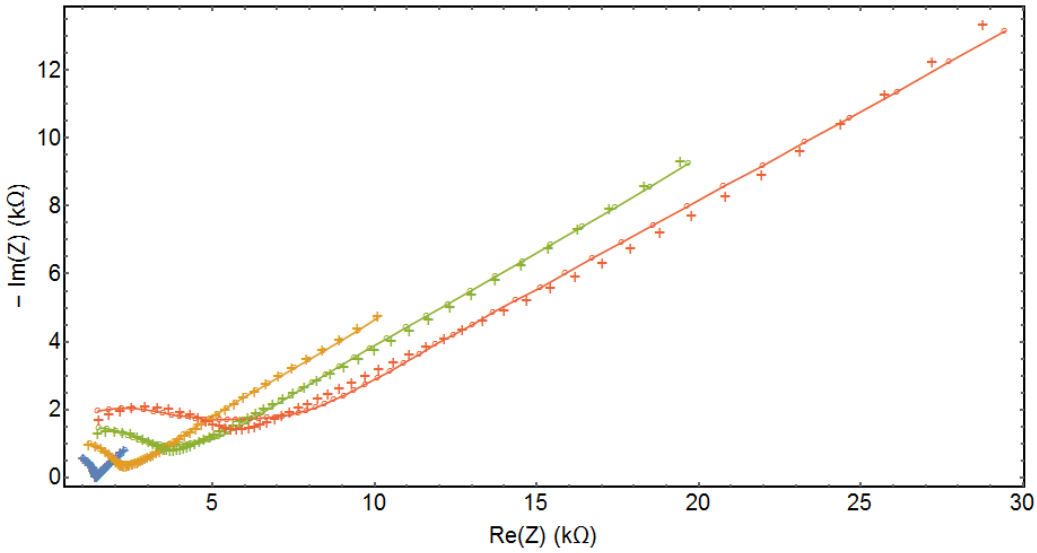

Figure 88 Every five discharge/charge cycles of a Li-S battery with their fits.

Figure 89 shows the evolution of the values for R_2 and R_3, i.e. the electrolyte and cathode charge transfer resistances respectively, during the cycling of the Li-S battery. The values were obtained from the fits of the EIS spectra displayed in Figure 86 using the model shown in Figure 87

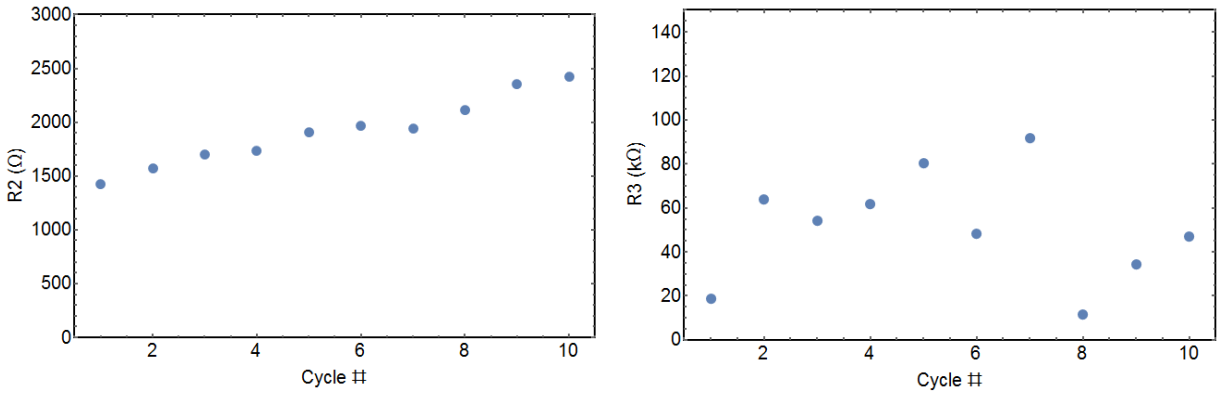

Figure 89 Evolution of R_2 and R_3 during cycling.

It can be seen from Figure 89 that during the first ten cycles, R_2 was found to increase from 1427 to 2425 Ω. The development of the cell resistivity is nearly linear and is of about +10% between the cycles. The electrochemical reaction that is seen during the first discharge and results in the double capacity than the theoretical one does not cause any substantial increase in the resistivity between the pristine and firstly discharge battery. We can therefore assume that the development of a highly resistive passivating cathode interphase, reported for $LiBH_4$-LiI cells, [112] is not observed for the $LiBH_4$-SiO_2 electrolyte.

The values for R_3 are scattered and do not show a clear trend. It illustrates the difficulty to model the tail of the EIS data. The average for the first ten cycles, is of 51 k Ω (Figure 89). The large value of the transfer resistance R_3 which may be due to the poor contact between the electrolyte and the sulfur in the cathode but most probably to the poor lithium conductivity in sulfur and in the low order polysulfides which is as low as 10^{-14} Scm^{-1} for Li_2S.[114]

5.3.4 Three Electrode setup

Impedance measurements in this chapter were carried out by Giovanni Crivellaro, MSc student at DTU Energy using a three electrode cell that we developed and first tested together. The results of three electrode measurements, performed while cycling a Li-S cell build around the LiBH4-SiO2 electrolyte are shown in Figure 90. Equivalent circuits that were used to for the EIS measurements are shown in Figure 91.

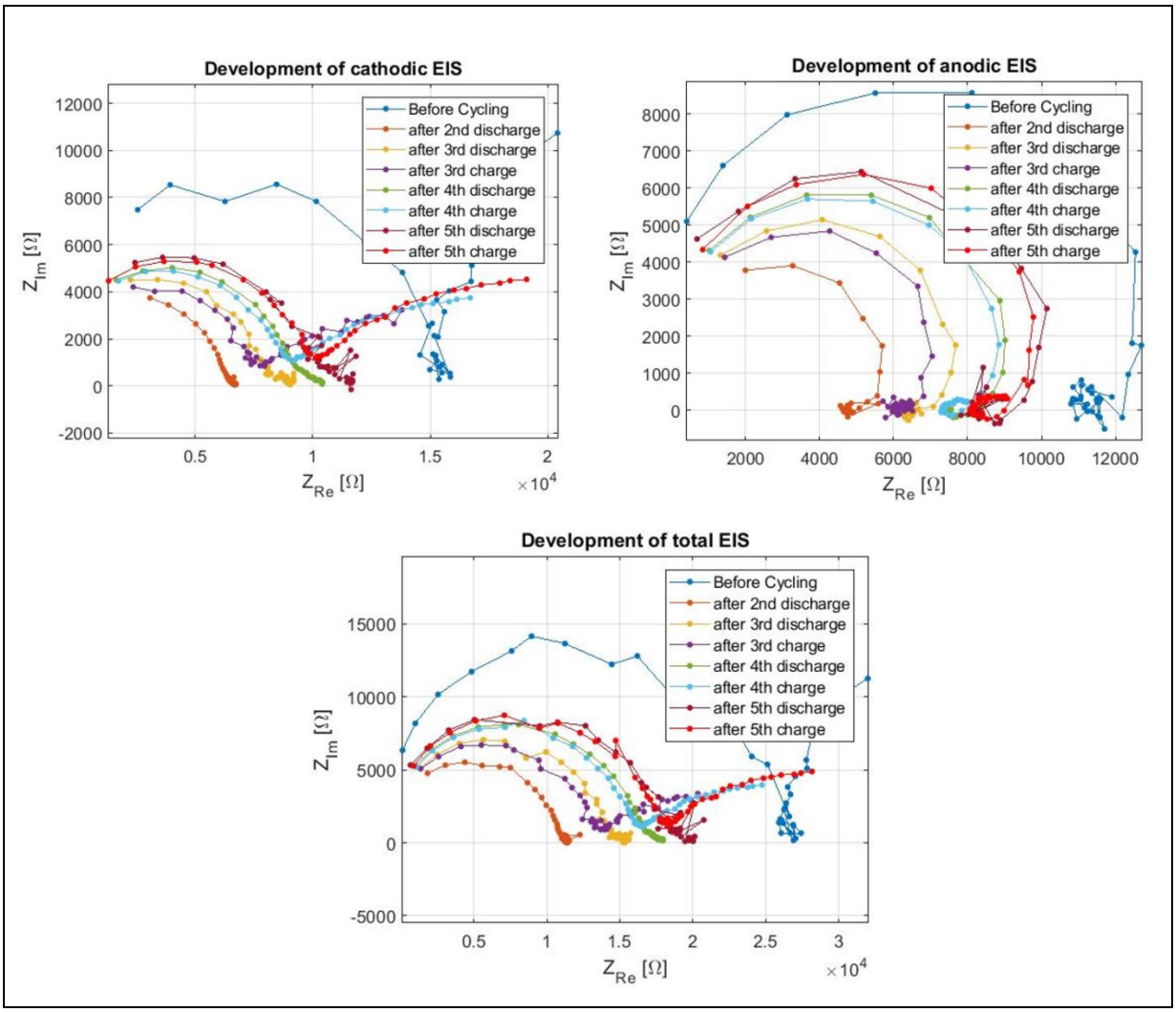

Figure 90 Development of cathodic and anodic EIS during cycling of a Li-S battery. The data were obtained by Giovanni Crivellaro (reprinted from Crivellaro, Master Thesis 2018)104

As shown in Figure 91, impedance of a negative electrode is represented by resistance and inductance in series with a constant phase element (CPE) and a Randles element. As for the cathode electrode, the equivalent circuit consist of CPE and a Randles element in series with Warburg element.

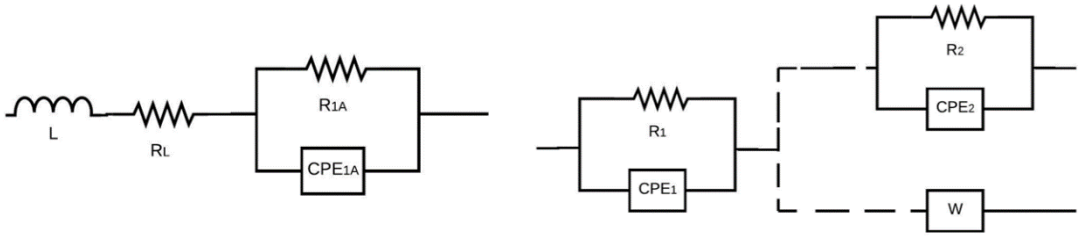

Figure 91: Equivalent circuits for impedance fits: negative electrode equivalent circuit (left) and positive and total equivalent circuit (right) (reprinted from Crivellaro, Master Thesis 2018)[104]

While the spectra of cathodic EIS show two semicircles at low frequency end which is likely due to charge transport limitations, the EIS spectra on the anode side show a different behavior – only one semicircle is seen showing inductive behavior. This is proving the assumption that the charge transport limitations in our Li-S battery are coming from the cathode side as it is the cathodic resistivity that gives a major contribution to the overall resistivity of the cell. As it was discussed earlier, observed cathodic resistivity is likely arising from transport limitations between solid-state electrolyte and sulfur.

Figure 92 and Figure 93 shows development of resistance on the anode and cathode side respectively. It can be seen from Figure 93 that the value for charge transfer resistance on eh cathode side, R2, is varying greatly during cycling and it correspond closely with the values obtained for total resistivity of the cell.

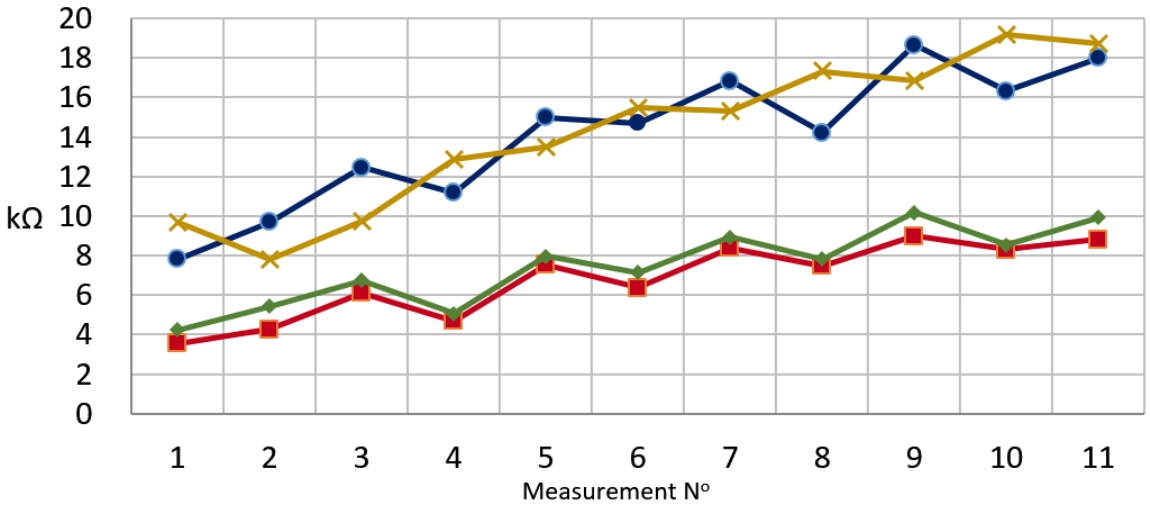

Figure 92: Red: (R1A) Resistance of the electrolyte anode side. Green: (R1) Resistance of the electrolyte cathode side. Blue: (R1A+R1) simple addition of Red and Green. Yellow: resistance from the full cell. (reprinter from Crivellaro, Master Thesis 2018)[104]

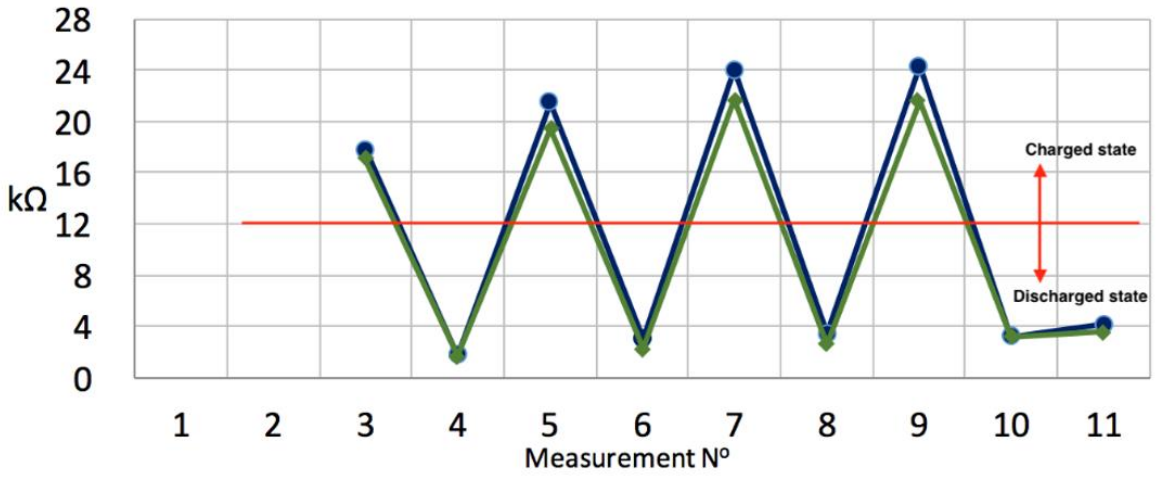

Figure 93: Green: (R2) Charge transfer resistance in the cathode. Blue: (R1+R2) Charge transfer resistance in the cathode (reprinted from Crivellaro, Master Thesis 2018)[104]

The changes in charge transfer resistance between charged and discharged state Figure 93 can be explained as while in the charged state, sulfur is formed on the cathode side and due to charge transfer resistance (Li^+ transfer form solid-state electrolyte to sulfur) the overall resistivity is high. As for the discharged state, sulfur is reduced to Li_2S thus charge transfer resistance.

The conclusion of the three-electrode study is that the values of charge transfer resistance of the cathode side dominate total resistivity of the cell. This result is in good agreement with the EIS data that was discussed in the previous section. It was possible with help of three-electrode setup to attribute high values of charge transfer resistance to Li^+ transfer form electrolyte to sulfur which is observed in charged state for lithium-sulfur cells.

5.3.5 LIPON coating for cathode protection

As it was previously shown in this chapter, the larger capacity at first cycle which was shown in Figure 78 is indicating that a reaction is occurring between electrolyte an cathode material. Therefore we have decided to protect carbon and sulfur by depositing a layer of a Li ion conductor on top of C+S to avoid direct reaction. We have chosen to use Lipon as was previously studied as a suitable material for batteries, [95] and due to its low electronic conductivity (~ $8 \cdot 10^{-14}$ Sm^{-1})[115] and acceptable Li ion conductivity (~ $1.2 \cdot 10^{-6}$ Sm^{-1}). [115] Lipon thin films with different thickness (10, 500, 1000, 1400 nm) were deposited on surface of C+S cathodes using RF magnetron sputtering. Figure 94 shows SEM images of Lipon coated cathodes with layer thickness stated above.

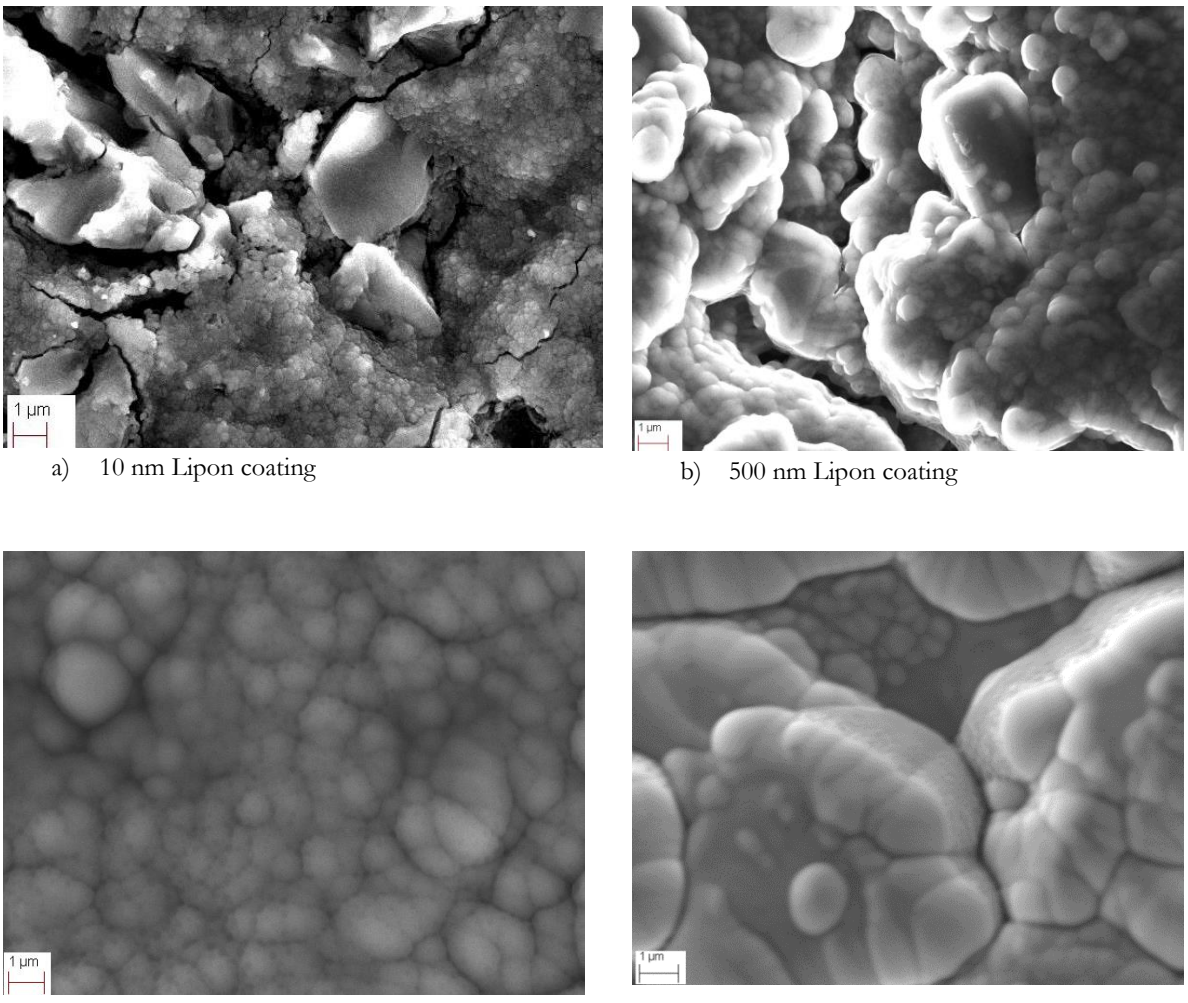

a) 10 nm Lipon coating

b) 500 nm Lipon coating

c) 1000 nm Lipon coating

d) 1400 nm Lipon coating

Figure 94 SEM micrograph of Lipon-coated cathodes with various thickness of Lipon layer

As it can be seen from Figure 94, the coating of the surface of carbon and sulfur on the cathodes is uniform for the 1000 and 1400 nm thin films, while for 10 and 500 nm the coating is

not uniform and is showing cracking, which is especially obvious for the 10 nm coated sample where non-coated support areas are observed in between of cracks. Figure 96

Figure 95 shows a lower magnification SEM image of a larger area of surface of a 10 nm thick Lipon coating where cracks and uncoated surface can be seen. Poor adhesion of the thin film and carbon and sulfur to the surface of current collector can results in peeling of the active material from electrode, bad contact to current collector and as a result poor and unstable performance of a battery.

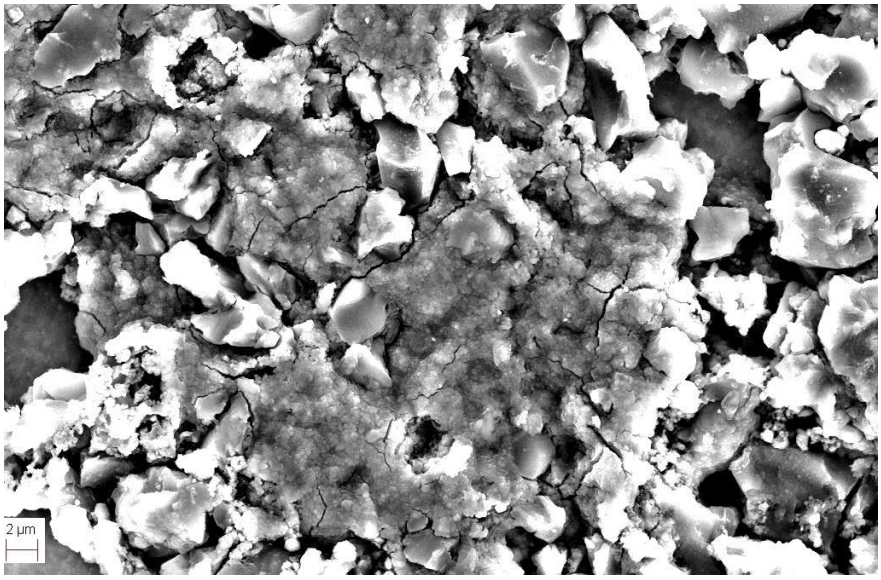

Figure 95 Surface of a 10 nm coated lipon thin film deposited on a C+S cathode

Cycling of Li-S batteries was performed using Lipon thin films with thickness stated above. While Li-S batteries with 10 and 500 nm thick Lipon layer had bad cycling capacities most likely due to bad contact between sulfur and electrolyte, the Li-S battery with 1400 nm thick coating showed no capacity at all which is likely because the Lipon layer is too thick and is a poor conductor due to thickness. The battery with a 1000 nm coating had a good cycling performance and its charge-discharge curves are shown in Figure 96.

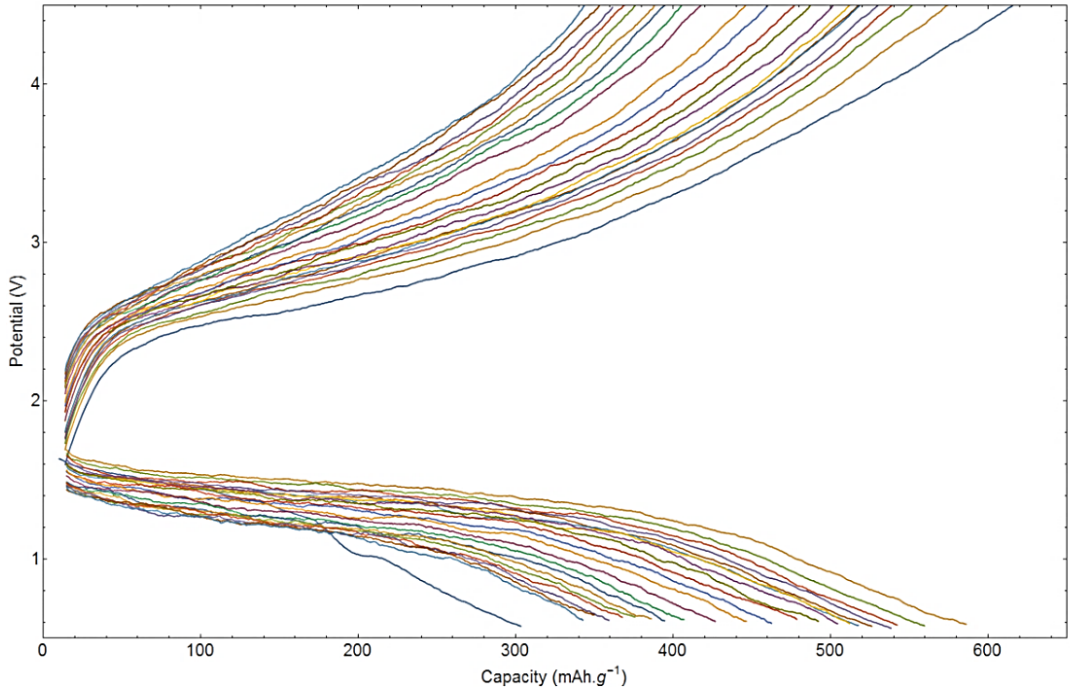

Figure 96 Discharge-charge cycles of a LiS battery with 1µm Lipon coated C+S cathode (Adapted from Lefevt, el al, 2018 [116])

It can be seen from Figure 96, that no decrease in capacity after first and second discharge that is observed for a reference a Li-S battery with non-coated cathode which is shown in Figure 97.

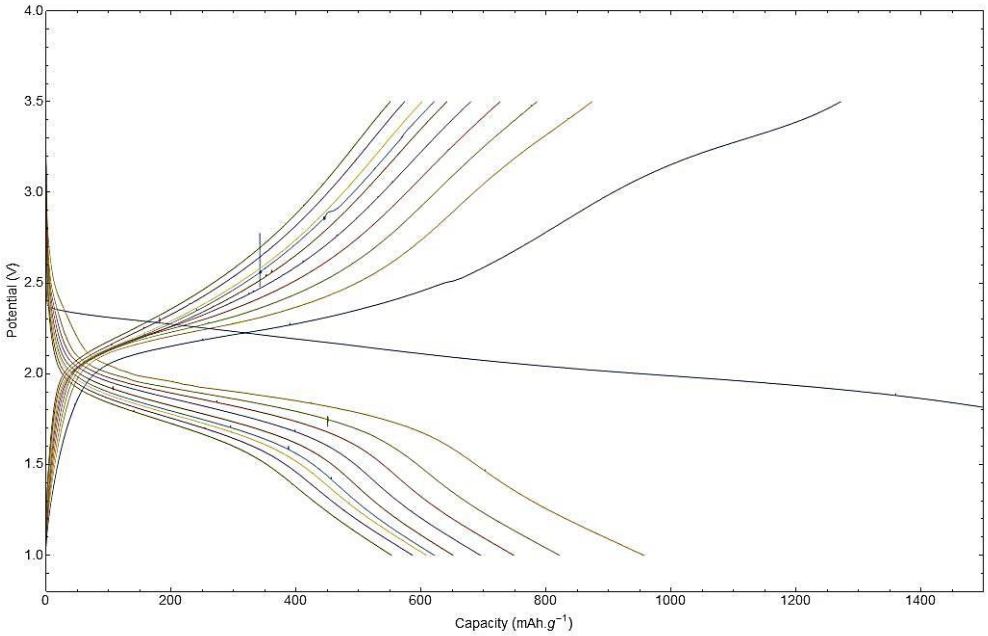

Figure 97 Discharge-charge cycles of a reference Li-S battery with C+S cathode (Adapted from Lefevt, el al, 2018 [116])

The charge-discharge cycles in Figure 96 exhibit curved slopes compared to sharper lines in Figure 97, which can be explained with that a distribution of polysulfide species is present in the Lipon coated battery which means that the transition from one discharge plateau to another one will be smoothed. Lower voltage for a Li-S battery compared to a non-coated battery seen in Figure 78 can be explained with ohmic drop to the Lipon layer that was calculated to be 5-6 mV.

Figure 98 Impedance spectra shows impedance spectra of a fresh Li-S battery with a 1µm Lipon coating (on the left) and a non-coated C+S cathode before first discharge (on the right).

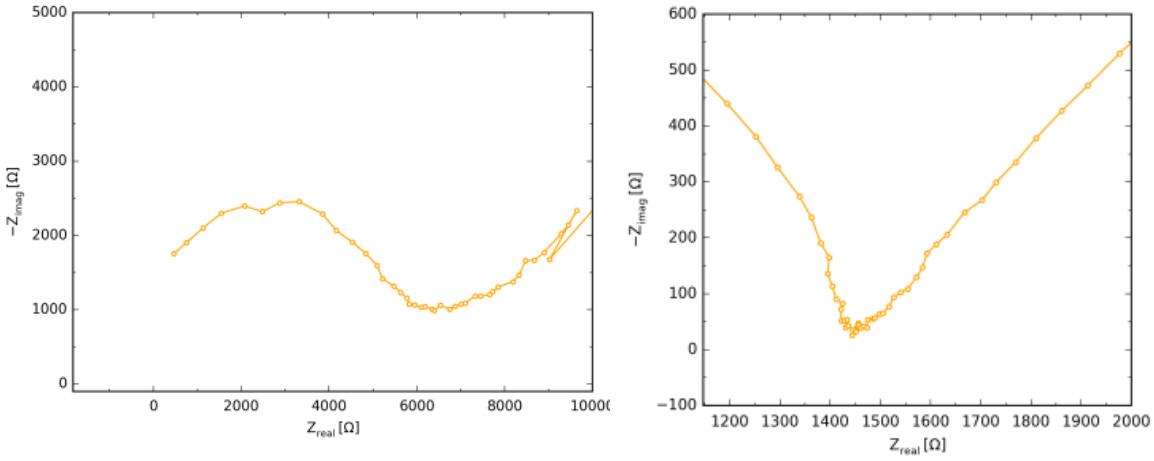

Figure 98 Impedance spectra of a fresh Li-S battery with a 1µm Lipon coathed C+S cathode (left) and non-coated C+S cathode (right)

As it can be seen in Figure 98 Impedance spectra the resistivity of a Lipon coated cathode is much higher (6 kΩ) compared to resistivity of a battery with non-coated cathode (1,4 kΩ) which is likely due to bad contact between sulfur particles and electrolyte. Some noise can be seen in impedance spectra which are likely due to the instrumental contribution as the equipment is working at frequency of 50 Hz which is causing noise. Furthermore, the presence of two arcs can be seen from the spectra of battery with coated which indicates the presence of two characteristic frequency intervals, however the two arcs are not well-resolved in impedance spectrum.

Characterization of Lipon layer was performed on a cycled Li-S battery to see whether the high resistance of a Lipon thin film was mechanical problems, such as cracking of a film when the pressure was applied to the cell, or by degradation process, either by exposure to gases in the glovebox or during the operation of the cell.

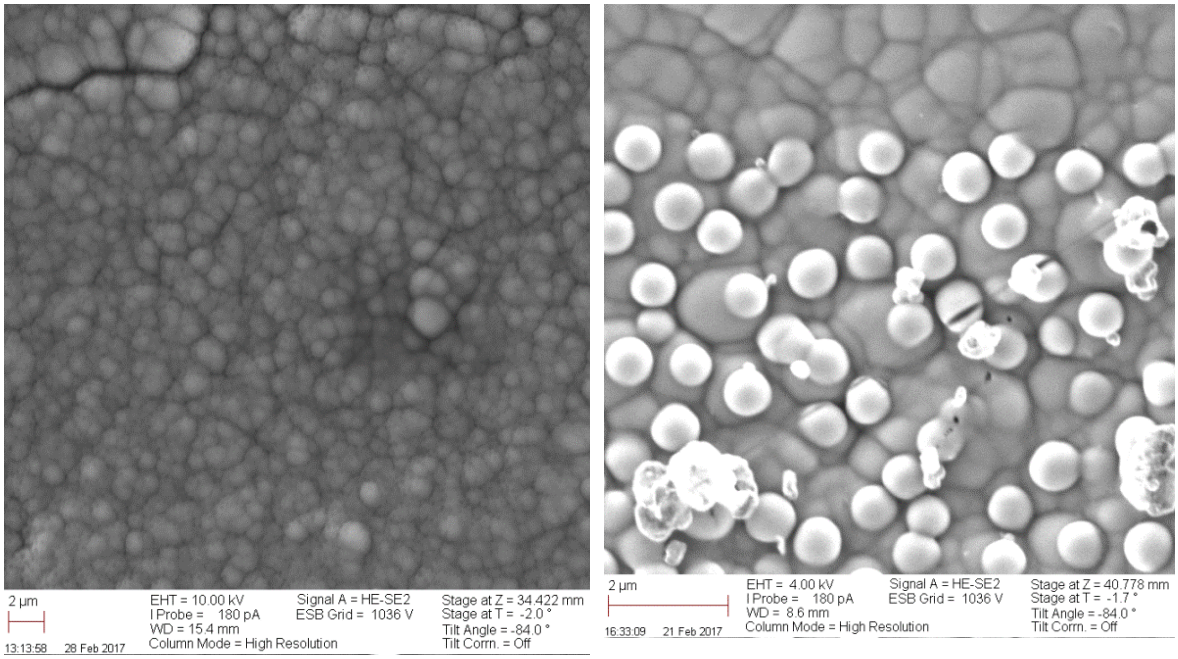

Figure 99 SEM micrograph of 1 µm Lipon-coated cathodes showing growth of bubble-like structues

As it can be seen from Figure 99, the surface of Lipon coating in a cycled battery is uniform (left), however after a short time after initial images are taken, surface of thin film becomes uneven with bubble-like objects growing on the surface. This effect is likely due to decomposition of Lipon thin film in the electron beam.

5.3.6 XRS Measurements

In order to study the possible reaction between the electrolyte and lithium metal XRS Measurements have been performed on pristine $LiBH_4$-MCM 41 solid electrolyte and a cycled pellet used during EIS measurement in a symmetric Li|SE|Li cell. MCM-41 is a mesoporous silica scaffold giving the similar increased in conductivity as SiO_2 aerogel. Figure 100 compares the edges of Li, Si, B and O for the pristine (above) and cycled (below) pellets. The "pellet edges" are the two sides of the pellet which were in contact with Li. The percentage on the plots refers to the degree of pores filling of the mesoporous MCM-41. 100 % means that the $LiBH_4$ volume use to prepare the electrolyte should filled up all the pores of the scaffold while 50 % means that half of the volume of the pores should be filled. In the latter case it is expected that the ratio of interfacial layer to bulk $LiBH_4$ is higher. The plot labelled as "mixture" is for a sample where the $LiBH_4$ and SIO_2 were just hand mixed, not ball-milled or melt infiltrated. The cycled pellet was made from the 100 % pore filling powder.

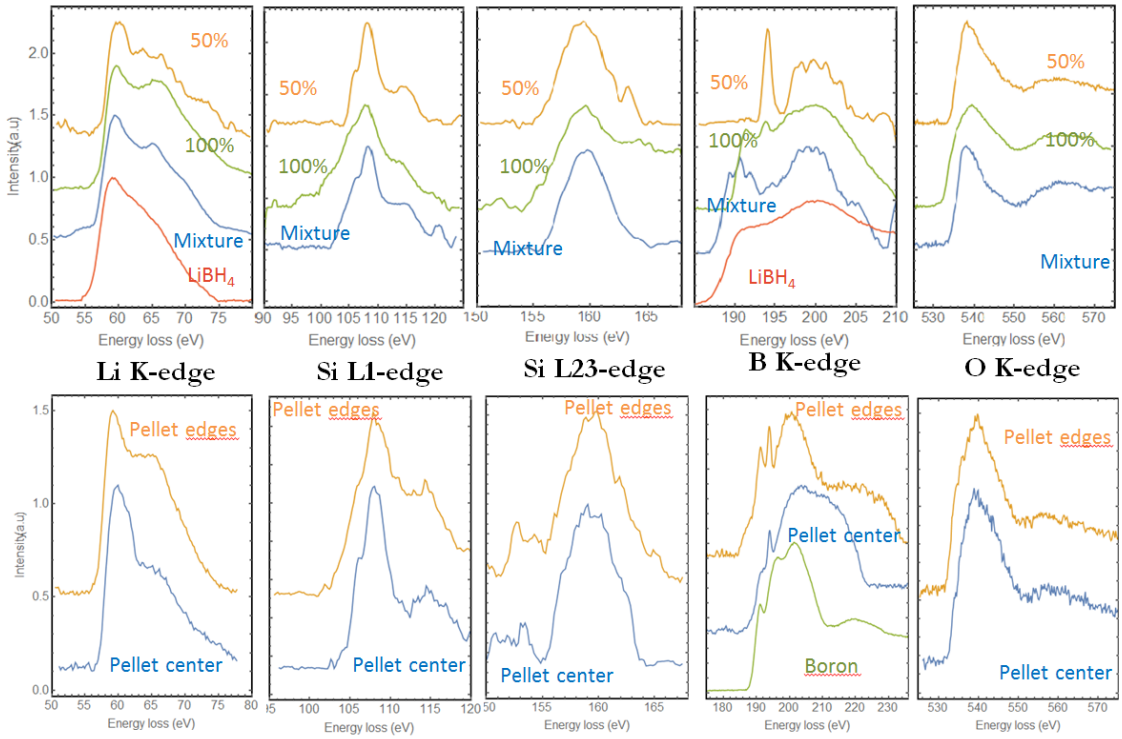

Figure 100 XRS measurements on LiBH4-MCM 41 pristine (above) and cycled (below) pellets

While no major changes are observed in O and Si edges, which was expected as no oxidation is taking place, XRS Measurements show changes in lithium and boron edge. As for the changes in lithium edge, these are indicating significant difference in structure between composites and pure $LiBH_4$. While one peak is seen for pure $LiBH_4$, at least two peaks are observed for composites which supports the idea of several populations from NMR measurements.

For boron edge, the differences are clear between different loadings of $LiBH_4$ and furthermore within different parts of a pellet. New peaks are observed which is likely due to a reaction between sulfur and $LiBH_4$ that can results in formation of Li_2S, $Li_2B_{12}H_{12}$ and Li_3BS_2 and gases such as H_2, B_2H_6 and H_2S. [117] Formation of H_2 was also detected with Raman spectroscopy and NMR which indicates that a direct reaction is possible. In order to eliminate the possibility of the reaction, Lipon coating can be performed.

As for the sulfur edge, no changes were observed before and after cycling. X-Ray Raman measurements carried out at Elletra Synchrotrone showed no changes on sulfur egde as well. These could be explained by that the reaction is taking place in the very center of pellet while the measurement is performed at the edges of the pellet where no reaction is taking place.

The conclusion of the XRS study is that before and after cycling, no new compounds are formed meaning that the battery is stable under operation. At the same time, change in boron edge are indicating that there is a possibility of direct reaction between sulfur and $LiBH_4$ which can be avoided by means of cathode coating.

5.3.7 Microtomography

There is evidence of growing particle size and sulfur agglomeration in li-s liquid electrolyte systems[118] which could be occurring in li-s systems with solid electrolyte as well as suggested by SEM image performed on the cathode material after discharge where Li_2S is expected to be formed (see Section 5.3.2). Depletion of sulfur in certain areas of the cathode has also been observed for liquid systems which could be causing decreased capacity during cycling of solid li-s batteries as well.

In order to study changes in sulfur distribution in cathode material during charging and discharging, X-Ray Microtomography has been performed on cycled batteries at different stages of charge. Microtomography of a capillary battery after initial discharge packed in quartz capillaries with outer diameter of 0.5-1 mm was performed using high precision rotation stage setup. Obtained images, raw and processed, are shown in Figure 101.

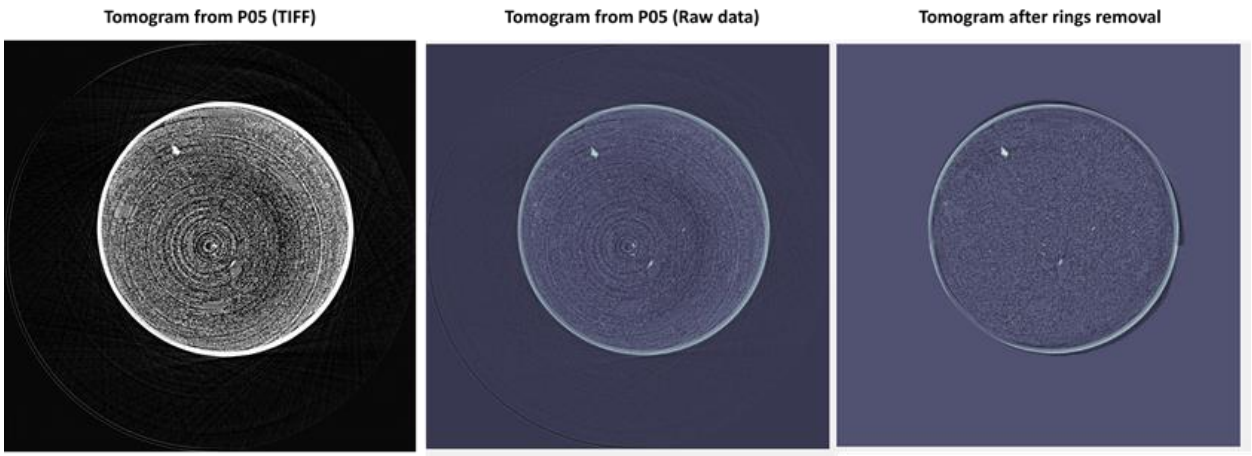

Figure 101 Tomograms of a capillary LiS cells obtained from P05 beamline

As it can be seen from Figure 101 to the left, the raw data that has been collected from the tomography beamline is superimposed by strong artifacts rings. These are common in analysis of tomographic images and arise from defects and non-uniformity of CCD camera pixels and

defects or impurities in the scintillator screen. While a common way to reduce ring artifacts in flatfield correction[119] where background images without sample are taken at regular intervals before and after data acquisition with a sample was performed.

Due to shortage of time for beamtime measurements, no flatfield correction was performed for the Li-S capillaries, for that reason ring artifacts had to be removed by filtering data. This is done by analyzing sonograms of measured data and studying sum values of gray color in each column. The results of filtering raw data are shown in Figure 101 to the right. As it can be seen from the processed image, the removal of rings leads to creation of secondary rings (although less pronounced) and loss of data quality as filtering removes intensity of signal in the areas without rings which can be seen by comparing .

The data obtained from processed images were then used to study distribution of sulfur in a Li-S battery by comparing images at different stages of charge/discharge process. As it was shown in Section 5.3.2, SEM images of batteries discharged to 1V reveal formation of grains (1-3 μm) which could be short-chain polysulfides such as Li_2S which should be present at this stage of discharge.

Contract enhancement was performed on the obtained images to distinguish between the two phases and the results are shown in Figure 102 where a randomly cropped slice of capillary battery with 30/70 wt% $LiBH_4$-SiO_2 electrolyte is seen without (left) and with enhanced contract between phases.

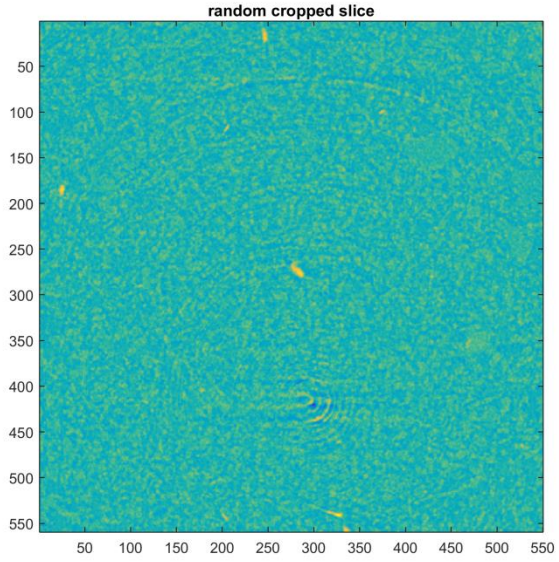

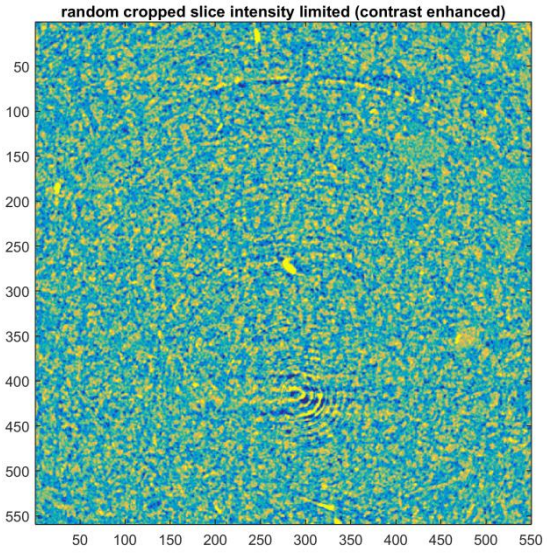

Figure 102 Tomographic image of a slice of a capillary (left) without and with enhanced contract (right)

As it can be seen from Figure 102 on the left, the contrast contrast between silica particles and sulfur is very low as difference between silicon and sulfur's attenuation coefficientss (ratios of atomic number-to-mass, Z/A are 0.49848 for silicon and 0,49897 for sulfur)[120] is small which makes it difficul to see the formation of sulfur in solid electroyte.

Figure 103 shows the reconstruction of a tomography as a lateral cut of a Li-S capillary. For this reconstruction, the images without enhanced correction were used. The colors were assigned to the image on the basis of color intensity which was assigned colors from green to yellow, orange and red. The red polygon that can be seen in the left part of the image is the steel rod serving as current collector.

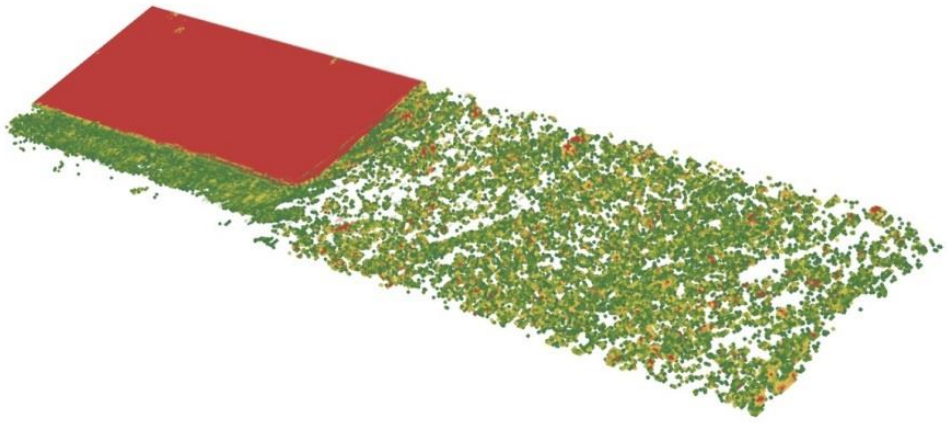

Figure 103 Latetal reconstruction of the tomography in 2D

It can be seen from Figure 103, that heavier particles (shown in red) are found along the capillary, however large agglomerations of the particles is around the electrode (red polygon) which could be indicating that a process similar to the one observed in liquid li-s is occurring in solid state as well. Figure 104 shows a 3D reconstruction of three areas in the electrolyte: center of the battery (left below), interface between electrolyte and C+S layer (right top) and C+S layer (right below).

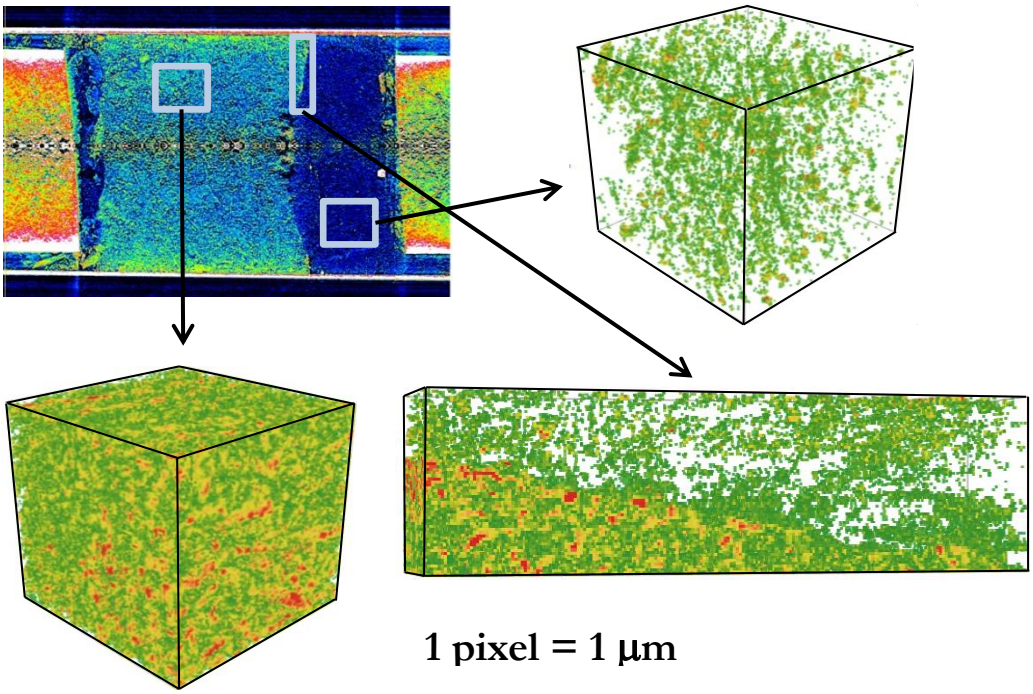

Figure 104 3D Reconstructions of areas in the middle of solid electrolyte (left), carbon and sulfur powder as cathode (right bottom) and interface between solid electrolyte and cathode material (right top)

As it can be seen from the reconstruction, the distribution of sulfur is homogeneous as sulfur particles are well-dispersed in the electrolyte and in the C+S layer.

In order to see a more precision distribution of larger particles which could be the formed Li_2S during discharge, the reconstruction of images with increased contrast showing particles with highest density than $LiBH_4$ that is made transparent was performed and the result of consonstruction of images in a capillary is shown in Figure 105.

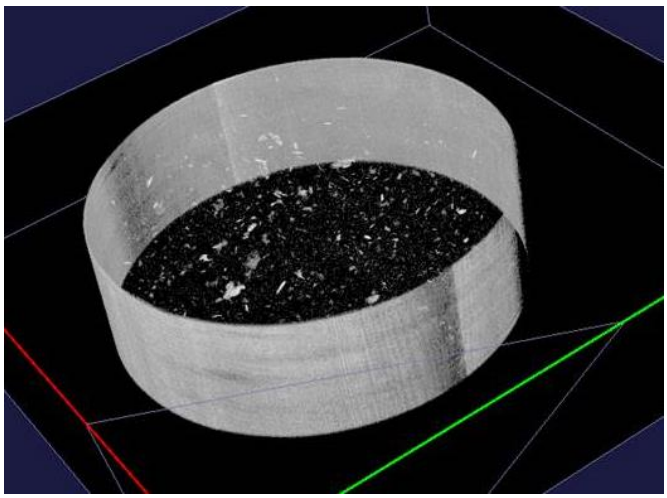

Figure 105 Reconstruction of a section (Adapted from Lefevt, el al, 2018 [116])

As it can be seen from Figure 105, there are particles in the top part of the capillary, however it is difficult to say whether the particles are sulfur species formed that were seen om SEM images of a discharged battery or it larger pieces of sulfur mixed with electrolyte, it is also possible that the particles are the quarts pieces peeling off from the sides of the capaillary due to scratching sides with steel current collectors during preparation process.

The limitation of the measurement is that the recorded spectra do not correspond directly to refractive indexes of the compounds, which would allow direct identification of compounds in the capillary. In order to make identification from the homographs obtained in this work, it is required to know densities of all intermediate species in the reaction:

$$S_8\text{-}Li_2S_8\text{-}Li_2S_6\text{-}Li_2S_4\text{-}\ Li_2S_2\text{-}\ Li_2S$$

As the intermediate species are not commercially available and only exist during charging and discharging of a battery, furthermore, the difference in weight which makes identification of sulfur species a difficult task.

The conclusion that can be drawn from analyzing obtained homographs is that the formation of particles in the electrolyte is uniform, however X-Ray tomography with resolution in micron-range cannot give additional information to what already is known from electrochemical measurements and SEM imaging and other technique should be applied.

5.3.8 Conclusions on Li-S batteries with $LiBH_4$-SiO_2 electrolyte

All-solid-state lithium-sulfur batteries build around $LiBH_4$-SiO_2 solid-state electrolyte have been tested in this work. Batteries show high specific capacity and high capacity retention during cycling however at slow charge-discharge rates. The initial discharge-charge cycle of these Li-S batteries gave capacities almost the double of the theoretical ones due to a side reaction. This electrochemical side reaction is only partially reversible at the charging voltage used herein; a small overcapacity was also seen during the first charge. The side reaction must originate from a reaction at the cathode side as lithium has proven to be stable against $LiBH_4$-SiO_2 solid-state electrolyte, therefore this reaction most likely is due to an interaction of the solid-electrolyte with the carbon matrix.

In order to protect cathodes from a side reaction, cathodes have been coated with a LIPON layer. Li-S batteries with coated cathodes did not exhibit this first high discharge capacity and furthermore better capacity retention upon cycling where achieve than for the Li-S batteries with non-coated cathodes. These results prove that it is possible to protect the cathode from parasitic reactions with the solid-state electrolyte by depositing a nanometer thick thin film on its surface.

Impedance measurements were performed on Li-S batteries and obtained spectra no evidence of formation of highly resistive passivating interphases on the cathode side which has been reported for $LiBH_4$-LiI cells. [112] The overall increase of cell resistivity is likely due to poor contact between sulfur and solid state electrolyte. Apart from bad contact, the reasons for increased resistivity could be low conductivity of the low order polysulfides that is as low as 10^{-14} Scm^{-1} (for Li_2S)[114] and charge transfer resistance between solid electrolyte and sulfur on the cathode side. This shows importance of surface engineering for lithium-sulfur cells.

We have performed X-Ray diffraction, Raman and X-Ray tomography imaging to probe the formation of lithium polysulfides during discharging of the cells. It has not been possible to extract quantitative information from the microtomographs since the contrast is too low between the different species. However, the results show that the growth of particles was uniform in the cell, which means that the sulfur material was utilized uniformly and efficiently in the cell. No changes were observed in sulfur edge in X-Ray Raman measurements during discharging of the cell which is due to limited penetration depth of the X-Ray beam which resulted in probing of side of cathode far from the electrolyte. As the cells that were prepared for synchrotron measurements are not pressed as we otherwise did for Li-S batteries, it is difficult to achieve good contact between sulfur and solid state electrolyte.

Chapter 6

Conclusions and Outlook

6.1 Conclusions

The main purpose of the present thesis was to investigate the possibility of improving performance of all solid-state Li-S batteries by using novel all-solid-state electrolytes based on $LiBH_4$. Ballmilled $LiBH_4$-SiO_2 composites, various ratios of silica aerogel and $LiBH_4$-$LiBF_4$ were tested in all-solid state batteries. Furthermore the mobility of Li ions was investigated by techniques, such as impedance spectroscopy, Raman spectroscopy and NMR. As Li-S batteries show higher capacities than the theoretical ones at first discharge/charge cycle, the possibility of protecting cathode layer by magnetron sputtering with Lipon thin film of various thickness (10, 500, 1000 and 1400 nm) was investigated in solid-state lithium sulfur batteries.

Prepared $LiBH_4$-SiO_2 composites have higher Li^+ conductivities compared to pure $LiBH_4$ at room temperature (10^{-4} S/cm^{-1} and 10^{-4} S/cm^{-1} and respectively). XRD measurements did not show any evidence of formation of new phases, however NMR and Raman measurements showed that the behavior of $LiBH_4$-SiO_2 composites is clearly different from pure $LiBH_4$. ^{7}Li NMR showed formation of an interphase between silica and borohydride which is likely originating from a reaction between $LiBH_4$ and silanol groups present on the surface of silica particles.

The $LiBH_4$ - $LiBF_4$ composites with low loading of $LiBF_4$ show higher conductivities than pure $LiBH_4$ which is likely due to a formation of solid solution with $LiBF_4$. For the higher $LiBF_4$ loadings, lower conductivities are seen which is likely to decomposition of $LiBH_4$.

All-solid-state lithium-sulfur batteries using $LiBH_4$-SiO_2 electrode have been successfully built and cycled. Batteries had coulombic efficiency of about 88.7%, with average capacity loss of around 7% after first 10 cycles. It was shown by using a three electrode setup that the increase of total resistivity of the cell was not due to formation of highly resistive interphase between

cathode and solid-state electrolyte but due to poor contract between cathode and electrolyte. Most likely there is a contribution from low conducting low order polysulfides that accounts for increase in total resistivity of the cell.

As lithium-sulfur cells showed higher capacities than the theoretical ones at first discharge/charge cycle, which is likely to due to a reaction between $LiBH_4$ and carbon matrix, we have investigate the possibility to protect cathode material with Lipon thin films. Li-S batteries with Lipon protected cathodes show better capacity retention during cycling compared to batteries with non-coated cathodes, furthermore they exhibit no overcapacities at first discharge/charge cycle. These results show the importance of surface treatment for improved performance of lithium-sulfur batteries.

6.2 Outlook

In the recent decades, much research has been focused on solid electrolytes as these are safer alternatives to liquid Li-ion batteries. Lithium borohydride is a promising material for battery storage and conductivity of $LiBH_4$ could be improved by mixing with silica oxide and $LiBF_4$ which both introduce defects in $LiBH_4$ crystal lattice and thus introducing a new pathway for Li ion diffusion.

To improve conductivity of electrolyte, drying silica at higher temperature (up to 463 K) can be recommended as silica drying at higher temperatures gives highest state of hydroxylation and removes H_2O monolayer from the surface of silica which will allow silanol groups to react with $LiBH_4$ and form a highly mobile layer accounting for high Li ion conductivity. There are a number of metal oxides with surface hydroxyl groups that can be used for mixing with $LiBH_4$ in a similar way that was performed with SiO_2 in this work, e.g. ZnO, TiO2, Al_2O_3, to achieve increased conductivity at room temperature.

To improve the performance of cathode, the use of techniques to study interfaces that could help to identify whether the formation of species follows the same steps as in LiS batteries with liquid electrolyte. Development of methods that allow studying what intermediate species are formed during charge and discharge process, as there is evidence of formation of various intermediate products in the literature. XANES could be a good technique to continue with research on polysulfides. Another technique that could give valuable results is XPS which was used by other research groups for characterization of liquid-based Li-S systems.

Furthermore, the origins of decreased capacity can be investigated in more detail to gain knowledge on how to protect cathode from a reaction that is likely to take place during first charge and discharge. As the batteries require pressure in order to work, it is difficult to investigate the role of interfaces, however there is evidence of a reaction during first charge-discharge cycle which could be eliminated by coating of cathode by a suitable thin film.

As for the cathodic protection, same method of deposition is required in order to have reproducible battery tests. Pressure could be another issue as it is difficult to control it once in the cell. Protection of cathode could help to decrease loss of capacity during cycling and this can be seen as a major issue that needs to be addressed before Li-S technology can be commercialized. A way to improve contact could by polishing or pressing the surface of the cathode in order to reduce particle size of sulfur particles that are large and could be the reason behind bad contact of electrolyte and cathode.

References

(1) U.S. Energy Information Administration. *Monthly Energy Review August 2018*; 2018.

(2) Goodenough, J. B.; Kim, Y. Challenges for Rechargeable Li Batteries. *Chem. Mater.* **2010**, *22* (3), 587–603.

(3) Boden, T.A., G. Marland, and R. J. A. Global, Regional, and National Fossil-Fuel CO2 Emissions. **2017**.

(4) Boden, T.; Andres, B.; Maryland, G. *Global Greenhouse Gas Emissions Data*; 2017.

(5) BP. Statistical Review of World Energy 2018. **2018**, 1–53.

(6) Manthiram, A.; Fu, Y.; Chung, S.; Zu, C.; Su, Y. Rechargeable Lithium − Sulfur Batteries. *Chem. Rev.* **2014**, *114*, 11751–11787.

(7) Energinet. Hvor kommer strømmen fra https://energinet.dk/El/Miljoedeklarationer/Hvor-kommer-stroemmen-fra (accessed Sep 2, 2018).

(8) Energinet. Wind power to combat climate change http://energinet.dk/DA/KLIMA-OG-MILJOE/Energi-og-klima/dendanskevindcase/Sider/Den-danske-vindcase.aspx (accessed Apr 27, 2017).

(9) Zaghib, K.; Mauger, A.; Julien, C. M. *12 - Rechargeable Lithium Batteries for Energy Storage in Smart Grids*; Elsevier Ltd., 2017.

(10) Van Noorden, R. Sulphur Back in Vogue for Batteries. *Nature* **2013**, *498* (7455), 416–417.

(11) Kaldellis, J. K. Ã.; Zafirakis, D. Optimum Energy Storage Techniques for the Improvement of Renewable Energy Sources-Based Electricity Generation Economic Efficiency. **2007**, *32*, 2295–2305.

(12) Mcdowall, J. Integrating Energy Storage with Wind Power in Weak Electricity Grids. **2006**, *162*, 959–964.

(13) Hadjipaschalis, I.; Poullikkas, A.; Efthimiou, V. Overview of Current and Future Energy Storage Technologies for Electric Power Applications. **2009**, *13*, 1513–1522.

(14) Fan, X.; Sun, W.; Meng, F.; Xing, A.; Liu, J. Advanced Chemical Strategies for Lithium-Sulfur Batteries: A Review. *Green Energy Environ.* **2017**, *3* (1), 2–19.

(15) OxisEnergyLtd. Our Cell and Battery Technology Advantages https://oxisenergy.com/technology/ (accessed Nov 11, 2018).

(16) Blomgren, G. E. The Development and Future of Lithium Ion Batteries. *J. Electrochem. Soc.* **2017**, *164* (1), A5019–A5025.

(17) NikkeiInc. Sony battery to offer 40% longer phone life https://asia.nikkei.com/Tech-Science/Tech/Sony-battery-to-offer-40-longer-phone-life (accessed Nov 11, 2018).

(18) Scheers, J.; Fantini, S.; Johansson, P. A Review of Electrolytes for Lithium-Sulphur Batteries. *J. Power Sources* **2014**, *255*, 204–218.

(19) Zhi Wei Seh, Yongming Sun, Qianfan Zhangc, Y. C. Designing High-Energy Lithium–sulfur Batteries. *Chem. Soc. Rev.* **2016**, *45*, 5605--5634.

(20) SolidPower. Solid-State 101 http://solidpowerbattery.com/solid-state-101/ (accessed Nov 12, 2018).

(21) Smith, L. J. Hyundai claims to have made solid-state electric car battery "breakthrough" technology https://www.express.co.uk/life-style/cars/987676/Hyundai-electric-car-solid-state-battery-technology-breakthrough (accessed Nov 11, 2018).

(22) HyundaiMotorCompany. Hyundai CRADLE Partners with Ionic Materials to Advance Battery Technology Development https://www.hyundaimotorgroup.com/MediaCenter/News/Press-Releases/hmc-CRADLE-180710.hub#.W-imwzEvxEY (accessed Nov 11, 2018).

(23) Reuters. Solid Power, BMW partner to develop next-generation EV batteries https://www.reuters.com/article/us-bmw-solid-power/solid-power-bmw-partner-to-develop-next-generation-ev-batteries-idUSKBN1EC16V (accessed Nov 11, 2018).

(24) Seo, I.; Martin, S. W. New Developments in Solid Electrolytes for Thin-Film Lithium Batteries. *Lithium Ion Batter. - New Dev.* **2012**, No. 1, 101–144.

(25) Bruce, P. G.; West, A. R. The A-C Conductivity of Polycrystalline LISICON, Li2+2x Zn1-X GeO4, and a Model for Intergranular Constriction Resistances. *J. Electrochem. Soc.* **1983**, *130* (3), 662–669.

(26) Bachman, J. C.; Muy, S.; Grimaud, A.; Chang, H. H.; Pour, N.; Lux, S. F.; Paschos, O.; Maglia, F.; Lupart, S.; Lamp, P.; et al. Inorganic Solid-State Electrolytes for Lithium Batteries: Mechanisms and Properties Governing Ion Conduction. *Chem. Rev.* **2016**, *116* (1), 140–162.

(27) Mohtadi, R.; Orimo, S. The Renaissance of Hydrides as Energy. *Nat. Publ. Gr.* **2016**, *2*, 1–16.

(28) Züttel, A.; Wenger, P.; Rentsch, S.; Sudan, P.; Mauron, P.; Emmenegger, C. LiBH4 a New Hydrogen Storage Material. *J. Power Sources* **2003**, *118* (1–2), 1–7.

(29) Łodziana, Z.; Vegge, T. Structural Stability of Complex Hydrides: LiBH4 Revisited. *Phys. Rev. Lett.* **2004**, *93*, 145501.

(30) Blanchard, D.; Shi, Q.; Boothroyd, C. B.; Vegge, T. Reversibility of Al/Ti Modified LiBH4. *J. Phys. Chem. C* **2009**, *113* (31), 14059–14066.

(31) Lemordant, D.; Blanchard, F.; Bosser, G.; Carré, B.; Chimie-physique, L. Physicochemical Properties of Fluorine-Containing. **2005**.

(32) Zhang, S. S. Liquid Electrolyte Lithium/sulfur Battery: Fundamental Chemistry, Problems, and Solutions. *J. Power Sources* **2013**, *231*, 153–162.

(33) Jeon, B. H.; Yeon, J. H.; Kim, K. M.; Chung, I. J. Preparation and Electrochemical Properties of Lithium-Sulfur Polymer Batteries. *J. Power Sources* **2002**, *109* (1), 89–97.

(34) Yeon, J.-T.; Jang, J.-Y.; Han, J.-G.; Cho, J.; Lee, K. T.; Choi, N.-S. Raman Spectroscopic and X-Ray Diffraction Studies of Sulfur Composite Electrodes during Discharge and Charge. *J. Electrochem. Soc.* **2012**, *159* (8), A1308–A1314.

(35) Patel, K. Lithium-Sulfur Battery: Chemistry, Challenges, Cost, and Future. *J. Undergrad. Res.* **2016**, *9*, 39–42.

(36) Shamsuri, A. A.; Abdullah, D. K. Ionic Liquids: Preparations and Limitations. *Makara* **2010**, *14* (2), 101–106.

(37) Chandra, S. *Supersonic Solids. Principles and Applications*; North-Holland Publishing company: Amsterdam, The Netherlands, 1981.

(38) Lindiard, A. B. *Handbuch Der Physik*; S.Flugge, Ed.; Springer-Verlag: Berlin, Germany, 1957.

(39) Jost, W. No Title. In *Diffusion in Solids, Liquids and Gases*; Academic Press: New York, 1952.

(40) Maier, J. Defect Chemistry and Conductivity Effects in Heterogeneous Solid Electrolytes. *J. Electrochem. Soc.* **1987**, *134* (6), 1524–1535.

(41) Maier, J. Defect Chemistry and Ionic Conductivity in Thin Films. *Solid State Ionics* **1987**, *23* (1–2), 59–67.

(42) Mohtadi, R.; Orimo, S. I. The Renaissance of Hydrides as Energy Materials. *Natrue Rev. Mater.* **2016**, *2* (3), 1–16.

(43) Soulié, J. P.; Renaudin, G.; Erný, R.; Yvon, K. Lithium Borohydride LiBH4: I. Crystal Structure. *J. Alloys Compd.* **2002**, *346* (1–2), 200–205.

(44) Matsuo, M.; Nakamori, Y.; Orimo, S.; Maekawa, H.; Takamura, H. Lithium Superionic Conduction in Lithium Borohydride Accompanied by Structural Transition. *Appl. Phys. Lett.* **2007**, *91* (22), 224103.

(45) Matsuo, M.; Orimo, S. I. Lithium Fast-Ionic Conduction in Complex Hydrides: Review and Prospects. *Adv. Energy Mater.* **2011**, *1* (2), 161–172.

(46) Maekawa, H.; Matsuo, M.; Takamura, H.; Ando, M.; Noda, Y.; Karahashi, T.; Orimo, S.

Halide-Stabilized LiBH4, a Room-Temperature Lithium Fast-Ion Conductor. *J. Am. Chem. Soc.* **2009**, *131* (3), 894–895.

(47) Sveinbjörnsson, D.; Christiansen, A. S.; Viskinde, R.; Norby, P.; Vegge, T. The LiBH4-LiI Solid Solution as an Electrolyte in an All-Solid-State Battery. *J. Electrochem. Soc.* **2014**, *161* (9), A1432–A1439.

(48) Myrdal, J. S. G.; Blanchard, D.; Sveinbjörnsson, D.; Vegge, T. Li-Ion Conduction in the LiBH4:LiI System from Density Functional Theory Calculations and Quasi-Elastic Neutron Scattering. *J. Phys. Chem. C* **2013**, *117* (18), 9084–9091.

(49) Liu, X.; Majzoub, E. H.; Stavila, V.; Bhakta, R. K.; Allendorf, M. D.; Shane, D. T.; Conradi, M. S.; Verdal, N.; Udovic, T. J.; Hwang, S.-J. Probing the Unusual Anion Mobility of LiBH4 Confined in Highly Ordered Nanoporous Carbon Frameworks via Solid State NMR and Quasielastic Neutron Scattering. *J. Mater. Chem. A* **2013**, *1* (34), 9935.

(50) Das, S.; Ngene, P.; Norby, P.; Vegge, T.; De Jongh, P. E.; Blanchard, D. All-Solid-State Lithium-Sulfur Battery Based on a Nanoconfined LiBH4 Electrolyte. *J. Electrochem. Soc.* **2016**, *163* (9), 2029–2034.

(51) Choi, Y. S.; Lee, Y.-S.; Choi, D.-J.; Chae, K. H.; Oh, K. H.; Cho, Y. W. Enhanced Li Ion Conductivity in LiBH4–Al2O3 Mixture via Interface Engineering. *J. Phys. Chem. C* **2017**, *121* (47), 26209–26215.

(52) Xu, X.; Zang, L.; Zhao, Y.; Zhao, Y.; Wang, Y.; Jiao, L. Hydrogen Storage Behavior of LiBH4improved by the Confinement of Hierarchical Porous ZnO/ZnCo2O4nanoparticles. *J. Power Sources* **2017**, *359*, 134–141.

(53) Choi, Y. S.; Lee, Y.-S.; Oh, K. H.; Cho, Y. W. Interface-Enhanced Li Ion Conduction in a LiBH4 –SiO2 Solid Electrolyte. *Phys. Chem. Chem. Phys.* **2016**, *18* (32), 22540–22547.

(54) Stoneham, A. M.; Wade, E.; Kilner, J. A. A Model for the Fast Ionic Diffusion in Alumina-Doped LiI. *Mater. Res. Bull.* **1979**, *14* (5), 661–666.

(55) Maekawa, H.; Fujimaki, Y.; Shen, H.; Kawamura, J.; Yamamura, T. Mesopore Size Dependence of the Ionic Diffusivity in Alumina Based Composite Lithium Ionic Conductors. *Solid State Ionics* **2006**, *177* (26–32 SPEC. ISS.), 2711–2714.

(56) Zhuravlev, L. T. The Surface Chemistry of Amorphous Silica. Zhuravlev Model. *Colloids Surfaces A Physicochem. Eng. Asp.* **2000**, *173* (1–3), 1–38.

(57) Lundén, A. On the Paddle-Wheel Mechanism for Cation Conduction in Lithium Sulfate. *Z. Naturforsch.* **1995**, *1076* (50a), 1067–1076.

(58) Allen J. Bard, L. R. F. *Electrochemical Methods: Fundamentals and Applications*, 2nd ed.; John Wiley and Sons, 2001.

(59) PLETCHER, D.; GREFF, R.; PEAT, R.; PETER, L. M.; ROBINSON, J. Potential Sweep Techniques and Cyclic Voltammetry. *Instrum. Methods Electrochem.* **2010**, 178–228.

(60) Þorsteinn, D.; Bjerg, M. Design and Characterisation of Solid Electrolytes for All-Solid-State Lithium Batteries Daði Þ . Sveinbjörnsson Design and Characterisation of Solid Electrolytes for All-Solid-State Lithium Batteries. **2014**.

(61) Lasia, A. *Electrochemical Impedance Spectroscopy and Its*.

(62) Beekmans, N. M.; Heyne, L. Correlation between Impedance, Microstructure and Composition of Calcia-Stabilized Zirconia. *Electrochim. Acta* **1976**, *21* (4), 303–310.

(63) Dijk van, T.; Burggraaf, A. J. Grain Boundary Effects on Ionic Conductivity in Ceramic GdxZr1-xO2-(x/2) Solid Solutions. *Phys. Status Solidi A Appl. Res.* **1981**, *63* (1981), 229.

(64) Haile, S. M.; West, D. L.; Campbell, J. The Role of Microstructure and Processing on the Proton Conducting Properties of Gadolinium-Doped Barium Cerate. *J. Mater. Res.* **1998**, *13* (6), 1576–1595.

(65) PerkinElmerInc. A Beginners Guide Thermogravimetric Analysis (TGA) - PerkinElmer https://www.perkinelmer.com/lab-solutions/resources/docs/faq_beginners-guide-to-thermogravimetric-analysis_009380c_01.pdf.

(66) CreaciveBiostrucuture. MagHelix™ Thermal Gravimetric Analysis (TGA) https://www.creative-biostructure.com/maghelix™-thermal-gravimetric-analysis-tga-216.htm (accessed Nov 9, 2018).

(67) BrukerBioSpin. *AVANCE Beginners Guide*; Rheinstetten, Germany, 2004.

(68) Reich, H. J. Summary of Nuclear Properties https://www.chem.wisc.edu/areas/reich/nmr/07-multi-01-nuclear.htm.

(69) HAHN, E.L, MAXWELL, D. E. Spin Echo Measurements of Nuclear Spin Coupling in Molecules. *Phys. Rev.* **1952**, *88* (5), 1070–1084.

(70) Duer, M. J. The Theory of Solid-State NMR and Chapter 1 The Basics of Solid-State NMR. **2002**.

(71) Duer, M. J. Chapter 2 Essential Techniques for Spin- – 2 Nuclei. **2002**.

(72) Kramer, F.; Deshmukh, M. V.; Kessler, H.; Glaser, S. J. *Residual Dipolar Coupling Constants: An Elementary Derivation of Key Equations*; 2004; Vol. 21.

(73) Polenova, T.; Gupta, R.; Goldbourt, A.; Aviv, T. Magic Angle Spinning NMR Spectroscopy: A Versatile Technique for Structural and Dynamic Analysis of Solid-Phase Systems. **2016**, *87* (11), 5458–5469.

(74) Duer, M. J. NMR Techniques for Studying Molecular Motion in Solids. In *Solid-State NMR Spectroscopy Principles and Applications*; 2007; pp 237–279.

(75) Griffin, J. M.; Forse, A. C.; Wang, H.; Trease, N. M.; Taberna, P. L.; Simon, P.; Grey, C.

P. Ion Counting in Supercapacitor Electrodes Using NMR Spectroscopy. *Faraday Discuss.* **2014**, *176*, 49–68.

(76) Indris, S.; Heitjans, P.; Uecker, R.; Roling, B. Spectroscopy and Conductivity Measurements. **2012**, 7–11.

(77) Jimura, K.; Hayashi, S. Reorientational Motion of BH4 Ions in Alkali Borohydrides MBH4 (M = Li, Na, K) as Studied by Solid-State NMR. *J. Phys. Chem. C* **2012**, *116* (7), 4883–4891.

(78) Gardiner, D. J. (1989). P. R. spectroscopy. S.-V. I. 978-0-387-50254-0. *Practical Raman Spectroscopy*; Springer-Verlag: Berlin, Germany, 1989.

(79) Vandenabeele, P. *Practical Raman Spectroscopy*; Wiley: Ghent, Belgium, 2013.

(80) Salthouse, J.A.; Ware, M. J. (1972). *Point Group Character Tables and Related Data*; Cambridge University Press, 1972.

(81) ThermoFishcerScientific. An Introduction to Electron Microscopy https://www.fei.com/documents/introduction-to-microscopy-document/.

(82) Swapp, S. Scanning Electron Microscopy http://serc.carleton.edu/research_education/geochemsheets/techniques/SEM.html (accessed Nov 23, 2018).

(83) Zhou, W., Apkarian, R., Wang, Z., Joy, D. Fundamentals of Scanning Electron Microscopy (SEM). In *Scanning Microscopy for Nanotechnology*; Zhou, W., Ed.; Springer: New York, 2006.

(84) Goodge, J. Energy-Dispersive X-Ray Spectroscopy (EDS) https://serc.carleton.edu/research_education/geochemsheets/eds.html.

(85) Tendeloo, G. Van. *Handbook of Microscopy*; 1997; Vol. II.

(86) Aquilanti, G.; Giorgetti, M.; Dominko, R.; Stievano, L.; Arčon, I.; Novello, N.; Olivi, L. *Operando* Characterization of Batteries Using X-Ray Absorption Spectroscopy: Advances at the Beamline XAFS at Synchrotron Elettra. *J. Phys. D. Appl. Phys.* **2017**, *50* (7), 74001.

(87) Newville, M. Fundamentals of XAFS. *Rev. Mineral. Geochemistry* **2014**, *78* (1), 33–74.

(88) Penner-Hahn, J. E. Comprehensive Coordination Chemistry II. *Compr. Coord. Chem. II* **2003**, 159–186.

(89) Alp, E. E.; Mini, S. M.; Ramanathan, M. X-Ray Absorption Spectroscopy: EXAFS and XANES-A Versatile Tool to Study the Atomic and Electronic Structure of Materials. *Synchrotron x-ray sources new Oppor. soil Environ. Sci.* **1990**, 25–36.

(90) Das, S.; Ngene, P.; Norby, P.; Vegge, T.; Jongh, P. E. De; Blanchard, D. All-Solid-State Lithium-Sulfur Battery Based on a Nanoconfined LiBH 4 Electrolyte. *J. Electrochem. Soc.* **2016**, *163* (9), 2029–2034.

(91) Van der Vegt, A. K. *Polymeren: Van Keten Tot Kunststof*; Delft University Press: Delft, 1991.

(92) Bentzen, J. J.; Wichmann, M.; Blanchard, D. Transportable Device for Transference of Atmosphere Sensitive Materials from Glove Box to High Resolution Scanning Electron Microscope. **2017**, 9–10.

(93) Robin Bendall, M.; Gordon, R. E. Depth and Refocusing Pulses Designed for Multipulse NMR with Surface Coils. *J. Magn. Reson.* **1983**, *53* (3), 365–385.

(94) Bielecki, A.; Burum, D. P. Temperature Dependence of 207Pb MAS Spectra of Solid Lead Nitrate. An Accurate, Sensitive Thermometer for Variable-Temperature MAS. *J. Magn. Reson. Ser. A* **1995**, *116* (2), 215–220.

(95) Christiansen, A. S.; Stamate, E.; Thydén, K.; Younesi, R.; Holtappels, P. Plasma Properties during Magnetron Sputtering of Lithium Phosphorous Oxynitride Thin Films. *J. Power Sources* **2015**, *273*, 863–872.

(96) Blanchard, D.; Nale, A.; Sveinbjörnsson, D.; Eggenhuisen, T. M.; Verkuijlen, M. H. W.; Suwarno; Vegge, T.; Kentgens, A. P. M.; De Jongh, P. E. Nanoconfined LiBH4 as a Fast Lithium Ion Conductor. *Adv. Funct. Mater.* **2015**, *25* (2), 184–192.

(97) Lefevr, J.; Cervini, L.; Gri, J. M.; Blanchard, D. Lithium Conductivity and Ions Dynamics in LiBH 4 / SiO 2 Solid Electrolytes Studied by Solid-State NMR and Quasi-Elastic Neutron Scattering and Applied in Lithium − Sulfur Batteries. **2018**.

(98) Gomes, S.; Hagemann, H.; Yvon, K. Lithium Boro-Hydride LiBH$_4$: II. Raman Spectroscopy. *J. Alloys Compd.* **2002**, *346* (1--2), 206–210.

(99) Hwang, S.; Lee, H.; To, M.; Lee, Y.; Whan, Y.; Choi, H.; Kim, C. Probing Molecular Dynamics of Metal Borohydrides on the Surface of Mesoporous Scaffolds by Multinuclear High Resolution Solid State NMR. *J. Alloys Compd.* **2015**, *645*, S316–S319.

(100) Corey, R. L.; Shane, D. T.; Bowman, R. C.; Conradi, M. S. Atomic Motions in LiBH 4 by NMR. *J. Phys. Chem. C* **2008**, *112*, 18706–18710.

(101) Corey, R. L.; Shane, D. T.; Bowman, R. C.; Conradi, M. S. Atomic Motions in LiBH4 by NMR. *J. Phys. Chem. C* **2008**, *112*, 18706–18710.

(102) Shane, D. T.; Corey, R. L.; McIntosh, C.; Rayhel, L. H.; Bowman, R. C.; Vajo, J. J.; Gross, A. F.; Conradi, M. S. LiBH4 in Carbon Aerogel Nanoscaffolds: An NMR Study of Atomic Motions. *J. Phys. Chem. C* **2010**, *114* (9), 4008–4014.

(103) Epp, V.; Wilkening, M. Fast Li Diffusion in Crystalline LiBH4 due to Reduced Dimensionality: Frequency-Dependent NMR Spectroscopy. *Phys. Rev. B* **2010**, *82* (2), 20301.

(104) Crivellaro, G. Lithium-Sulphur Batteries. An Experimental Approach, DTU, 2018.

(105) Her, J. H.; Yousufuddin, M.; Zhou, W.; Jalisatgi, S. S.; Kulleck, J. G.; Zan, J. A.; Hwang, S.

J.; Bowman, R. C.; Udovic, T. J. Crystal Structure of Li2B12H12: A Possible Intermediate Species in the Decomposition of LiBH4. *Inorg. Chem.* **2008**, *47* (21), 9757–9759.

(106) Friedrichs, O.; Remhof, a; Hwang, S. J.; Züttel, a. Role of Li 2 B 12 H 12 for the Formation and Decomposition of LiBH 4. *Chem. Mater.* **2010**, *22* (10), 3265–3268.

(107) Liu, X.; Majzoub, E. H.; Stavila, V.; Bhakta, R. K.; Allendorf, M. D.; Shane, D. T.; Conradi, M. S.; Verdal, N.; Udovic, T. J.; Hwang, S. J. Probing the Unusual Anion Mobility of LiBH4confined in Highly Ordered Nanoporous Carbon Frameworks via Solid State NMR and Quasielastic Neutron Scattering. *J. Mater. Chem. A* **2013**, *1* (34), 9935–9941.

(108) Ji, X.; Lee, K. T.; Nazar, L. F. A Highly Ordered Nanostructured Carbon-Sulphur Cathode for Lithium-Sulphur Batteries. *Nat. Mater.* **2009**, *8* (6), 500–506.

(109) Song, M.-K.; Cairns, E. J.; Zhang, Y. Lithium/sulfur Batteries with High Specific Energy: Old Challenges and New Opportunities. *Nanoscale* **2013**, *5* (6), 2186–2204.

(110) Kobayashi, T.; Imade, Y.; Shishihara, D.; Homma, K.; Nagao, M.; Watanabe, R.; Yokoi, T.; Yamada, A.; Kanno, R.; Tatsumi, T. All Solid-State Battery with Sulfur Electrode and Thio-LISICON Electrolyte. *J. Power Sources* **2008**, *182* (2), 621–625.

(111) Das, S.; Ngene, P.; Norby, P.; Vegge, T.; Jongh, P. E. De; Blanchard, D. All-Solid-State Lithium-Sulfur Battery Based on a Nanoconfined LiBH 4 Electrolyte. *Submitt. to J. Electrochem. Soc.*

(112) Sveinbjornsson, D.; Christiansen, A. S.; Viskinde, R.; Norby, P.; Vegge, T. The LiBH4-LiI Solid Solution as an Electrolyte in an All-Solid-State Battery. *J. Electrochem. Soc.* **2014**, *161* (9), A1432–A1439.

(113) Kim, J.; Lee, D. J.; Jung, H. G.; Sun, Y. K.; Hassoun, J.; Scrosati, B. An Advanced Lithium-Sulfur Battery. *Adv. Funct. Mater.* **2013**, *23* (8), 1076–1080.

(114) Ren, Y. X.; Zhao, T. S.; Liu, M.; Tan, P.; Zeng, Y. K. Modeling of Lithium-Sulfur Batteries Incorporating the Effect of Li2S Precipitation. *J. Power Sources* **2016**, *336*, 115–125.

(115) Le Van-Jodin, L.; Ducroquet, F.; Sabary, F.; Chevalier, I. Dielectric Properties, Conductivity and Li+ion Motion in LiPON Thin Films. *Solid State Ionics* **2013**, *253*, 151–156.

(116) Lefevr, J.; Blanchard, D.; Stamate, E. Improving Performance of All-Solid-State Lithium-Sulfur Batteries by Magnetron Sputtering of Lithium Phosphorous Oxynitride Thin Films. In *LiSM3 2018 Conference*; Chicago, USA, 2018; pp 3–4.

(117) Paskevicius, M.; Richter, B.; Polański, M.; Thompson, S. P.; Jensen, T. R. Sulfurized Metal Borohydrides. *Dalt. Trans.* **2015**, *45* (2), 639–645.

(118) Yermukhambetova, A.; Tan, C.; Daemi, S. R.; Bakenov, Z. Exploring 3D Microstructural Evolution in Li-Sulfur Battery Electrodes Using in-Situ X-Ray Tomography. *Nat. Publ. Gr.* **2016**, No. October, 1–9.

(119) Boin, M.; Haibel, A. Compensation of Ring Artefacts in Synchrotron Tomographic Images. **2006**, *14* (25), 12071–12075.

(120) J. H. Hubbell and S. M. Seltze. *X-Ray Mass Attenuation Coefficients*; 2016.

Appendix

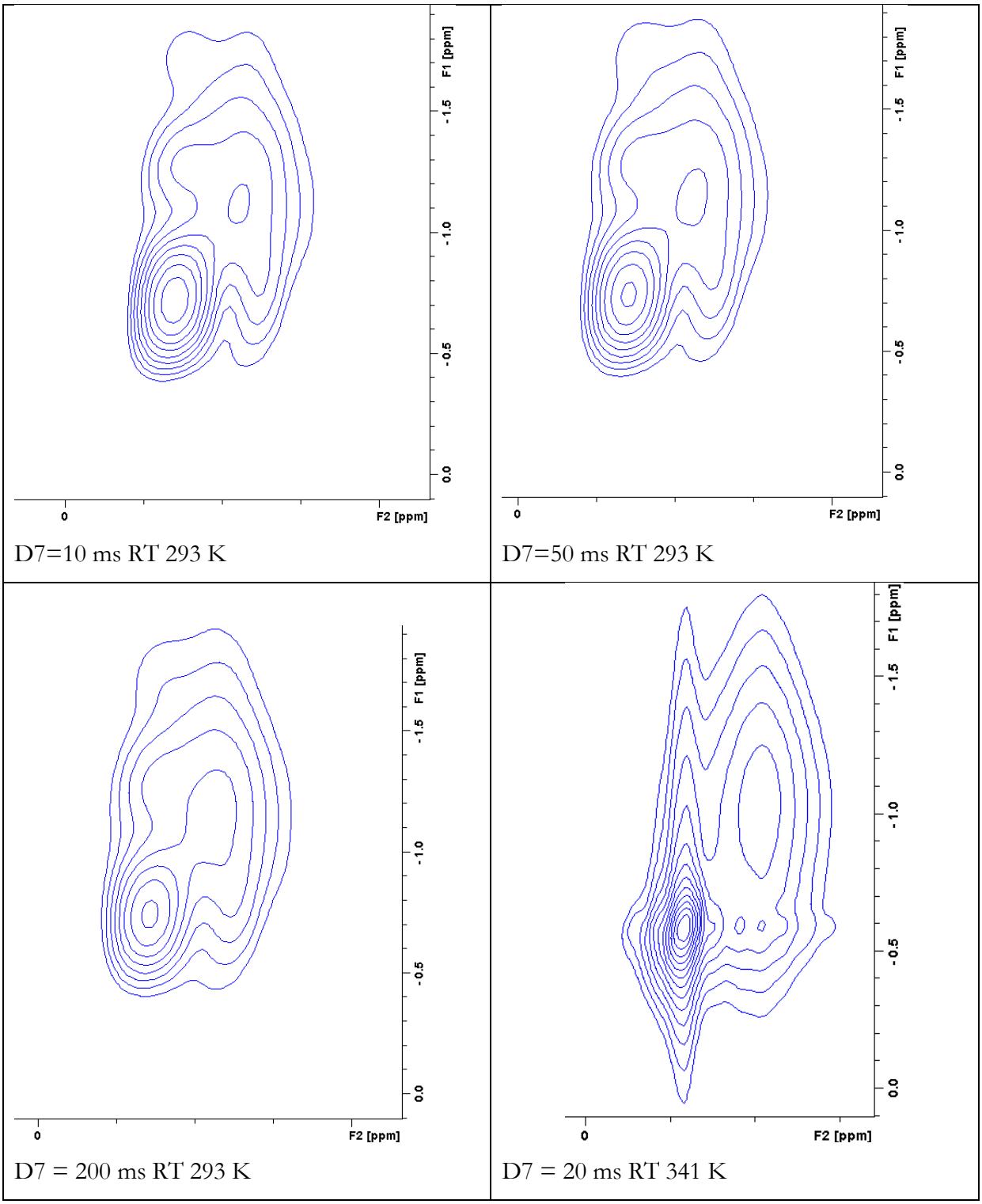

Figure A 1 2-D EXSY spectra of 7Li for 30/70 wt% $LiBH_4$-SiO_2

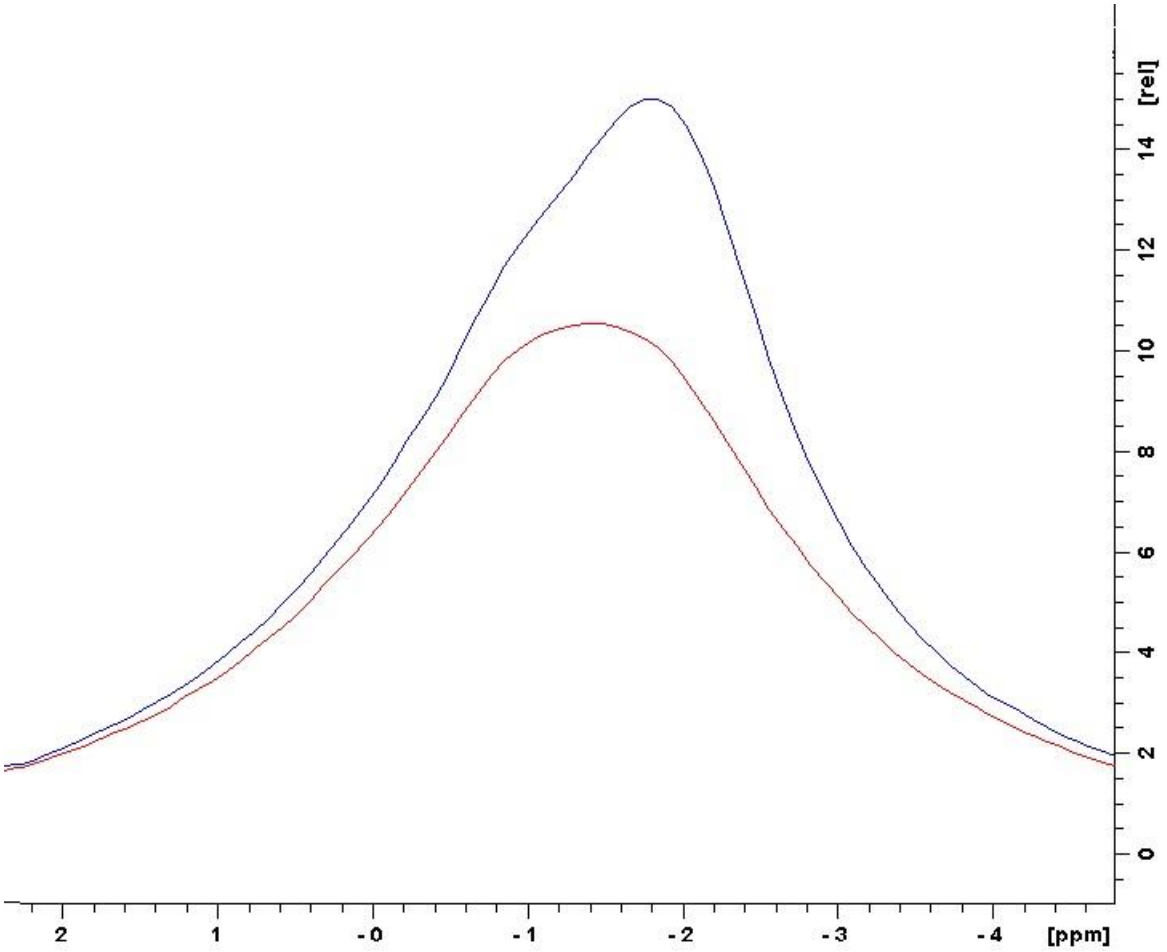

Figure A 2: Single pulse 7Li resonance of 30 (red) and 35 (blue) wt% $LiBF_4$- $LiBH_4$

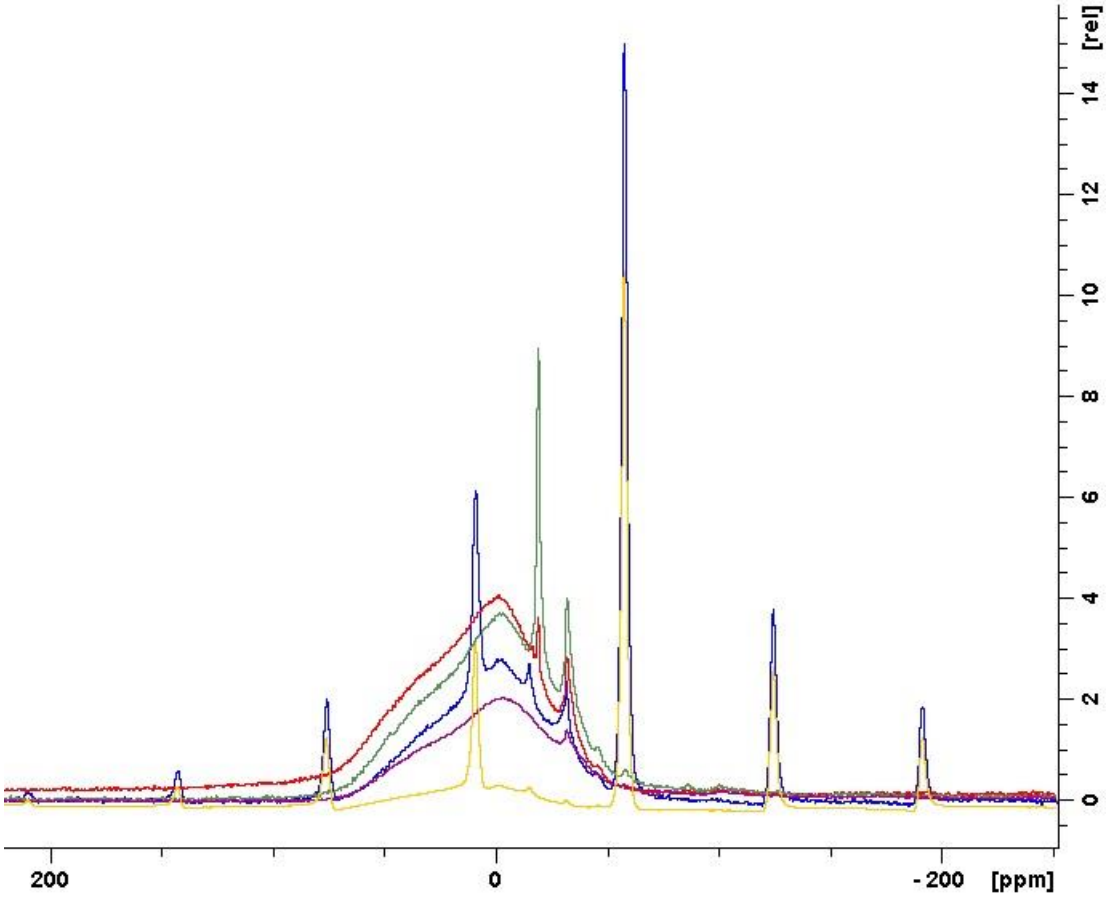

Figure A 3 11B High-power decoupling spectra 5 (yellow), 20 (blue), 30 (red), 35 (green) wt% LiBF4-LiBH4 compared to pure Li2B12H12 (purple)

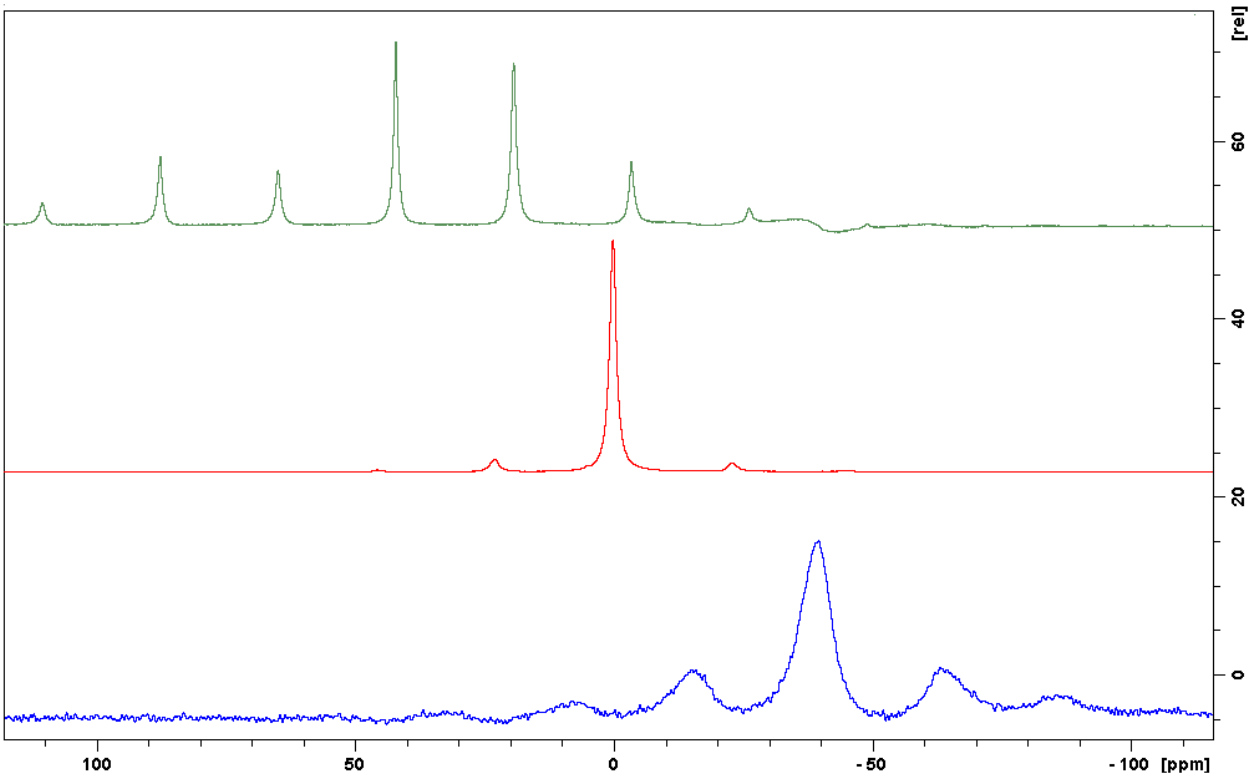

Figure A 4 19 F spectra of 80/20 wt% $LiBH_4$-$LiBF_4$ (green) compared to pure $LiBF_4$ (red) and pure LiF (blue) at 293 K